Gustavo Henrique Silvestre

Computational Simulations Applied on Boron and Carbon Based 2D Materials

Uberlândia

2022

Gustavo Henrique Silvestre

Computational Simulations Applied on Boron and Carbon Based 2D Materials

Instituto de Física
Universidade Federal de Uberlândia

Supervisor: Prof. Dr. Roberto Hiroki Miwa

Uberlândia
2022

Dados Internacionais de Catalogação na Publicação (CIP)
Sistema de Bibliotecas da UFU, MG, Brasil.

S587c
2022

Silvestre, Gustavo Henrique, 1991-
Computational simulations applied on boron and carbon based 2D materials [recurso eletrônico] / Gustavo Henrique Silvestre. - 2022.

Orientador: Roberto Hiroki Miwa.
Tese (Doutorado) - Universidade Federal de Uberlândia, Programa de Pós-Graduação em Física.
Modo de acesso: Internet.
Disponível em: http://doi.org/10.14393/ufu.te.2023.8038
Inclui bibliografia.

1. Física. I. Miwa, Roberto Hiroki, 1964-, (Orient.). II. Universidade Federal de Uberlândia. Programa de Pós-Graduação em Física. III. Título.

CDU: 53

André Carlos Francisco
Bibliotecário - CRB-6/3408

UNIVERSIDADE FEDERAL DE UBERLÂNDIA
Coordenação do Programa de Pós-Graduação em Física
Av. João Naves de Ávila, 2121, Bloco 1A, Sala 213 - Bairro Santa Mônica, Uberlândia-MG, CEP 38400-902
Telefone: (34) 3239-4309 - www.infis.ufu.br - cpgfisica@ufu.br

ATA DE DEFESA - PÓS-GRADUAÇÃO

Programa de Pós-Graduação em:	Física				
Defesa de:	Defesa de Doutorado				
Data:	Vinte e dois de Novembro de 2022	Hora de início:	14:10	Hora de encerramento:	18:30
Matrícula do Discente:	11823FIS001				
Nome do Discente:	Gustavo Henrique Silvestre				
Título do Trabalho:	Computational Simulations Applied on Boron and Carbon Based 2D Materials				
Área de concentração:	Física				
Linha de pesquisa:	Estrutura eletrônica e Simulações Computacionais				
Projeto de Pesquisa de vinculação:	Simulação Computacional Aplicada à Sistemas 1D e 2D: Estabilidade Estrutural, Transporte Eletrônico, Fases Topológicas e a Interação com Superfícies Sólidas.				

Reuniu-se por meio de Videoconferência a Banca Examinadora, designada pelo Colegiado do Programa de Pós-graduação em Física, assim composta: Professores Doutores: Alexandre MArletta - INFIS/UFU, Daiane Damasceno Borges - INFIS/UFU, José Eduardo Padilha de Souza - UFPR/PR, Pedro Paulo de Melo Venezuela- UFF/RJ e Roberto Hiroki Miwa - INFIS/UFU orientador do candidato.

Iniciando os trabalhos o presidente da mesa, Dr. Roberto Hiroki Miwa, apresentou a Comissão Examinadora e o candidato, agradeceu a presença do público, e concedeu ao Discente a palavra para a exposição do seu trabalho. A duração da apresentação do Discente e o tempo de arguição e resposta foram conforme as normas do Programa.

A seguir o senhor(a) presidente concedeu a palavra, pela ordem sucessivamente, aos(às) examinadores(as), que passaram a arguir o(a) candidato(a). Ultimada a arguição, que se desenvolveu dentro dos termos regimentais, a Banca, em sessão secreta, atribuiu o resultado final, considerando o(a) candidato(a):

Aprovado

Esta defesa faz parte dos requisitos necessários à obtenção do título de Doutor.

O competente diploma será expedido após cumprimento dos demais requisitos, conforme as normas do Programa, a legislação pertinente e a regulamentação interna da UFU.

Nada mais havendo a tratar foram encerrados os trabalhos. Foi lavrada a presente ata que após lida e achada conforme foi assinada pela Banca Examinadora.

Documento assinado eletronicamente por **Roberto Hiroki Miwa**, **Professor(a) do Magistério Superior**, em 24/11/2022, às 09:31, conforme horário oficial de Brasília, com fundamento no art. 6º, § 1º, do Decreto nº 8.539, de 8 de outubro de 2015.

Documento assinado eletronicamente por **Alexandre Marletta**, **Professor(a) do Magistério Superior**, em 25/11/2022, às 07:35, conforme horário oficial de Brasília, com fundamento no art. 6º, § 1º, do Decreto nº 8.539, de 8 de outubro de 2015.

Documento assinado eletronicamente por **Daiane Damasceno Borges**, **Professor(a) do Magistério Superior**, em 25/11/2022, às 08:45, conforme horário oficial de Brasília, com fundamento no art. 6º, § 1º, do Decreto nº 8.539, de 8 de outubro de 2015.

Documento assinado eletronicamente por **José Eduardo Padilha de Sousa**, **Usuário Externo**, em 30/11/2022, às 08:17, conforme horário oficial de Brasília, com fundamento no art. 6º, § 1º, do Decreto nº 8.539, de 8 de outubro de 2015.

Documento assinado eletronicamente por **Pedro Paulo de Mello Venezuela**, **Usuário Externo**, em 08/12/2022, às 09:44, conforme horário oficial de Brasília, com fundamento no art. 6º, § 1º, do Decreto nº 8.539, de 8 de outubro de 2015.

A autenticidade deste documento pode ser conferida no site https://www.sei.ufu.br/sei/controlador_externo.php?acao=documento_conferir&id_orgao_acesso_externo=0, informando o código verificador **4090636** e o código CRC **CC8026CA**.

Agradecimentos

Agradeço primeiramente a Deus, por ter me conduzido até aqui, que é onde sempre quis estar. Aos meus pais e avós, pelo apoio incondiconal. A minha esposa Letícia por sempre me apoiar e estar ao meu lado - sem você jamais chegaria e nem estaria aqui. Ao professor Hiroki, não apenas pela orientação, mas pela amizade, pela convivência, pela paciência, pelos ensinamentos, por me ensinar a ser um cientista com seu exemplo - certamente levarei por toda a vida. Aos professores Wanderlã Scopel, Juliana Bernardes, Adalberto Fazzio e Felipe Lima, pela colaboração nos artigos publicados. A coordenação do PPGFIS pelo apoio necessário no decorrer do curso. A todos os os amigos que fiz durante os seis anos de pós. Aos irmãos de 1X12 - Pedro, Emmanuel, Felipe, Willian, Dominike e Marcos - pelos Überbrau de comemoração, cafézinho e pão de queijo, arrumar computadores e cafeteiras, e várias outras coisas. Vocês são incríveis! A CAPES e INCT pelo apoio finnceiro. Ao CENAPAD-SP e ao LNCC pelo tempo computacional. Enfim, agradeço à todos que ajudaram de maneira direta ou indireta na realização deste trabalho.

Acknowledgements

First of all, I thank God for leading me here, where I always wanted to be. To my parents and grandparents for their unconditional support. To my wife Letícia for always supporting me and being by my side, I'd never been here without you. To Professor Hiroki, not only for the guidance but for the friendship, for working together, for the patience, for the teachings, for teaching me with your example of how to be a scientist - I will certainly carry it for the rest of my life. To professors Wanderlã Scopel, Juliana Bernardes, Adalberto Fazzio and Felipe Lima, for their collaboration in the published articles. The coordination of PPGFIS for the support during the course. To all the friends I made during these six years in my post-graduate time. To the brothers of 1X12 - Pedro, Emmanuel, Felipe, Willian, Dominike, Marcos - for everything we lived, as the Überbrau happy hours, all koffies and *pão de queijo*, PC's and coffee machine fixing time, and a lot of other things. You are awesome! To CAPES and INCT for financial support. To CENAPAD-SP and LNCC for the computational time. Finally, I would like to thank everyone who helped directly or indirectly in the realization of this work.

Abstract

Neste trabalho, utilizamos a Teoria do Funcional de Densidade (DFT) na investigação de sistemas bidimensionais a base dos elementos boro e carbono. Investigamos as estruturas eletrônica e estrutural (via XANES) das fases pristinas do borofeno S0, S1 e S2 e de superredes de borofeno, formadas por diferentes concentrações das fases pristina por heterojunções laterais. Nossos resultados mostraram que o caráter metálico foi mantido e foi possível relacionar as propriedades eletrônicas com as características estruturais do borofeno, assim como o confinamento eletrônico nas superredes, regido pelas devida proporções das fases. Investigamos também o processo de desmontagem de fibrilas de celulose oxidada. Mostramos aqui que a quebra pode ser atribuída à formação dos grupos carboxilato, que enfraquece a interação, fazendo que o processo ocorra predominantemente nas interações intercadeias, levando ao surgimento de cadeias celulósicas. Investigamos também a interação celulose-grafeno, as propriedades energéticas, estruturais e eletrônicas das interfaces de nanocelulose/grafeno, com especial atenção às interfaces hidrofóbicas ($\mathrm{nCL}^{\mathrm{phob}}$/G - [100]) e hidrofílicas ($\mathrm{nCL}^{\mathrm{phil}}$/G - [110]). O *fingerprint* das interfaces $\mathrm{nCL}^{\mathrm{phob}}$/G e $\mathrm{nCL}^{\mathrm{phil}}$/G foi identificado através de um estudo detalhado de espectro de XANES da borda K dos átomos de carbono.

Palavras-chave: Teoria do Funcional de Densidade, Materiais 2D, Borofeno, Boro, Carbono, Celulose, Grafeno

Abstract

In this work, we used the Density Functional Theory (DFT) to investigate boron and carbon-based two-dimensional systems. We investigated the electronic and structural features (via simulated XANES) of borophene pristine phases S0, S1 and S2, and borophene superlattices, formed by tuning different concentrations of pristine borophene lateral heterostructures. Here the study reveals that metallic character remained and revealed the link between electronic properties and structural properties of borophene, as electronic confinement in borophene superlattices tuned by phase proportion. In carbon-based systems, we investigate the disassembling process of oxidized cellulose, We have performed a theoretical investigation of cellulose disassembly mediated oxidation processes. Here, we showed this disruption could be attributed to the formation of carboxylate groups, which weakens the interactions, and the disassembling process occurs predominantly in interchain interactions, giving rise to cellulosic chains. Next, we studied cellulose-graphene interaction, we performed an investigation of the energetic, structural, and electronic properties of the nanocellulose/graphene interface, with a special look for hydrophobic ($\mathrm{nCL}^{\mathrm{phob}}$/G) and hydrophilic ($\mathrm{nCL}^{\mathrm{phil}}$/G) interfaces. The structural fingerprints of $\mathrm{nCL}^{\mathrm{phob}}$/G and $\mathrm{nCL}^{\mathrm{phil}}$/G interfaces were identified through a detailed study of the Carbon K-edge absorption (XANES) spectra.

Key-words: DFT, 2D Materials, Borophene, Boron, Carbon, Cellulose, Graphene.

List of Figures

List of Tables

Abbreviations and Acronyms

2D	TWO-DIMENSIONAL
a.u.	ATOMIC UNITS
B	BORON
BN	BORON NITRIDE
BSL	BOROPHENE SUPERLATTICE
BZ	BRILLOUIN ZONE
C	CARBON
CNC	CELLULOSE NANOCRYSTALS
CNF	CELLULOSE NANOFIBERS/CELLULOSE NANOFIBRILS
DFT	DENSITY FUNCTIONAL THEORY
DP	DIRAC POINT
DOS	DENSITY OF STATES
$\mathbf{E^{b}}$	BINDING ENERGY
$\mathbf{E^{C}}$	COHESIVE ENERGY
EEF	EXTERNAL ELECTRIC FIELD
$\mathbf{E_{F}}$	FERMI ENERGY/FERMI LEVEL
$\mathbf{E_{V}}$	VACUUM ENERGY/VACUUM LEVEL
eV	ELECTRON-VOLT
GBL	GRAPHENE BILAYER
GGA	GENERALIZED GRADIENT APPROXIMATION
GO	GRAPHENE OXIDE
HF	HARTREE-FOCK
hBN	HEXAGONAL BORON NITRIDE
IC	INTERCHAIN

ID	INTERFACE DISTANCE
IS	INTERSHEET
KS	KOHN-SHAM
LDA	LOCAL DENSITY APROXIMATION
NC/NCL	NANOCELLULOSE
PHIL	HYDROPHILIC
PHOB	HYDROPHOBIC
PAW	PROJECTOR AUGMENTED-WAVE
PBE	FUNCIONAL PERDEW-BURKE-ERNZERHOF
PW	PLANE WAVES
QE	QUANTUM ESPRESSO
rGO	REDUCED GRAPHENE OXIDE
Ry	RYDBERG
VBM	VALENCE BAND MAXIMUM
vdW	VAN DER WAALS
VASP	VIENNA AB-INITIO SIMULATION PACKAGE
XAS	X-RAY ABSORPTION SPECTRA
XANES	X-RAY ABSORPTION NEAR EDGE STRUCTURE
SE	SCHRÖDINGER EQUATION

Contents

II CARBON BASED 2D MATERIALS 58

1 Introduction

2D systems have attracted the focus of several studies aimed at both technological applications and the understanding of new physical phenomena. An entirely new class of materials known as “2D materials” has been created as a consequence of the discovery of graphene (1, 2, 3) and its remarkable properties. Motivated by the success of graphene, alternative layered and non-layered 2D materials have become the focus of intense research due to their unique physical and chemical properties. The 2D family of materials has also recently included other new monatomic materials from the 13-, 14- and 15-family of the periodic table, such as Borophene (4, 5, 6, 7, 8) and Gallenene (9) (13-family), Silicene (10, 11) and Germanene (12) (14-family) and Phosphorene (13) (15-family). Some of these materials are listed in Fig. 1. Beyond these aforementioned, other materials (now not only exclusively monoatomic systems) like boron nitrides (14), lateral heterojunctions (15, 16), doping (17), and vdW stacking (18, 19) have shown promising properties. Fig. [2(a)] shows the increasing (quantitative) evolution of publications on 2D materials from 1992 to 2019.

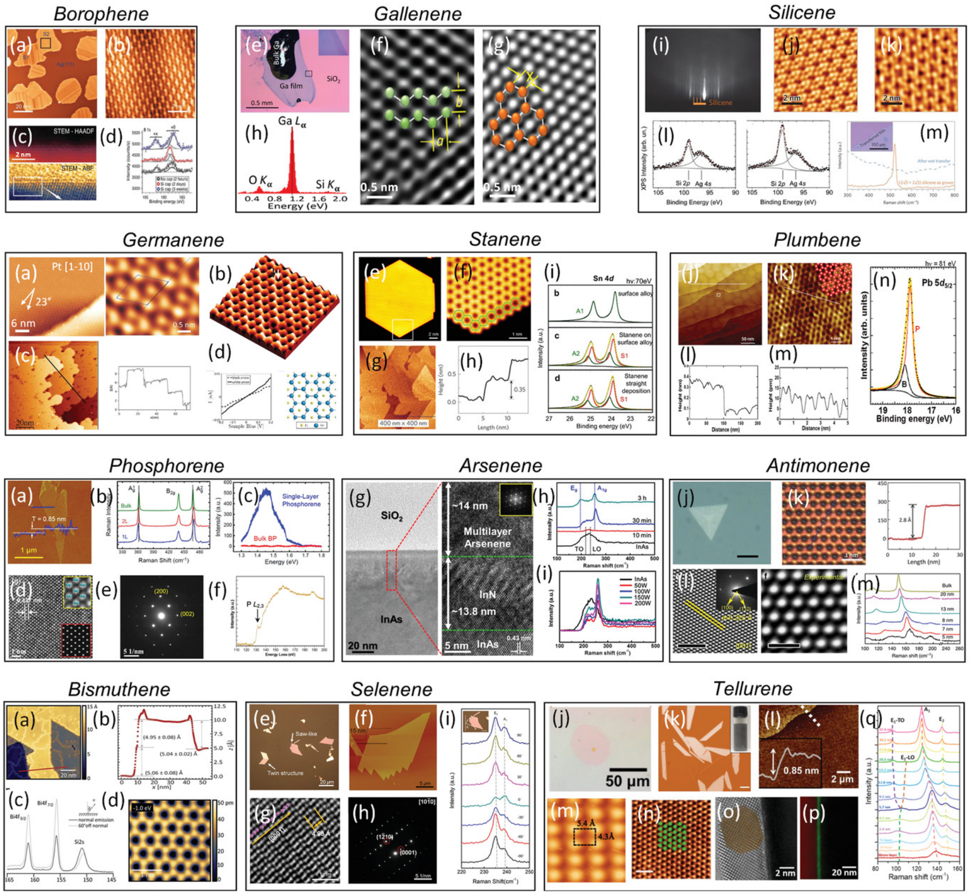

Figure 1 – 13-, 14-, 15- and 16-families 2D materials successfully synthesized, adapted from(20).

2D materials are an ideal candidate for engineering new classes of materials, and

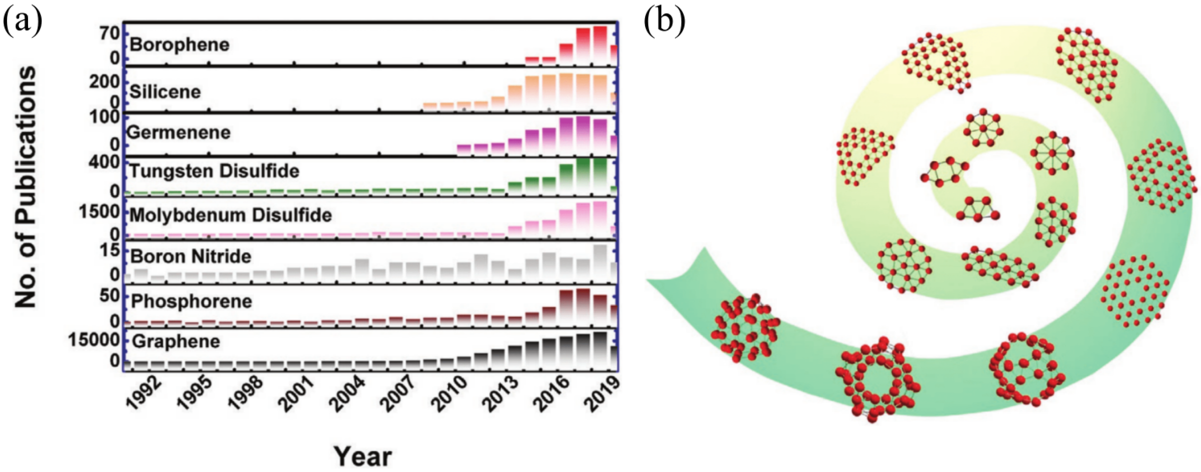

Figure 2 – The number of publications on 2D materials from 1992 to 2019 (a). Examples of boron allotropes (b), adapted from (26).

many examples have already been realized in practice, such as quantum information (21), spintronics (22), layertronics (23), vdW structures (24) and contacts (25). In this section, we will present some boron- and carbon-based materials, their main characteristics and applications.

1.1 Boron

Among these materials, borophene, a two-dimensional system formed only by boron atoms and whose name is associated with graphene, has drawn the attention of the scientific community for its electronic properties. The complexity of boron structures is attributed to its trivalent electronic configuration, forming diverse allotropes (Fig. [2(b)]) - a feature that is responsible for the interest of the scientific community for decades (27, 4). The boron metallic character makes it a potential complement to graphene, hBN, and metal disulfides which may be the ultimate building components in devices(28, 29, 30, 31, 32).

In 2015, we have the first report of borophene synthesis by Mannix et al. (6). It is worth mentioning that these sheets already was predicted in 2007 and intensively studied theoretically, even with the status, until then, of a hard material to synthesise. (33, 34). In the following year, 2016, Feng et al. (7) synthesized two other new structures, energetically more stable and resistant to oxidation - these structures were also predicted theoretically (34, 35). Different polymorphs of borophene sheets have been grown on metal substrates of Ag (111) (6), Al (111) (36), Cu (111) (37), Au (111) (38), and Ir (111) (39, 40) through different techniques. Large-scale fabrication of borophene is still challenging, but many theoretical and experimental researches have been devoted to investigating pristine and functionalized borophene potential applications (41).

The 2-*Pmmn* phase found by Mannix et al., most known in the literature as S0, was successfully synthesized in 2015. One of the ways to borophene synthesis in this phase (S0)

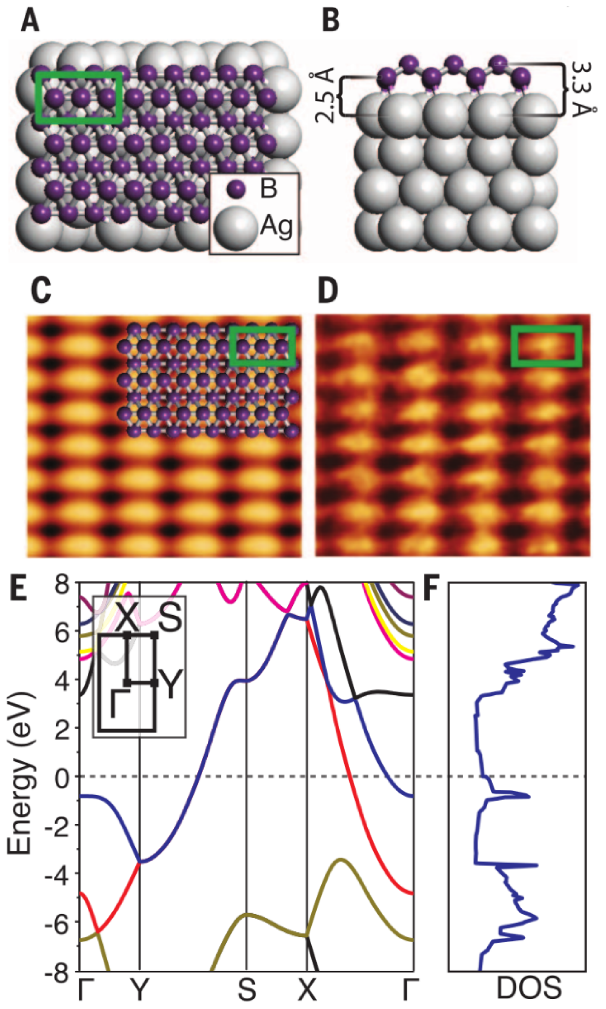

Figure 3 – Top (A) and side (B) views of the S0 borophene monolayer structure (unit cell indicated by green box). Simulated STM image ($V_{sample} = 1.0$ V), with overlaid atomic structure (C) and experimental STM images (D). DFT–calculated electronic band structure (E) and DOS (F) for freestanding borophene (inset: 2D Brillouin zone). Adapted, from (6).

is through the deposition of boron from a source of solid boron of high purity (99,9999%) on inert Ag substrates as a surface for borophene growth. During this entire process, the Ag substrate is maintained between 450 °C and 700 °C and in a UHV (ultrahigh vacuum) regime. At 550 °C it is possible to observe the formation of two distinct phases, one a homogeneous and planar phase and the other being corrugated. Sites with higher deposition of B atoms favour the emergence of a homogeneous phase, while sites with lower deposition of B atoms favour the emergence of a phase described as a corrugated ribbon. The increase in temperature favours the consolidation of the S0 phase, which suggests that the homogeneous phase is metastable to the corrugated phase (6). As mentioned, its geometry is corrugated, justified by the rectangular lattice distortions, to maximize the ideal number of boron adsorption sites, which leads to a density of holes[1] $\eta = 0$ and the

---

[1] the ratio between the number of hexagon holes and the total number of atoms in the original (pristine) triangular lattice (33).

only phase here that presents buckled geometry, with 0.87 Å of vertical distance (buckling) between the sublayers. The band structure [Fig 3(e)] indicates strong electronic anisotropic features of this phase.

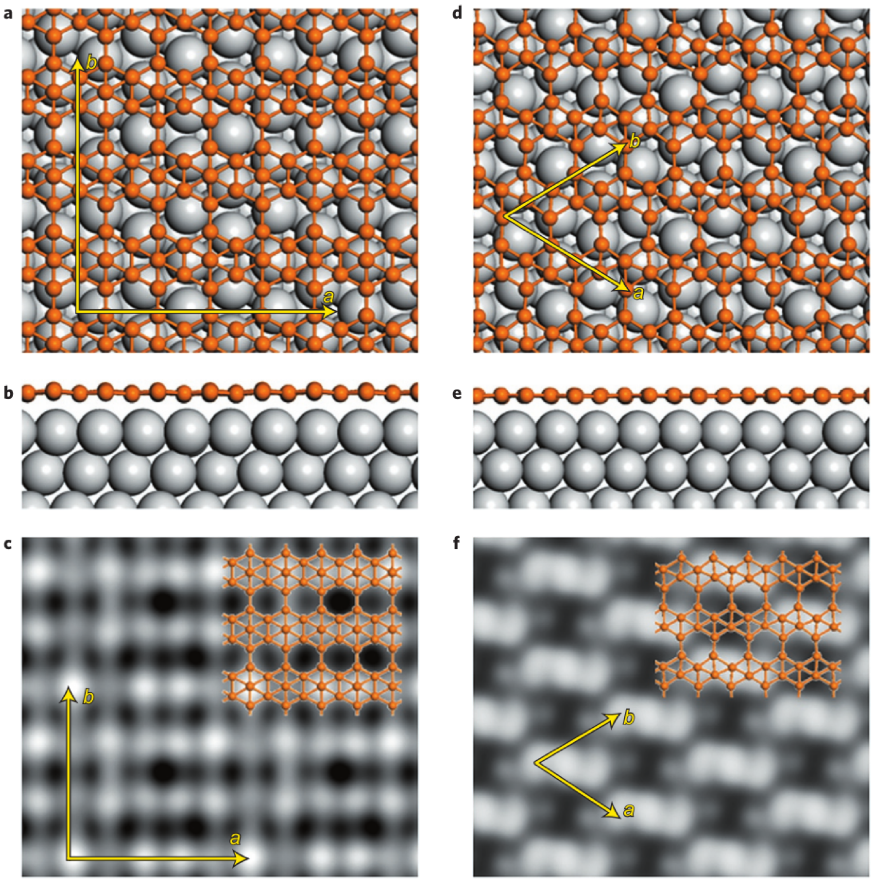

Figure 4 – Top (a) and side (b) views of the S1 model, and simulated STM topographic image of the β_{12} sheet (c). Top (d) and side (e) views of the S2 model, and simulated STM topographic image of the χ_3 sheet (f). Orange and grey balls in a,b,d and e represent boron and silver atoms, respectively. Models of the β_{12} and χ_3 sheets are superimposed on their simulated STM images, which agree very well with the experiments. The striped pattern of S1 and the alternating bright–dark protrusions of S2 are both reproduced well. Adapted from (7).

Phases β_{12} and χ_3 were synthesized in 2016 by Peng et al. (29). The β_{12} phase, also known in the literature as S1, is characterized by hole chains separated by hexagonal boron rows [Figs 4(a) and (c)] meanwhile the χ_3 phase, most known in the literature as S2, consist of similar, but narrower zigzag boron rows separated by hole arrays, as shown in Figs [4(d) and (f)]. They can also coexist in the same process (42). Both models are planar due to the presence of vacancies, vacancies that give $\eta = 1/6$ and $1/5$ for S1 and S2 respectively. These sheets were grown on a single-crystal Ag(111) surface by direct evaporation of a pure boron source. Near 570 K, monolayer islands with a perfectly ordered structure form on the surface. STM images reveal parallel stripes on the island surface in the $[\bar{1}10]$ direction of Ag(111), corresponding to the S1 phase. The S2 phase usually coexists with the S1 phase in the temperature range from 650 to 800 K. At higher temperatures, most areas of the surface will be transformed into the S2 phase.

The S2 phase can also be obtained by directly growing boron on Ag(111) with a substrate temperature next to 680 K. The electronic structure of pristine phases indicates a loss in anisotropy when compared with the S0 phase but still retains metallic features. It is worth mentioning two points: (i) the formation of a B-Ag surface alloy or boride is highly improbable (43), and (ii) the metastable homogeneous phase indicated in Ref. (6), in the synthesis of the S0 phase corresponds to the S2 phase. In this work, we will consider only the borophene freestanding sheet, i.e., without considering the substrate interaction.

In some borophene systems, more specifically in borophene heterostructures, the formation of metallic channels occurs (44, 45), which, in addition to the anisotropy regarding electronic transport, can lead to the formation of preferential sites for the adsorption of atoms and molecules. In a previous study, (44), was inferred that the S0 phase laterally attached in the S1 phase induces a preferential direction to form metallic channels, ruled by the phase proportion and the direction of the attachment. In Ref. (45), this behaviour remains but is more intense due to the common features of this phase (42).

1.2 Carbon

Carbon nanostructures are a leading material in the nanotechnology field. The discovery and research of carbon materials have considerably contributed to the advancement of modern-day science and technology. Due to its exceptional qualities, such as excellent thermal conductivity, extreme mechanical properties, and ultra-high electron mobilities, graphene has received the most attention among 2D materials since its discovery. Researchers are interested in graphene oxide (GO), which has oxygen-containing groups attached to the graphene sheets. To interact with a variety of metal oxides and create functional hybrids and composites with unique properties, GO must have oxygen-containing functional groups in the basal plane (epoxy and hydroxyl) and the sheet edges (carbonyl and carboxyl). A material similar to graphene with comparable property values can be produced by encouraging the total or partial reduction of GO; this reduction product is known as reduced graphene oxide (rGO). A wide range of chemical and physical properties may also be obtained by using the functional groups in GO as sites for chemical modification or functionalization. About carbon-based 2D materials, the three mentioned above are the best known, but there are several other materials. One of these materials that have been widely studied is cellulose.

Cellulose is composed of carbon, oxygen and hydrogen atoms ($[C_6H_{10}O_5]_n$), forming crystalline fibers on a nanoscale (46, 47), and is better known as one of the most ubiquitous polymers in Earth. Also, is responsible for a lot of high-importance products for modern society, including papers, tissue, adhesives even automotive and construction compounds.

With new materials cellulose-based, new research revealed properties and their importance in this new field(48). An example of an application is the development of piezoelectric sensors (49, 50), ionic conductors (51), construction of nanogenerators mediated by the incorporation of metals such as copper (52), in addition to the construction of nanofibers, due to their mechanical properties such as high tensile strength (53). Micro and nanoscale cellulosic fibres are appealing to replace synthetic fibres as reinforcement in environmentally friendly green products. Although its industrial use is generally for making paper and cardboard, it has also attracted significant interest as a source of biofuel production (54).

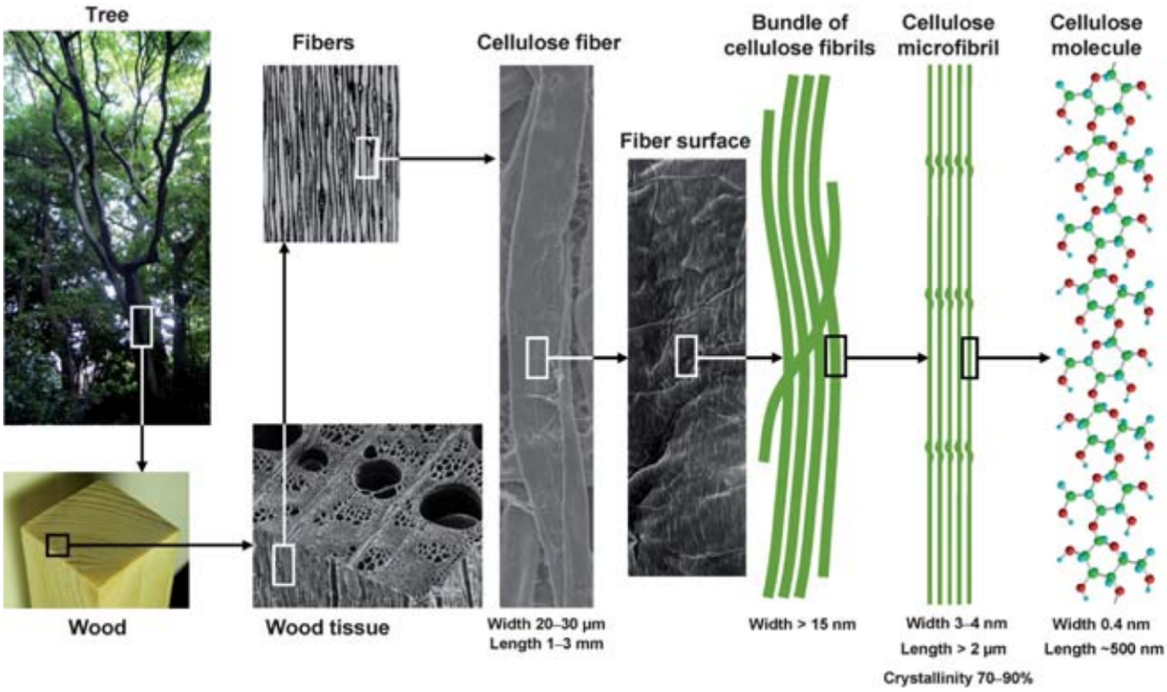

Figure 5 – Hierarchical structure of wood biomass and the characteristics of cellulose microfibrils, adapted from (55).

Structurally, cellulose is a homopolymer with linear chains of glucopyranose rings linked through β-(1,4)-glycosidic bonds, which interact with other macromolecules as lignin and hemicellulose, within the plant cell walls (56, 57). Depending on the source of cellulose, its structure can vary considerably. Cellulose fibers exhibit a unique structural hierarchy derived from their biological origin, as shown in Fig. (5). They are composed of nanofiber assemblies with a diameter that ranges from 1 to 20 nm and a length of more than a few micrometres. The previous figure exhibits the structural hierarchy of wood biomass but is also possible to extract fibres from non-wood fibres, such as coconut trees, pineapple leaf fibres, jute, flax and bagasse.

Cellulose particles with at least one dimension in the nanoscale (1–100 nm) are referred to as nanocellulose (NC). Nanocellulose is a general term for cellulosic materials that have at least one dimension in the nanometer range. Depending on the production conditions, which influence the dimensions, composition and properties, nanocellulose can be divided into two main categories: (i) CNC - cellulose nanocrystals (even named as cellulose whiskers) and (ii) CNF - cellulose nanofibrils, also known as nanofibrillated cellulose, microfibrillated cellulose or cellulose nanofibers (58). While CNCs are rod-like rigid particles, CNFs are long, flexible nanofibers that are entangled and have both crystalline and amorphous sections. Due to the lignocellulosic matrix's compact and rigid structure, also known as biomass recalcitrance[2], the production of CNC and CNF requires harsh conditions (59).

Sugarcane bagasse is produced on a large scale, $\sim$ 1.6 billion tons per year basis globally (60), and Brazil is currently the largest producer at about 739.3×10^6 metric tons per year (2018) (61). Usually, sugarcane bagasse has in its composition between $40\% \sim 50\%$ of cellulose. The Fig. 6 shows the general CNC extraction scheme of sugarcane bagasse.

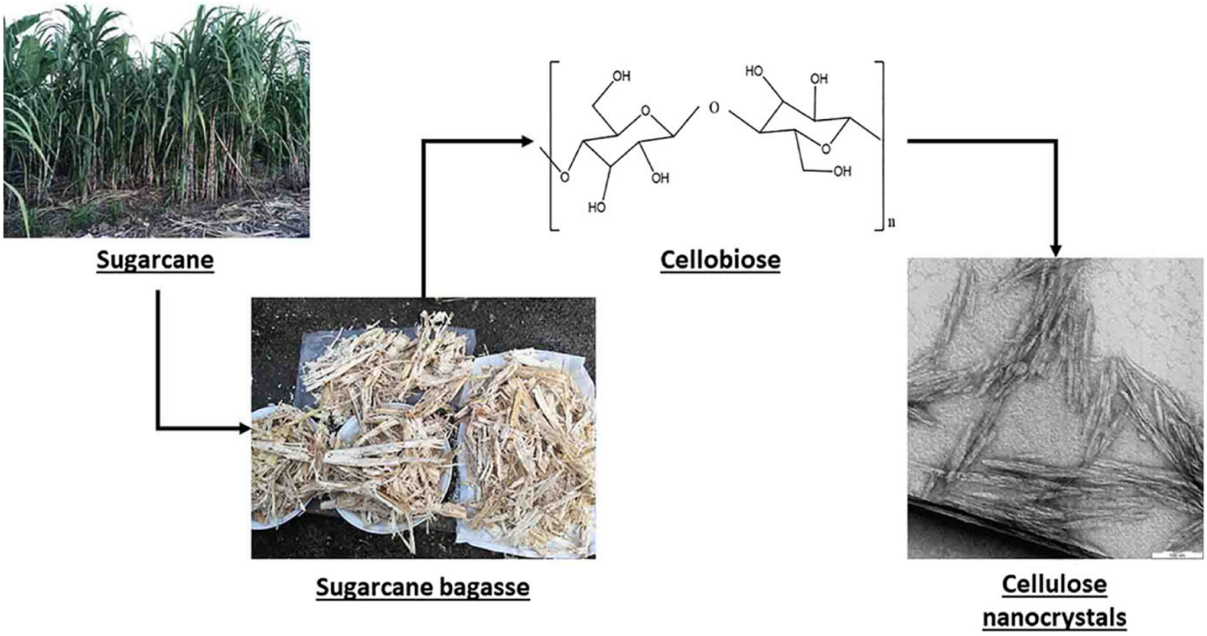

Figure 6 – Extraction of cellulose nanocrystals from sugarcane bagasse, adapted from (61).

Pinto et al. have used a recently proposed low-energy cost pathway to produce cellulose nanofibers from sugarcane bagasse with widths of single and double cellulose polymer chain (59), using TEMPO-mediated oxidation. The 2,2,6,6-tetramethylpiperidine-1-oxyl radical (TEMPO) -mediated oxidation is a way to convert completely cellulose particles in individualized cellulose nanofibers 3–4 nm wide and at least a few microns long.

There are some allomorphs of cellulose, and the most abundant in plants is called I_β. X-ray and neutron diffraction of cellulose Iβ allowed us to determine the most accurate position of all atoms in the unit cell, including the hydrogens (46). The I_β phase consists of two parallel chains slightly misaligned with each other, as shown in Fig. 7. Both H-bondings within a single layer of cellulose and stacking interactions contribute to stabilizing the cellulose crystal structure.

---

[2] The resistance of plant biomass to breakdown and to fractionate into its molecular constituents

To impart electrical conductivity to cellulose, metallic particles (62), conductive polymers (63), carbon-based particles (64), and 2D materials (65) are usually integrated into nanocellulose through different techniques (coating, dipping, printing, blending, etc.). The combination of nanocellulose and 2D nanomaterials such as graphene, MoS_2, and MXenes has recently triggered great interest in the scientific community as a new class of multifunctional hybrid compounds. For electronic applications, 2D/nanocellulose hybrid materials should be able to tolerate mechanical stress and deformations while maintaining the satisfactory electrical conductivity of 2D materials. Therefore, a fundamental understanding of how the insertion of cellulose, a dielectric compound, influences the electrical properties of 2D materials is essential to guide the development of (nano) devices.

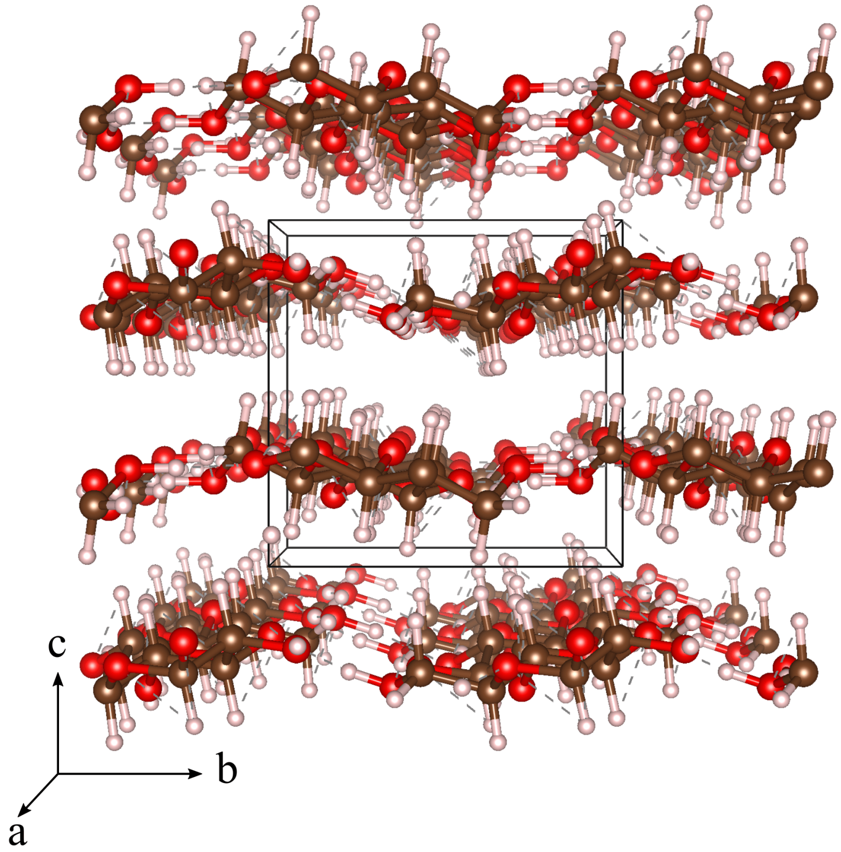

Figure 7 – Structural model of cellulose in a perspective view.

We present in Chapter 2 the details about the methodology and formalism used in the simulations. Then, in chapter 3, we will discuss boron-based 2D materials, i.e. (i) borophene and (ii) BSLs: in (i) we analyze the electronic properties of the pristine phases of borophene and connect them with the structural properties obtained by the XANES simulations, and in (ii) we investigate the electronic, structural properties and the confinement effects of electronic confinement of BSLs; in chapter 4, we present perspectives for borophene studies. Chapters 5 and 6 are the results of carbon-based materials. The chapter 5 we present the results of our theoretical studies combined with an experimental collaboration (LNNano/CNPEM). Here we unveil the dominance of vdW interaction over the hydrogen bonds in pristine cellulose nanofibers and that the disruption of CNFs occurs due to the formation of carboxylate groups, that weaken the hydrogen bonds. In chapter 6, where we investigate two different nanocellulose - graphene interfaces, it was found that the binding energy of nCL/G is comparable with BN/Graphene, these systems fingerprints through XANES simulations and we unveil a net charge accumulation in the nCL/G interface and its increases with an external electric field and pressure. Then the Appendix has some important information used in this work.

2 Methodology

One of the greatest challenges of our days is the uninterrupted search for new materials, that somehow give useful properties to the community. And technology advances thru the years showed us new findings and materials, and those findings and materials lead to the need for new techniques and the enhancement of known techniques, just to this - understand and improve these new materials.

In the early's 2000, Novoselov and Geim(1) wins the Nobel prize due to graphene synthesis. And then, a new era in materials science has begun. Materials like own graphene, borophene (6), silicene (10), germanene (12), and others are successfully synthesized. And we can say that the Density Functional Theory (DFT) is a powerful tool to study these materials. In this chapter, we will show a brief description of this method, which helped in this work.

2.1 Density Functional Theory (DFT)

In a many-body system, a way to solve the problem is using the total electronic charge density $\rho(\boldsymbol{r})$. To this, Scrödinger's equation for N electrons and the wavefunction with N variables (in this case without taking into consideration the spin), can be written just with three variables. Thomas, Fermi and Dirac's ideas (66, 67, 68) led to DFT as we know it today. In 1964, Walter Kohn and Pierre Hohemberg published the article that mark the beginning of DFT. Then, the next year, Walter Kohn and Lu Jeu Sham published another article on the development of self-consistent equations and exchange-correlation effects.

So there was a notable growth of DFT's application in atoms, molecules and solids, and it's one of the most popular methods to calculate electronic, structural, and other properties of a system. The main idea of DFT is that any property of a many-body system can be described by a single electronic density functional $\rho(\boldsymbol{r})$, carried by Kohn-Sham theorems, shown next.

2.1.1 The Schrödinger Equation

Any dynamic system's state can be described through the Schrödinger equation, as any problem in which electronic structure is involved. Here we will start our point of time-independent Schrödinger equation. For an isolated system containing N electrons and taking into consideration the Born-Oppenheimer approximation (appendix), then we have:

$$\hat{H}\Psi = E\Psi, \tag{2.1}$$

where E is the electronic energy of system, $\Psi = \Psi(\boldsymbol{r}_1, \boldsymbol{r}_2, \ \dots \ , \boldsymbol{r}_N)$ is the wavefunction, and $\hat{H}$ is the Hamiltonian operator given by:

$$\hat{H} = \sum_{i=1}^{N} \left(-\frac{1}{2}\nabla_i^2\right) + \sum_{i=1}^{N} \upsilon(\boldsymbol{r}_i) + \sum_{i<j}^{N} \frac{1}{\boldsymbol{r}_{ij}} = \hat{T} + \hat{V}_{ne} + \hat{V}_{ee}, \tag{2.2}$$

$$\hat{H} = \hat{T} + \hat{V}_{ne} + \hat{V}_{ee}. \tag{2.3}$$

The term

$$\upsilon(\boldsymbol{r}_i) = -\sum_{\alpha} \frac{Z_\alpha}{\boldsymbol{r}_{i\alpha}}, \tag{2.4}$$

represents the external electric potential in each electron i . The electronic coordinates $\boldsymbol{x}_i$ are related with spatial coordinates $\boldsymbol{r}_i$.

2.1.2 Thomas-Fermi-Dirac Approximation

L. Thomas (66) and E. Fermi (67) pioneered the development of DFT calculations. Both works didn't present an accurate precision as a "modern DFT", but showed the way to how calculations should proceed. In this method, the kinetic energy of the system is approximately an explicit functional of electronic density, like a non-interacting electrons system in a homogeneous gas, with a density equal to a local density at any point of the system. In this approach, P. Dirac (68) corrected a detail that passed by. It was the exchange and correlation effects, formulated in 1930, taking into consideration the local approximation, and is still used nowadays (69, 70).

Here, the energy is given by:

$$E_{TF}[\rho] = C_1 \int d^3\boldsymbol{r}\ n(\boldsymbol{r})^{(\frac{5}{3})} + \int d^3(\boldsymbol{r}\ V_{ext}(\boldsymbol{r})n(\boldsymbol{r}) + C_2 \int d^3r\ n(\boldsymbol{r})^{(\frac{4}{3})}$$
$$+\frac{1}{2} \int d^3\boldsymbol{r}\ d^3\boldsymbol{r}' \frac{n(\boldsymbol{r})n(\boldsymbol{r}')}{|\boldsymbol{r} - \boldsymbol{r}'|}. \tag{2.5}$$

The first term is the local approximation for kinetic energy, with $C_1 = 2,871$ (u. a.), and the third term is the local exchange, with $C_2 = -\frac{3}{4}(\frac{3}{\pi})^{1/3}$, and the last term is the classical electrostatic Hartree energy. Energy and density of ground state can be found minimizing functional $E[\rho]$ in (2.1.2) to all possible density subjected to restrictions on the total amount of electrons

$$\int \rho(\boldsymbol{r}) d^3\boldsymbol{r} = N. \tag{2.6}$$

Using the Lagrange multiplier, the solution can be found through a functional minimization, such that:

$$\Omega_{TF}[\rho] = E_{TF}[\rho] - \mu \left\{ \int \rho(\boldsymbol{r}) d^3\boldsymbol{r} - N \right\}, \tag{2.7}$$

where Lagrange multiplier μ is the Fermi energy.

2.1.3 Hohemberg and Kohn Theorems

Hohemberg and Kohn published an article in 1964 - the article that was the "beginning of modern DFT" (71). This paper contains the two main pillars of DFT calculations, which can be proved simply. This is the heart of DFT. The theorem shows that from the system's electronic density ground-state, it is possible to get exactly the ground-state energy.

For this, we consider a system with N electrons, being $\boldsymbol{r}_i = (\boldsymbol{x}_i, \boldsymbol{y}_i, \boldsymbol{z}_i)$ the position vector of i-th electron. The first theorem says:

"For any system of interacting particles in an external potential V_{ee}, the potential V_{ee}, is determined uniquely, except for a constant, by the ground state particle density $\rho_0(\boldsymbol{r})$."

In other words, the ground-state energy from Schrödinger's equation is a unique functional of electron density (72). To the proof, we will consider the Ψ state as the ground-state, characterized by a Hamiltonian $\hat{H}$. This Hamiltonian in question is represented by equation (2.3). In this equation, the first term represents the electron's kinetic energy, and the terms $\hat{V}_{ne}$ and $\hat{V}_{ee}$ the nuclei-electron and electron-electron potential energy. Assuming that there is a second external potential $\upsilon'(\boldsymbol{r})$ that leads to $\hat{H}'$ and a second ground-state namely Ψ'. Here will be considered the hypothesis that both states lead to the same electronic density $\rho(\boldsymbol{r})$, and all states aren't degenerated[1].

By Variational Principle [2], we have:

$$E = \langle\Psi|\hat{H}|\Psi\rangle < \langle\Psi'|\hat{H}|\Psi'\rangle, \tag{2.8}$$

$$E' = \langle\Psi'|\hat{H}|\Psi'\rangle < \langle\Psi|\hat{H}|\Psi\rangle. \tag{2.9}$$

$$E = \langle\Psi|\hat{T} + \hat{V}_{ee} + \hat{V}_{ne}|\Psi\rangle < \langle\Psi'|\hat{T} + \hat{V}_{ee} + \hat{V}_{ne}|\Psi'\rangle, \tag{2.10}$$

$$E' = \langle\Psi'|\hat{T} + \hat{V}_{ee} + \hat{V}'_{ne}|\Psi'\rangle < \langle\Psi|\hat{T} + \hat{V}_{ee} + \hat{V}'_{ne}|\Psi\rangle, \tag{2.11}$$

or

$$E = \langle\Psi|\hat{H}|\Psi\rangle < \langle\Psi'|\hat{H}|\Psi'\rangle = \langle\Psi'|\hat{H}|\Psi'\rangle < \langle\Psi|\hat{V}_{ne} - \hat{V}'_{ne}|\Psi\rangle. \tag{2.12}$$

Knowing that:

$$\rho(\boldsymbol{r}) = \langle\Psi|\sum_{i=1}^{N}\delta(\boldsymbol{r} - \boldsymbol{r}_i)|\Psi\rangle, \tag{2.13}$$

$$\hat{V}_{ne} = \sum_{i=1}^{N}\upsilon(\boldsymbol{r}_i), \tag{2.14}$$

we have

$$\langle\Psi|\hat{V}_{ne}|\Psi\rangle = \sum_{i=1}^{N}\int d^3\boldsymbol{r}_1 ... \int d^3\boldsymbol{r}_N \Psi^*(\boldsymbol{r}_1, ..., \boldsymbol{r}_N)\upsilon(\boldsymbol{r}_i)\Psi(\boldsymbol{r}_1\boldsymbol{r}_N), \tag{2.15}$$

or

$$\langle\Psi|\hat{V}_{ne}|\Psi\rangle = \sum_{i=1}^{N}\int d^3\boldsymbol{r}\int d^3\boldsymbol{r}_1 \, ... \, d^3\boldsymbol{r}_i\upsilon(\boldsymbol{r})\delta(\boldsymbol{r} - \boldsymbol{r}_i)\int d^3\boldsymbol{r}_{i+1} ... \int d^3\boldsymbol{r}_n\Psi\Psi^*, \tag{2.16}$$

---

[1] This proof can be extended for degenerated systems too.

[2] Appendix C.

$$\langle\Psi|\hat{V}_{ne}|\Psi\rangle = \int \rho(\boldsymbol{r})\upsilon(\boldsymbol{r})d^3\boldsymbol{r}. \tag{2.17}$$

Using equation (2.17) result in equation (2.12), we will obtain the following result:

$$E < E' + \int [\upsilon(\boldsymbol{r}) - \upsilon'(\boldsymbol{r})]\rho(\boldsymbol{r})d^3\boldsymbol{r}. \tag{2.18}$$

Doing the same operation for $E' = \langle\Psi'|\hat{H}|\Psi'\rangle$,

$$E' < E + \int [\upsilon'(\boldsymbol{r}) - \upsilon(\boldsymbol{r})]\rho(\boldsymbol{r})d^3\boldsymbol{r}. \tag{2.19}$$

So we have:

$$E + E' < E' + E. \tag{2.20}$$

To begin the proof, we have assumed the same density ρ for $\upsilon \neq \upsilon'$, and now, we faced a contradiction due $\Psi \neq \Psi'$. So we conclude the unicity demands consider $\Psi = \Psi'$. The first theorem says that ground-state density should contain the same information as the state in question. This makes it a unique density functional, proving it by *reductio ad absurdum*.

This theorem leads to a corollary, that implies "Since the Hamiltonian is thus fully determined except for a constant shift of the energy, it follows that the many-body wavefunctions for all states (ground and excited) are determined. Therefore, all properties of the system are completely determined given only the ground state density $\rho_0(\boldsymbol{r})$". Then, in principle, the wavefunction of any state is determined by solving the Schrödinger equation with this Hamiltonian. Among all solutions consistent with the given density, the unique ground state wavefunction is the one that has the lowest energy.

The second theorem says *"A universal functional for the energy $E[\rho]$ in terms of the density $\rho(\boldsymbol{r})$ can be defined, valid for any external potential $\upsilon(\boldsymbol{r}_i)$. For any particular $\upsilon(\boldsymbol{r}_i)$, the exact ground state energy of the system $E_0[\rho]$ is the global minimum value for this functional, and the density $\rho(\boldsymbol{r})$ that minimizes the functional is the exact ground state density $\rho_0(\boldsymbol{r})$."*, or:

$$E[\rho] = \langle\Psi|\hat{H}|\Psi\rangle. \tag{2.21}$$

Here we will treat $\rho(r)$ as the density of some determined state Ψ, unnecessarily coming from $\hat{H}$, that in this case is ρ_0. This takes us to two scenarios:

- $\rho \neq \rho_0 \rightarrow \Psi \neq \Psi_0 \implies E > E_0$;
- $\rho = \rho_0 \rightarrow \Psi = \Psi_0 \implies E = E_0$.

The second theorem confirms that $E[\rho]$ is a $\rho(\boldsymbol{r})$ functional, and its value is the minimum obtained through ground-state density. Rewriting (2.21) and combining with (2.3), we have now:

$$E[\rho] = \langle\Psi|\hat{T} + \hat{V}_{ee}|\Psi\rangle + \langle\Psi|\hat{V}_{ne}|\Psi\rangle. \tag{2.22}$$

The term $\langle\Psi|\hat{T} + \hat{V}_{ee}|\Psi\rangle$ is a well-known universal functional, valid for any coulombian system, that can be written as $F[\rho]$. The term $\langle\Psi|\hat{V}_{ne}|\Psi\rangle$ depends on each system. So we have:

$$E[\rho] = F[\rho] + \langle\Psi|\hat{V}_{ne}|\Psi\rangle. \tag{2.23}$$

Similarly to ground-state:

$$E[\rho_0] = F[\rho_0] + \langle\Psi_0|\hat{V}_{ne}|\Psi_0\rangle, \tag{2.24}$$

where Ψ_0 is the ground-state wavefunction. As ρ_0 determines Ψ_0, and ρ determines Ψ, and assuming that either ρ_0 or another ρ are determined for some external potential, we can apply the variational principle, and then obtain:

$$E[\Psi_0] < E[\Psi], \tag{2.25}$$

$$F[\rho_0] + \langle\Psi_0|\hat{V}_{ne}|\Psi_0\rangle < F[\rho] + \langle\Psi|\hat{V}_{ne}|\Psi\rangle, \tag{2.26}$$

$$E[\rho_0] < E[\rho]. \tag{2.27}$$

So we prove the second theorem. This theorem leads to another corollary, The functional $E[\rho]$ alone is sufficient to determine the exact ground state energy and density. In general, the excited states of the electrons must be determined by other means.

2.1.4 Kohn-Sham Equations

Both theorems proposed by Hohemberg and Kohn couldn't establish a way to find some functional related to ground-state energy. In 1965, Kohn and Sham formulated a new procedure that will give a self-consistent equations system (73). The solution will return the density that minimizes the ground state energy functional, and this is one of the reasons that DFT is one of the most popular methods for electronic structure calculations - due to this approximation. The idea of replacing the initial many-body problem with an auxiliary problem of independent particles was an accurate shot that leads to the exact result of properties of a many-body system, even when using a single particle system - an *ansatz* (69).

The *ansatz* has two main ideas: the exact many-body ground-state energy system can be represented by an auxiliary single-particle ground-state density, and the single-particle's Hamiltonian is chosen having a kinetic energy operator and an effective potential V_{KS}.

These ideas will lead to an approximation that makes a $3N$ variables problem to other single-particle problem but with N equations.

Using the energy eigenvalue given by equation (2.3), it is possible to write the electron's kinetic energy as

$$T = T[\rho] = T_s[\rho] + T_C[\rho], \tag{2.28}$$

where $T_s[\rho]$ is the kinetic energy of non-interacting electrons, $T_C[\rho]$ is the amount of kinetic energy due electronic correlation. Proceeding, we have:

$$V_{ee} = V_{ee}[\rho] = V_{ee_H}[\rho] + V_{ee_X}[\rho] + V_{ee_C}[\rho], \tag{2.29}$$

where V_{ee_H} is the electron-electron interaction potential energy, also known as *Hartree energy*, that can be described by the following equation:

$$V_{ee_H} = \frac{e^2}{2}\int d^3\boldsymbol{r}\int d^3\boldsymbol{r}'\frac{\rho(\boldsymbol{r})\rho(\boldsymbol{r}')}{|\boldsymbol{r}-\boldsymbol{r}'|}. \tag{2.30}$$

The exchange term $V_{ee_X}[\rho]$ is represented by:

$$V_{ee_X}[\rho] = -\frac{e^2}{2}\sum_{jk}\int d^3\boldsymbol{r}\int d^3\boldsymbol{r}'\frac{\phi_j^*(\boldsymbol{r})\phi_k^*(\boldsymbol{r}')\phi_j(\boldsymbol{r}')\phi_k(\boldsymbol{r})}{|\boldsymbol{r}-\boldsymbol{r}'|}, \tag{2.31}$$

$\phi(\boldsymbol{r})$ represents the particle eigenvalues. In equation (2.29), still there is an unknown correlation term, $V_{ee_C}[\rho]$. With all terms, it is possible to rewrite the total energy of the system as:

$$E[\rho] = T_s[\rho] + T_C[\rho] + V_{ee_H}[\rho] + V_{ee_X}[\rho] + V_{ee_C}[\rho] + V_{ne}[\rho]. \tag{2.32}$$

The term $V_{ne}[\rho]$ is equivalent to $\int \rho(\boldsymbol{r})\upsilon(\boldsymbol{r})d^3\boldsymbol{r}$. The next step is to try an equation simplification, grouping all of them in a new term, which will be called $E_{XC}[\rho]$, the exchange-correlation energies, such as:

$$T_C[\rho] + V_{ee_X}[\rho] + V_{ee_C}[\rho] = E_{XC}[\rho]. \tag{2.33}$$

Now, the total energy will assume the following form:

$$E[\rho] = T_s[\rho] + V_{ee_H}[\rho] + V_{ne}[\rho] + E_{XC}[\rho]. \tag{2.34}$$

This simplification allows us to group all terms we didn't know, like (2.32), in only one term $E_{XC}[\rho]$. The kinetic energy term of a non-interacting electrons system has only one known scheme (74) given by:

$$T_s[\rho] = -\frac{\hbar^2}{2m}\sum_i^N\int d^3\boldsymbol{r}\phi_i^*(\boldsymbol{r})\nabla^2\phi_i(\boldsymbol{r}). \tag{2.35}$$

All terms in which exchange and correlation effects are involved will be in $E_{XC}[\rho]$. There's no one exact expression for this term.

We could find the total energy and electronic ground-state density if we know the exchange-correlation energy term (2.33). To solve this so, the Hohemberg-Kohn theorems will help: the ground-state energy will be obtained through (2.33) minimization with relation to electronic density, taking into consideration the orthogonality of non-interacting system:

$$\int \phi_i^*(\boldsymbol{r})\phi_j(\boldsymbol{r})d^3\boldsymbol{r} = \delta_{ij}. \tag{2.36}$$

By Lagrangian multipliers, we can minimize the equation above, so that:

$$\mathcal{L} = E[\rho] - \sum_i \varepsilon_i \int \phi_i^*(\boldsymbol{r})\phi_j(\boldsymbol{r})d^3\boldsymbol{r}, \tag{2.37}$$

where ε_i are the Lagrangian multipliers. Minimize $\mathcal{L}$ means

$$\frac{\delta\mathcal{L}}{\delta\phi_i(\boldsymbol{r})} = 0, \tag{2.38}$$

and then:

$$\frac{\delta E[\rho]}{\delta\phi_i^*(\boldsymbol{r})} = \frac{\delta T_s[\rho]}{\delta\phi_i^*(\boldsymbol{r})} + \left[\frac{\delta V_{ee_H}}{\delta\rho(\boldsymbol{r})} + \frac{\delta V_{ne}}{\delta\rho(\boldsymbol{r})} + \frac{\delta E_{xc}}{\delta\rho(\boldsymbol{r})}\right] + \frac{\rho(\boldsymbol{r})}{\delta\phi_i^*(\boldsymbol{r})}, \tag{2.39}$$

where the electronic density of a single-particle system will be:

$$\rho_s(\boldsymbol{r}) = \sum_j \delta\phi_j^*(\boldsymbol{r})\delta\phi_j(\boldsymbol{r}). \tag{2.40}$$

At the same time, to kinetic energy term ((2.35) equation) we will have:

$$\frac{\delta\rho(\boldsymbol{r})}{\delta\phi_j^*(\boldsymbol{r})}, \tag{2.41}$$

$$\frac{\delta T_s[\rho]}{\delta\phi_i^*(\boldsymbol{r})} = -\frac{\hbar^2}{2m}\nabla^2\phi_i(\boldsymbol{r}), \tag{2.42}$$

where the index i refers to some specific state of the single-particle system. to get these expressions, we need to apply the definition of a functional derivative[3].

Following the term where are the Lagrangian multipliers, we have:

$$\frac{\delta}{\delta\phi_j^*(\boldsymbol{r})}\left(\sum_i \varepsilon_i \int \delta\phi_j^*(\boldsymbol{r})\delta\phi_j(\boldsymbol{r})d^3\boldsymbol{r}\right) = \varepsilon_i\phi_r(\boldsymbol{r}). \tag{2.43}$$

From equation (2.37):

$$-\frac{\hbar^2}{2m}\nabla^2\phi_i(\boldsymbol{r}) + \left[\frac{\delta V_{ee_H}}{\delta\rho(\boldsymbol{r})} + \frac{\delta V_{ne}}{\delta\rho(\boldsymbol{r})} + \frac{\delta E_{xc}}{\delta\rho(\boldsymbol{r})}\right]\phi_i(\boldsymbol{r}) - \varepsilon_i\phi_r(\boldsymbol{r}) = 0, \tag{2.44}$$

$$\left[-\frac{\hbar^2}{2m}\nabla^2 + v_H(\boldsymbol{r}) + v(\boldsymbol{r}) + v_{XC}(\boldsymbol{r})\right]\phi_i(\boldsymbol{r}) = \varepsilon_i\phi_r(\boldsymbol{r}), \tag{2.45}$$

where $v_H(\boldsymbol{r}) \equiv \frac{\delta V_{ee_H}}{\delta\rho(\boldsymbol{r})}$, $v(\boldsymbol{r}) \equiv \frac{\delta V_{ne}}{\delta\rho(\boldsymbol{r})}$ e $v_{XC}(\boldsymbol{r}) \equiv \frac{\delta E_{xc}}{\delta\rho(\boldsymbol{r})}$. Now we can calculate the electronic density of an interacting system in a $v(\boldsymbol{r})$ potential described by the Schrödinger Equation

---

[3] see Appendix B.

and by the solution of a non-interacting system in a $v_S(\boldsymbol{r}) = v_H(\boldsymbol{r}) + v(\boldsymbol{r}) + v_{XC}$ potential. For the non-interacting system, we have:

$$\left[-\frac{\hbar^2}{2m}\nabla^2 + v_S(\boldsymbol{r})\right]\phi_i(\boldsymbol{r}) = \varepsilon_i\phi_i(\boldsymbol{r}) \tag{2.46}$$

$$\rho(\boldsymbol{r}) \equiv \rho_S(\boldsymbol{r}) = \sum_i^{occu} |\phi_i(\boldsymbol{r})|^2. \tag{2.47}$$

Equations (2.46) and (2.47) are the ***Kohn-Sham equations***. Through them, is possible to obtain the electronic density of the ground-state electronic density of interacting electrons by the electron density of a system of non-interacting electrons that are submitted to an effective potential $\rho_s = V_{KS}$ solving the equations of Kohn-Sham.

Getting ρ_0, the total energy will be given by:

$$E[\rho_0] = T_S[\rho_0] + V_{ne_H}[\rho_0] + V_{ee}[\rho_0] + E_{XC}[\rho_0] \tag{2.48}$$

with

$$V_{ee}[\rho_0] = \int d^3\boldsymbol{r}v(\boldsymbol{r})\rho_0(\boldsymbol{r}) \tag{2.49}$$

$$= \int d^3\boldsymbol{r}[v_S(\boldsymbol{r}) - v_H(\boldsymbol{r}) - v_{XC}(\boldsymbol{r})]\rho_0(\boldsymbol{r}) = V_S[\rho_0] - \int d^3\boldsymbol{r}[v_H(\boldsymbol{r}) - v_{XC}(\boldsymbol{r})]\rho_0(\boldsymbol{r}). \tag{2.50}$$

So, the total energy will be:

$$E_0 = \sum_i^{occu} \varepsilon_i - \frac{e^2}{2}\int d^3\boldsymbol{r}\int d^3\boldsymbol{r}'\frac{\rho(\boldsymbol{r})\rho(\boldsymbol{r}')}{|\boldsymbol{r}-\boldsymbol{r}'|} - \int d^3\boldsymbol{r}[v_H(\boldsymbol{r}) - v_{XC}(\boldsymbol{r})]\rho_0(\boldsymbol{r}) + E_{XC}[\rho_0], \tag{2.51}$$

where the non-interacting system energy is:

$$E_S = \sum_i^{occu} \varepsilon_i = T_S[\rho_0] + V_S[\rho_0]. \tag{2.52}$$

Kohn-Sham equations are solved by a self-consistent field procedure, where initially we propose an electronic density, that through it, will be possible to solve v_S potential and solve (2.46). The next step is to calculate the electronic density by (2.47). Using convergence criteria, expanded in the next subsection (2.1.5), this will lead to a new final density to the system, and then, getting all observables.

2.1.5 The Self-Consistent Field (SCF)

How the Kohn-Sham potential V_{KS} depends on electronic density, and this density is calculated by Kohn-Sham potential, the solution to this equation is known as self-consistent, which is based on the use of an initial density ρ_0, built by a sum of atomic densities, such we have:

$$\rho_0(\boldsymbol{r}) = \sum_\alpha \rho_\alpha(\boldsymbol{r}_\alpha - \boldsymbol{R}_\alpha), \tag{2.53}$$

where ρ_α represents the atomic density of atom α and $\boldsymbol{R}$ the position of this atom.

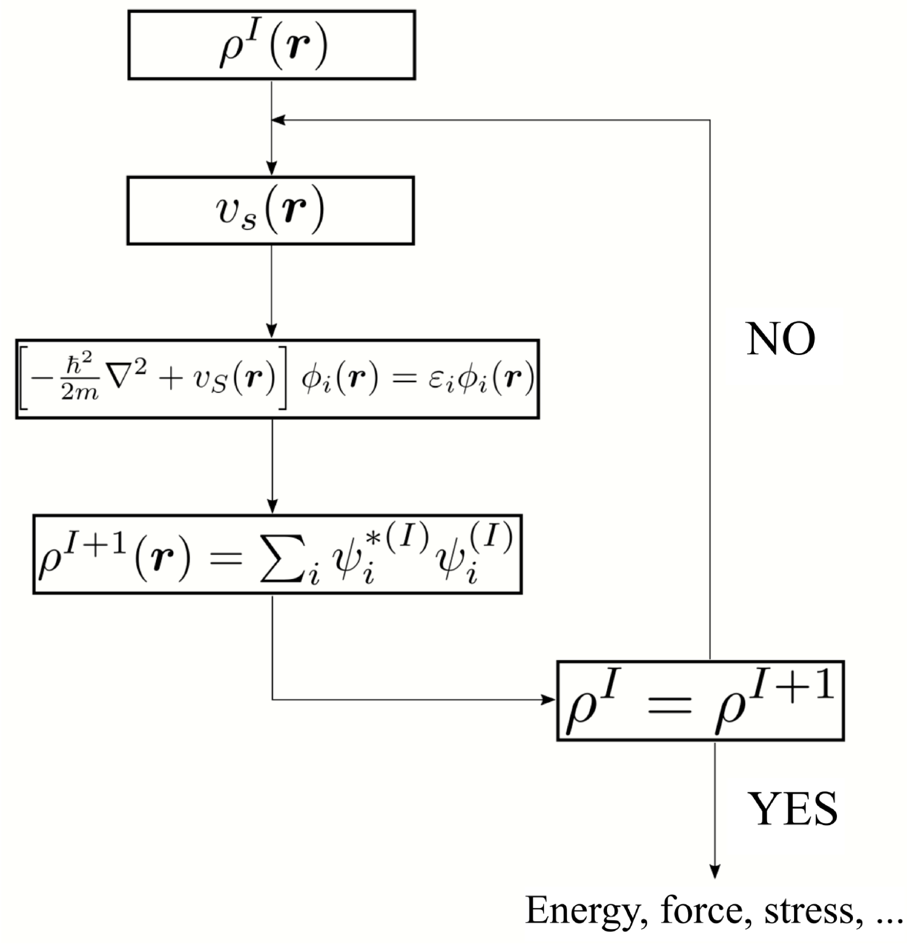

Figure 8 – The self-consistent field procedure.

This initial density will be the kickstart of Kohn-Sham's potential calculations. From this potential, the diagonalization of the Hamiltonian matrix $\hat{H}_{KS}$ begins, in some convenient base. Once the Kohn-Sham orbitals are found, the electron density of the system is obtained. The self-consistent field is over when a convergence criterion is satisfied. Usually, these criteria are based on the total energy difference, when reaches convergence for $|E^{(i)} - E^{(i-1)}| < \rho$. If this criterion isn't satisfied yet, the SCF cycle is restarted, but with a new density. The cycle repeats until convergence is reached. In figure 8, we have an expanded picture of the SCF procedure.

2.2 Approximations and Functionals

As we mentioned previously, some problems that happen due to many-body effects are summarized in a single term, namely E_{XC}. And now the determination of this term is substantial to the correct DFT's behaviour. As there is no well-defined expression for the exchange and correlation term, we use some approximations for this term that are necessary.

2.2.1 LDA Approximation

Given the need for an approximation to the exchange-correlation term, Kohn and Sham (73) proposed this approximation. It's quite simple and there is a physical motivation. Anchored in previous work from Thomas and Fermi (75), the Local Density Approximation (LDA) considers that each region of the space of the system has an infinitesimal volume that can be treated as a homogeneous electron gas. The exchange and correlation energy is given by:

$$E_{XC}^{LDA}[\rho] = \int \rho(\boldsymbol{r})\varepsilon_{XC}(\rho(\boldsymbol{r}))d^3\boldsymbol{r}, \tag{2.54}$$

where $\varepsilon_{XC}(\rho)$ is the exchange-correlation/particle of a homogeneous electron gas with density ρ. The exchange-correlation potential $v_{XC}(\boldsymbol{r})$ now will be written as:

$$v_{XC}^{LDA}(\boldsymbol{r}) = \frac{\delta E_{XC}}{\delta\rho(\boldsymbol{r})} = \varepsilon_{XC}(\rho(\boldsymbol{r})) + \rho(\boldsymbol{r})\frac{\partial\varepsilon_{XC}(\rho)}{\partial\rho}, \tag{2.55}$$

as the equation (2.47) will be rewritten as:

$$\left[-\frac{\hbar^2}{2m}\nabla^2 + v(\boldsymbol{r}) + \frac{\rho(\boldsymbol{r}')}{|\boldsymbol{r}-\boldsymbol{r}'|}d^3(\boldsymbol{r}') + \varepsilon_{XC}^{LDA}(\boldsymbol{r})\right]\phi_i(\boldsymbol{r}) = \varepsilon_i\phi_i(\boldsymbol{r}). \tag{2.56}$$

The self-consistent solution of equation (2.56) defines the Kohn-Sham local density approximation, which is commonly known as LDA. The LDA depreciates the correlation energy, otherwise, overestimates the exchange factor. In inhomogeneous systems, i.e., $\rho(\boldsymbol{r})$ isn't completely uniform, and LDA shows weak results. To balance this problem, the functional $E_{XC}[\rho]$ should be expressed in terms of the total charge density gradient.

2.2.2 GGA Approximation

If the electronic density is non-uniform, we will use a trick that consists in express the exchange-correlation functional $E_{XC}[\rho]$ in terms of the electronic density gradient, such this functional carries information of electronic density inhomogeneity. This method is better known as Generalized Gradient Approximation. The exchange-correlation term is written as:

$$E_{XC}^{GGA}[\rho] = \int f^{GGA}(\rho(\boldsymbol{r}), \nabla\rho(\boldsymbol{r}))d^3\boldsymbol{r}. \tag{2.57}$$

The term $f^{GGA}(\rho(\boldsymbol{r}), \nabla(\boldsymbol{r}))$ is numerically calculated by parametrizations. One of the most used parametrizations is the PBE functional, proposed by John Perdew, Kieron Burke e Matthias Ernzerhof (76).

2.2.3 PBE Functional

A functional is defined by a rule or application that takes a function to a number (74). The PBE functional is the most simple GGA (69) (77). The way this functional satisfies the conditions in reference (76) is:

$$E_C^{GGA-PBE}[\rho(\boldsymbol{r}), \nabla(\boldsymbol{r})] = \int \rho(\boldsymbol{r})[\varepsilon_C(\boldsymbol{r}_s, \zeta) + H(\boldsymbol{r}_s, \zeta, t)d^3\boldsymbol{r}, \tag{2.58}$$

where $\zeta = \frac{\rho^{\uparrow}-\rho^{\downarrow}}{\rho(\boldsymbol{r})}$ is the spin polarization, $\boldsymbol{r}_s$ is the local value of the density parameter and t is the dimensionless gradient given by:

$$\frac{|\nabla\rho(\boldsymbol{r})|}{2\phi k_{TF}\rho(\boldsymbol{r})}. \tag{2.59}$$

Here, $\phi = ((1+\zeta)^{2/3} + (1+\zeta)^{2/3})/2$. The final form of H is:

$$H = \frac{e^2}{a_0}\gamma\phi^3 \ln\left(1 + \frac{\beta}{\gamma}t^2 \frac{1+At^2}{1+At^2+A^2t^4}\right), \tag{2.60}$$

where the factor e^2/a_0 is the default unit in atomic units (a_0 is the Bohr radius), β and γ are numbers that their values is respectively$\simeq 0,066725$ and $(1-\ln 2)/\pi^2 \simeq 0,031091$, and A is:

$$A = \frac{\beta}{\gamma}\left[exp\frac{-\varepsilon_C^{hom}}{\gamma\beta^3\frac{e^2}{a_0}} - 1\right]^{-1}. \tag{2.61}$$

2.2.4 van der Waals Density Functionals

Usually, in non-homogeneous systems, semi-local approximations are the most appropriate. In some molecules and materials, local and semilocal density functionals can describe very well the interaction effects, such as cohesion, bond lengths, and other properties. Nonetheless, for more dispersed systems, such as molecular crystals and layered materials, nonlocal and long-range interactions such as van der Waals forces are critical. The first decade of the 21st century saw the development of two vdW functionals. The objective of the vdW-DF is to provide, within the DFT, an efficient method for calculating the non-local effects of vdW for all systems electronics. The interactions of vdW in vdW-DF are approximated non-empirically, based on the many-body physics and general physical laws. Here we will present a brief discussion of the vdW corrections that we used in this work.

2.2.4.1 vdW-D2

In the DFT-D2 method, the total energy is given by:

$$E_{DFT-D} = E_{KS-DFT} + E_{\text{disp}} \tag{2.62}$$

where E_{KS-DFT} is the usual self-consistent Kohn–Sham energy, and E_{disp} is an empirical dispersion correction is given by:

$$E_{\text{disp}} = -s_6 \sum_{i=1}^{N_{at}-1} \sum_{j=i+1}^{N_{at}} \frac{C_6^{ij}}{R_6^{ij}} f_{\text{dmp}}(\boldsymbol{R}_{ij}), \tag{2.63}$$

where N_{at} is the number of atoms in the system, C_6 denotes the dispersion coefficient for atom pair ij,s_6 is a global scaling factor that only depends on the DF used, R^{ij} is an interatomic distance, and f_{dmp} is a Fermi-type damping function that must be used to avoid near-singularities for small $\boldsymbol{R}$ (78).

2.2.4.2 vdW-DF

The vdW-DF consists of different contributions to the exchange and correlation functional, where

$$E_{XC}[\rho] = E_X^{revPBE}[\rho] + E_C[\rho], \tag{2.64}$$

where the correlation energy E_C can be split into two pieces:

$$E_C^{LDA}[\rho] + E_C^{nl}[\rho]. \tag{2.65}$$

The terms $E_X^{revPBE}[\rho]$ and $E_C^{LDA}[\rho]$ respectively represent the functional of revPBE exchange and the LDA correlation energy. The interaction of vdW is given by the non-local correction $E_C^{nl}[\rho]$ for the correlation only electronics, since for two spatially separated systems it is possible to distinguish the electrons as belonging to one or another system. The simplest way to write the nonlocal correlation energy is given by the adiabatic connection, being

$$E_C^{nl}[\rho] = \frac{1}{2}\int d\boldsymbol{r}d\boldsymbol{r}'\rho(\boldsymbol{r})\phi(\boldsymbol{r},\boldsymbol{r}')\rho(\boldsymbol{r}'), \tag{2.66}$$

where $\phi(\boldsymbol{r},\boldsymbol{r}')$ is a function that depends on $(\boldsymbol{r}-\boldsymbol{r}')$ and the density ρ in the close to $\boldsymbol{r}$ and $\boldsymbol{r}'$.

The term E_C^{nl} is treated in the full potential approximation, which is exact at long distances between separated fragments, and then it can be written as:

$$E_C^{nl} = \int_0^\infty \frac{du}{4\pi} tr[\ln(1 - V\tilde{\chi}) - \ln \epsilon], \tag{2.67}$$

where $\tilde{\chi}$ is the density response to a fully self-consistent potential with long-range, V is the interelectronic Coulomb interaction, ϵ is an appropriately approximated dielectric function, and u is the imaginary frequency (79, 80).

2.2.4.3 vdW-DF2

For arbitrary geometries, vdW-DF reveals a good response when compared especially with other non-empirical methods. Although, it overestimates equilibrium separations and underestimates hydrogen-bond strength. The idea behind the vdW-DF2 is to employ a more accurate semilocal exchange functional and the use of a large-N asymptote gradient correction in determining the vdW kernel, such this correction improves equilibrium separations, hydrogen-bonds strength and vdW attractions at intermediate separations longer than the equilibrium ones.

The first change is to replace the exchange term coming from Perdew-Burke-Ernzerhof (revPBE) with PW86 because revPBE is generally too repulsive near the equilibrium separation, and can bind spuriously by exchange alone, although less so than most other local or semilocal functionals. For the E_C^{nl} term, now we have the inclusion of a long-range piece of the correlation energy $E_C^{nl}[\rho]$, a fully nonlocal functional of the density $[\rho]$ (81).

The nonlocal piece of the correlation energy in vdW-DF2 is of the form:

$$E_C^{nl}[\rho] = \int d^3r \int d^3r' \rho(\boldsymbol{r})\phi(\boldsymbol{r}, \boldsymbol{r}')\rho(\boldsymbol{r}'). \tag{2.68}$$

2.2.4.4 optB86b-vdW

Original vdW-DF similarly overestimates lattice constants to how it overestimates binding distances for gas-phase dimers. However, some of the modified vdW functionals lead to average errors which are similar to those of PBE or better.

Factors such as the equilibrium separation overestimated and hydrogen-bond underestimated in vdW-DF led this method to several modifications focused on both the exchange and correlation parts. This functional gives a special look to solid-state properties of materials and gives an accuracy similar to other functional (optB88-vdW) which is good for weakly bonded gas phase dimers and has improved asymptotic behaviour. From detailed studies of the exchange functionals and binding curves, it became apparent that the behaviour of the exchange enhancement factor (F_x) for small reduced density gradients (s) affects the position of the repulsive Pauli wall (82).

The form of the optB86b functional is given by:

$$F_x^{\text{optB86b}} = 1 + \frac{\mu s^2}{(1 + \mu s^2)^{4/5}}, \quad \mu = 0.1234 \tag{2.69}$$

2.2.5 Pseudopotentials

Despite numerous facilities for performing the calculations, DFT faces a slight complication: the high computational cost for calculations in systems with a large number of atoms, especially for atoms with many electrons. As there are also numerous systems with many atoms, there was a need to develop a method to circumvent this problem. Then, there was the development of pseudopotentials. Pseudopotentials take into account that only valence electrons participate in bonds, thus reducing the number of electrons that will participate in the calculation.

The electrons are classified in the pseudopotentials as core electrons, inert, composed of the electrons of the inner layers and the nucleus, and valence electrons, being those who participate mainly in the properties of solids and molecules, and the DFT calculations, as previously mentioned. Like electrons, pseudopotentials are also classified according to their obtainment. The first group of pseudopotentials are the empirical potentials, which were obtained through experimental parameters, and the second group of pseudopotentials is composed of those that were obtained by *ab-initio* calculations by the solution of the self-consistent equation of the Schrödinger equation.

Covering the discussion for first principles pseudopotentials, we can include a few subcategories, such as the conserved norm pseudopotentials (83), the soft pseudopotentials (84) and the ultra-soft pseudopotentials (85). We can also include a subcategory known as Projector Augmented-Wave (PAW) (86, 87). We do not exactly consider the PAW method as a pseudopotential, as it retains the information of the correct behaviour of the wavefunction $\psi(\boldsymbol{r})$ that describes the core electrons and generates the pseudopotentials. The projector augmented wave method is a general approximation that introduces a linear transformation between the pseudo wave functions and the real wave functions, where this is the KS wavefunction without approximations. Its origin comes from the ideas of Slater (88), where space is divided into two regions with different behaviours.

2.2.6 The PAW Method

We will then consider a region of the boundary, in which the wavefunction $\psi(\boldsymbol{r})$ presents a smooth behaviour and another region closer to the nucleus of atoms, where the function $\psi(\boldsymbol{r})$ presents a disturbing behaviour due to the strong attractive nuclear potential. What the PAW method does in practice is transform the function $\psi(\boldsymbol{r})$ into a smooth function close to the regions where it is disturbed, introducing an auxiliary wave function $\tilde{\psi}(\boldsymbol{r})$ in that region, to get the wave function $\psi(\boldsymbol{r})$ through it. We need to correctly describe the wave function that will help us so that we can get the functions compatible with reality. We will use the T operator, so that:

$$|\psi_i(\boldsymbol{r})\rangle = T|\tilde{\psi}_i(\boldsymbol{r})\rangle, \tag{2.70}$$

where ψ_i is the real wavefunction and $\tilde{\psi}_i$ is the smooth wavefunction. The operator T will be given by:

$$T = 1 + \sum_R \hat{S}_R, \tag{2.71}$$

where S_R is a locality term applied to the atomic enclosure region of radius R. The operator T is composed of a part perfectly described by plane waves, in addition to a local term. We now need to determine the form of the S_R operator to continue the problem. We know that T when applied to smooth functions that seek to describe orbitals of the core $|\Phi_i\rangle$, returns the orbitals of the core $|\tilde{\Phi}_i\rangle$, where i represents the set of quantum numbers. So:

$$|\Phi_i\rangle = T|\tilde{\Psi}_i\rangle, \tag{2.72}$$

$$|\Phi_i\rangle = (1 + S_R)|\tilde{\Psi}_i\rangle, \tag{2.73}$$

$$S_R|\tilde{\Psi}_i\rangle = |\Phi_i\rangle - |\tilde{\Psi}_i\rangle. \tag{2.74}$$

Since the transformation T must be linear, the coefficients must be linear functions of the wave function $|\tilde{\Phi}_i\rangle$ and another fixed function called the *projector operator* ($\langle\tilde{P}_i|$), which is null in the region outside the core, where:

$$\langle\tilde{P}_i|\tilde{\psi}_j\rangle = \delta_{ij}. \tag{2.75}$$

The equation (2.74) can be rewritten as:

$$S_R|\tilde{\Psi}_i\rangle = \sum_j (|\Phi_j\rangle - |\tilde{\Phi}_j\rangle)\langle\tilde{P}_i|\tilde{\Phi}_j\rangle, \tag{2.76}$$

and applying in the total wavefunction, we'll have:

$$|\psi_i\rangle = |\tilde{\psi_i}\rangle + \sum_j (|\Phi_j\rangle - |\tilde{\Phi}_j\rangle)\langle\tilde{P}_i|\tilde{\psi_j}\rangle. \tag{2.77}$$

The projector operator is responsible for correctly writing the local character of the wave function. Having the projectors, we can find a way to describe the operators, so that they can correctly represent the eigenvalues acting on smooth plane waves instead of the core potentials. We have to calculate the expected value of an operator $\hat{O}$, analogously to the change between the Schrödinger and Heisenberg representations, by the linear transformation T:

$$\langle\psi_i|\hat{O}|\psi_i\rangle = \langle\tilde{\Psi}_i|T^\dagger\hat{O}\,T|\tilde{\Psi}_i\rangle. \tag{2.78}$$

To facilitate the calculations, we use some approximations for the regime close to the core potential. We will consider that:

$$\sum |\tilde{\Phi}_j\rangle\langle\tilde{P}_j| = 1, \tag{2.79}$$

and then:

$$T = 1 + \sum_j (|\Phi_j\rangle - |\tilde{\Phi}_j\rangle)\langle\tilde{P}_i|, \tag{2.80}$$

$$T = 1 + \sum_j |\Phi_j\rangle\langle\tilde{P}_j| - \sum_j |\tilde{\Phi}_j\rangle\langle\tilde{P}_j|, \tag{2.81}$$

$$T = 1 + \sum_j |\Phi_j\rangle\langle\tilde{P}_j| - 1, \tag{2.82}$$

$$T = \sum_j |\Phi_j\rangle\langle\tilde{P}_j|. \tag{2.83}$$

The core orbitals must equal the smooth function outside the argument region, causing $|\Phi_j\rangle = |\tilde{\Phi}_j\rangle$, and so $T = 1$. Therefore, these conditions lead us to a configuration for the average value of a given operator, which will be given by:

$$\langle\tilde{\psi_i}|\hat{O}|\tilde{\psi_i}\rangle = \langle\tilde{\psi_i}|T^\dagger\hat{O}\,T|\tilde{\psi_i}|\rangle = \langle\tilde{\psi_i}|\hat{O}|\tilde{\psi_i}|\rangle + \sum_{j,k}\langle\tilde{\psi_i}|\tilde{P}_k\rangle(\langle\Phi_k|\hat{O}\Phi_j\rangle - \langle\tilde{\Phi}_k|\hat{O}|\tilde{\Phi}_j)\langle\hat{P}_j|\tilde{\psi_i}\rangle, \tag{2.84}$$

such:

$$\tilde{\hat{O}} = \hat{O} + \sum_{j,k}|\tilde{P}_k\rangle(\langle\Phi_k|\hat{O}\Phi_j\rangle - \langle\tilde{\Phi}_k|\hat{O}|\tilde{\Phi}_j)\langle\hat{P}_j|. \tag{2.85}$$

We can include one more term due to the presence of the core region (ψ^c), causing the expected value of the operator to be given by:

$$\langle\tilde{\psi_i}|T^\dagger\hat{O}\,T|\tilde{\psi_i}|\rangle = \langle\tilde{\psi_i}|\hat{O}|\tilde{\psi_i}|\rangle + \sum_{j,k}\langle\tilde{\psi_i}|\tilde{P}_k\rangle(\langle\Phi_k|\hat{O}\Phi_j\rangle - \langle\tilde{\Phi}_k|\hat{O}|\tilde{\Phi}_j)\langle\hat{P}_j|\tilde{\psi_i}\rangle + \langle\psi^c|\hat{O}|\psi^c\rangle. \tag{2.86}$$

2.2.7 Basis - Periodic Systems, Plane Waves and Cutoff Energy

The crystalline state is characterized by a spatial repetition of a basic structure that may contain one or more atoms bonded together (89, 90). This repetition can occur in any direction, allowing the infinite system to be reproduced in the desired direction(s). We call this "unit" of repetition as *unit cell* (91). The main advantage of using the unit cell in calculations is that we can consider the external potential as:

$$V(\boldsymbol{r}) = V(\boldsymbol{r} + \boldsymbol{R}), \tag{2.87}$$

where $\boldsymbol{R}$ is a lattice translation vector.

According to Bloch's theorem, the wave function of an electron in a periodic potential defined by (2.87) can be written as the product of a function of the same periodicity as the potential (92), as:

$$\psi_{\boldsymbol{k}}(\boldsymbol{r}) = e^{i\boldsymbol{k}.\boldsymbol{r}} u_{\boldsymbol{k}}. \tag{2.88}$$

By the theorem (2.88), we naturally introduce the idea of plane waves. The KS orbitals $\psi\boldsymbol{r}$ must be written as an expansion of a set of PW, so that they form a complete basis and reproduce the periodicity of the lattice, according to the equation (2.88), where the term $u_{\boldsymbol{k}}$ is responsible for describing the periodicity of the lattice, and k represents the wave number. Then, the expansion of $u_{\boldsymbol{k},j}$ in plane waves takes the following form:

$$u_{\boldsymbol{k},j}(\boldsymbol{r}) = \sum_{\boldsymbol{G}} C_{\boldsymbol{k},j}(\boldsymbol{G}) e^{i\boldsymbol{k}.\boldsymbol{r}} u_{\boldsymbol{G},\boldsymbol{r}}, \tag{2.89}$$

where $C_{\boldsymbol{k},j}(\boldsymbol{G})$ are the Fourier coefficients and the index j indicates the different eigenstates, and so:

$$\psi_{\boldsymbol{k}}(\boldsymbol{r}) = \sum_{\boldsymbol{G}} C_{\boldsymbol{k},j}(\boldsymbol{G}) e^{i(\boldsymbol{G}+\boldsymbol{k}).\boldsymbol{r}}. \tag{2.90}$$

The vectors of the reciprocal lattice are represented by $\boldsymbol{G}$, and now the sum of the KS orbitals is done in the moments' space.

Bloch's theorem implies that the wave function can be expanded on a plane wave basis, as mentioned earlier. So the $\boldsymbol{G}$ allowed vectors lead to a reciprocal lattice with infinite vectors that represent the wave function with infinite accuracy, which would lead to extremely long and unpracticable calculations. So we need to impose cutoff energy to constrain the sum. In practice, Fourier coefficients decrease as the term $|\boldsymbol{k} + \boldsymbol{G}|$ increases, which allows the expansion to be truncated to a finite number of terms. That is, the maximum value of the kinetic energy for an electron in the system will be the cutoff energy which is given by:

$$E_{cut} > \frac{\hbar^2}{2m} |\boldsymbol{G} + \boldsymbol{k}|^2. \tag{2.91}$$

For historical reasons, it is common to express the cutoff energy, not in atomic units (a.u.), but in Rydberg (Ry), where 1 Ry = 13.6 eV = 0.5 $a.u.$ = 0.5 Hartree.

When expanding the KS equations into plane waves, we find a term for kinetic energy and a second term for potential energy, which leads us to find the energy eigenvalues. We provide the cutoff energy in the calculation to obtain the expansion coefficients of the KS orbitals, and thus the electron density $\rho(\boldsymbol{r})$.

Part I

Boron Based 2D Materials

3 Borophene: Pristine Phases and Superlattices

3.1 Electronic and Structural Properties in Pristine Borophene

In part I, our analysis is over borophene structures in two different cases: in the first moment, only pristine sheets, *viz.* S0, S1 e S2, where we investigate the electronic and structural properties combining DFT[1] and XANES[2]. Afterwards, we looked for borophene heterostructures combining pristine phases with different periodicities (44, 45), where we studied electronic properties, the rising of electronic stripes and transport properties in this borophene superlattices (BSLs). These BSLs were designed through lateral attaching of borophene pristine phases, changing the density of hollow hexagons, η, consequently modifying electronic and structural structures. Due to the higher stability of pristine S1 and S2 over S0, S1/S2 BSLs showed higher stability compared to those that contain S0 in their composition (29). In S1/S2, we find a highly anisotropic electronic structure that leads the lattices presents an electronic confinement ruled by pristine phase concentration (45).

Now looking for the adsorption of organic molecules over borophene sheets, our goal is to investigate the formation of self-organized molecular arrays, like of organic molecules such as tetracyanoquinodimethane (TCNQ) and tetrafluoro-tetracyanoquinodimethane (F4-TCNQ). Guided by the structure of the substrate, in this case, both pristine phases and borophene heterostructures will allow the formation of different molecular channels. If a stable molecular self-array is found, it will be possible to investigate the electronic properties as a function of an external field.

3.1.1 Electronic Properties

The Fig. [9(a1, b1 and c1)] presents our calculated electronic bands and structural models (a2, b2 and c2) of pristine borophene in S0 [Figs. 9(a1) and (a2)], S1 [Figs. 9(b1) and (b2)], and S2 [Figs. 9(c1) and (c2)] phases. In the S0 phase, the boron atoms are six-fold coordinated and present a buckled geometry. This buckling leads to two sublayers with a vertical distance (in our case, z direction) of 0.87 Å, in good agreement with the literature. As we briefly mentioned in section 1.1, the electronic band structure of S0 is highly anisotropic. This means that the band structure presents different features for different wave vectors, i.e., in the $\hat{y}$ direction (ΓY and SX K-paths), the S0 borophene looks like an insulator meanwhile in the $\hat{x}$ direction presents a metalic character - the

---

[1] See Chapter 2

[2] See Appendix D

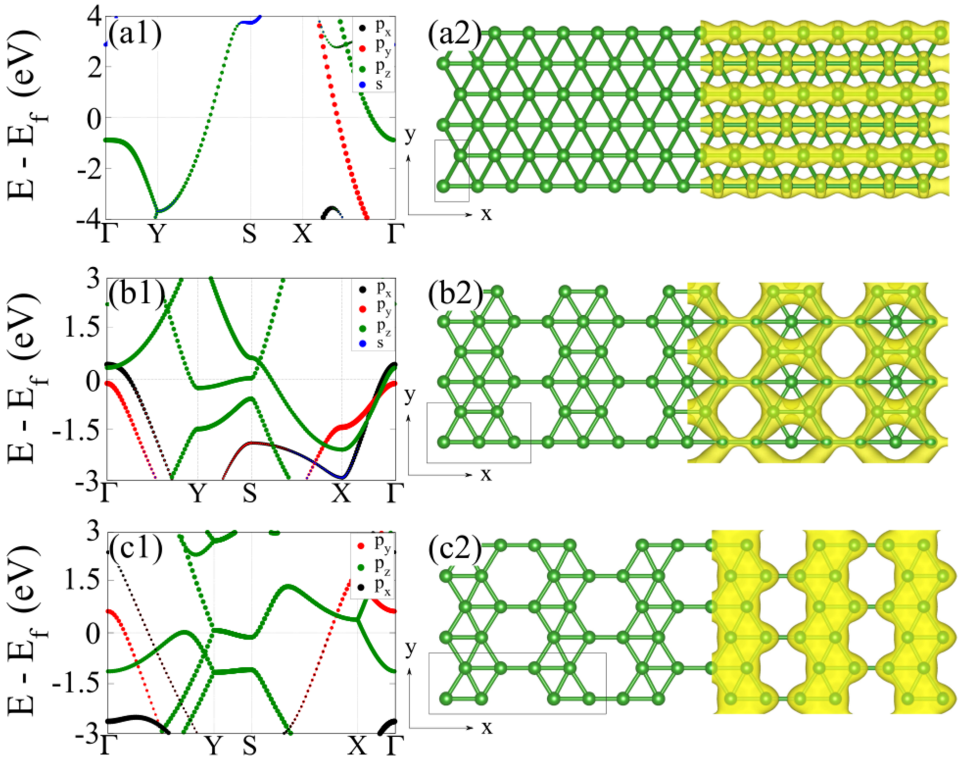

Figure 9 – Electronic structure, and structural models of the pristine borophene sheets with different vacancy concentrations (η), (a) S0 ($\eta = 0$), (b) S1 ($\eta = 1/6$), and (c) S2 ($\eta = 1/5$); and the projected density of states near the Fermi level, $E_F \pm 0.1\,\text{eV}$. The isosurfaces in (a2) and (b2) are equal to $2.5\,me/\text{Å}^3$, and in (c2) $5\,me/\text{Å}^3$.

Fig. [9(a2)] corroborates this feature, since there is a formation of metallic chanes only in the $\hat{x}$ direction. The electronic band structure of the Fig. [9(a1)] is characterized by the formation of p$_y$ and p$_z$ metallic bands for wave vectors along the Γ-X and Y-S directions, represented by red and green circles in [Fig. 9(a1)](6). Fig. [9(a2)] presents the projected electronic density of states near the Fermi level in an energy range of $E_F \pm 0.1\,\text{eV}$, where it can be verified the wave function overlap along the x-direction. For S0 phase, we verified that the electronic transport properties in S0 are characterized by a strong directional dependence (93). In S1 and S2 phases, the existing vacancies give place to a planar sheet (7). The planar boron sheets, with four-fold, five-fold and six-fold coordinated B atoms in S1 and five-fold and six-fold coordinated B atoms in S2, are characterized by a η density of hollow hexagons of 1/6 and 1/5, respectively. The energetic stability of those pristine systems was verified through calculations of the cohesive energy (E^c), which was given by:

$$E^c = \frac{E^{\text{sis}}}{N} - E_{\text{isol}}, \tag{3.1}$$

where E^{sis} is the total amount energy of system, N is the number of borophene atoms and E_{isol} is the energy of an isolated boron atom. Here we found E^c of -6.21, -6.25, and -6.27 eV/atom for S0, S1 and S2 phases, respectively, confirming that S2 is the most stable phase. Negative values of E^C are due to the system being stable. The energetic preference of S1 and S2, compared with S0 is in agreement with the previous first-principles results (27, 6, 7).

The metallic character of borophene in the S1 and S2 phases has been kept, as shown in band structures in Figs. [9(b1) and (c1)], indicated by the semi-filled bands that cross the Fermi level. However, compared with the S0, the electronic anisotropy (where metallic bands only exist in YS and XΓ K-paths), is somewhat dimmed, as in all K-paths have semi-filled energy bands. We find that the metallic bands of S1 are mostly composed of the B-2p_z and B-2p_x orbitals localized on the four-fold and five-fold coordinated B atoms. In S2 the formation of the metallic bands along the Γ-Y and S-X directions is dictated by a combination of σ- (B-2p_y) and π-orbitals (B-2p_z).

3.1.2 Structural Properties

To get some insight into the structural and electronic features of the borophene sheets, we simulate the boron K-edge XANES. We investigated the main features associated with the B-1s $\rightarrow \pi^*$ transitions by considering the polarization vector perpendicular to the borophene sheet ($\hat{\varepsilon}_{\perp}$). Structurally, there is a considerable difference between the three phases described. Boron atoms in S0, S1 and S2 are characterized by different geometries and coordination. In S0 we have only six-fold coordinated boron atoms. In S1, we have three types of coordination: (i) four-fold, (ii) five-fold and (iii) six-fold coordination; and in S2 only two types of coordination: (i) four-fold and (iii) five-fold coordination. The first one presents a buckled geometry, giving rise to boron lines along the x-direction [Fig. 9(a2)], while S1 and S2, due to the presence of vacancies, show a planar geometry, where the six-fold boron atoms are separated by boron vacancy lines, in S1 (Fig. [9(b2)]) and S2 these vacancies are formed by dimer stripes, also separated by boron vacancies.

Those structural differences can be identified at the near-edge absorption interval, as shown in Fig. [10(a1) and (a2)], where the comparison heads only with S0 and S1, then, between the six-fold coordinated B; namely, the B-1s, $\rightarrow \pi^*$ absorption peak in S0 presents a larger energy dispersion (wider Δ in Fig. [10(a1)]) in comparison with its counterpart in S1 (Fig. [10(a2)]). **This indicates that the presence of vacancy lines and the planar geometry of S1 results in more localized π^* states compared to the buckled S0 phase.** At the atomic scale, we have a nice manifestation of the role played by the local geometry on the absorption spectra. In S0 the B–B bond length (d) between B atoms lying on the same layer ($d = 1.61$ Å) is shorter than the ones of the six-fold coordinated boron atoms in S1 ($d = 1.71$ Å), and thus increasing the π^* hybridizations in S0 in comparison with S1.

Now showing S1 and S2, both are planar structures, with vacancies, and five-fold and four-fold coordinated boron atoms. S1 is characterized by hexagonal boron structures separated by vacancy lines, while in S2 we have zigzag rows of boron-dimers ($d = 1.67$ Å) separated by vacancy lines. As presented in Figs. [9(b2) and (c2)], the electronic density

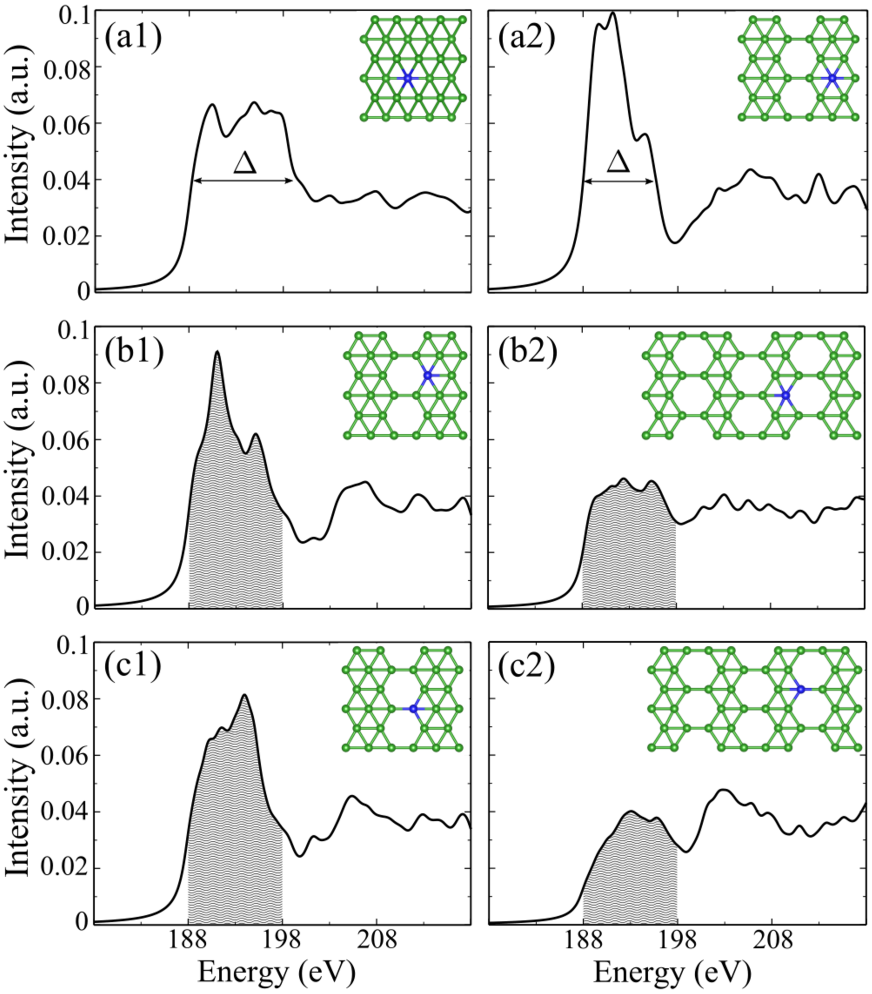

Figure 10 – The simulated X-ray Absorption Near-Edge Structure (XANES) of the pristine borophene sheets, K-edge spectra of six-fold boron atoms in S0 (a1) and S1 (a2); five-fold coordinated boron atoms in S1 (b1) and S2 (b2); four-fold coordinated boron atoms in S1 (c1) and S2 (c2). Inset, the local geometry of the probed boron atoms (blue circles).

of states of S1 and S2, near the Fermi level, shows different features. The hybridization in S1 somewhat mimics the one present in graphene, while in S2 there is charge density overlap along the zigzag rows of B dimers. Our simulated XANES results capture those structural and electronic differences. **In S1, the near edge spectra (shaded regions in Fig. [10(b1) and (c1)]) are characterized by a more intense and less dispersive B-1s $\rightarrow$ π^* transitions when compared with the ones in S2, (shaded regions in Figs. [10(b2) and (c2)]). This indicates that the presence of hexagonal structures in S1 gives rise to a more localized character of the π^*-orbitals near the Fermi level, meanwhile in S2, the hexagonal structures give rise now to a less localized character of the π^*-orbitals near the Fermi level.**

3.2 Electronic Properties in Borophene Superlattices

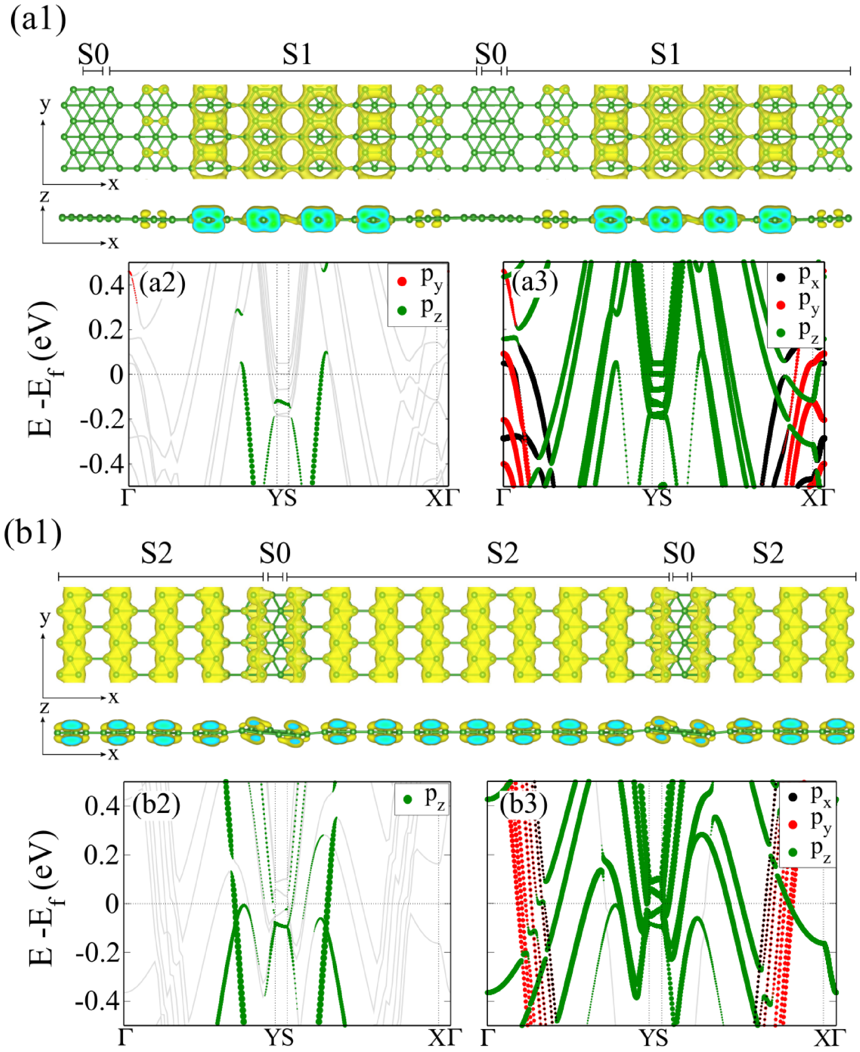

Figure 11 – Structural models (top-view and side-view) and the projected electronic density of states near the Fermi level, $E_{\mathrm{F}} \pm 0.1\,\mathrm{eV}$, of $\mathrm{S0_1/S1_7}$ (a1), and $\mathrm{S0_2/S2_4}$ (b1) BSLs. Electronic band structure of $\mathrm{S0_1/S1_7}$ [$\mathrm{S0_2/S2_4}$] projected on S0 (a2) [(b2)] and S1 (a3) [S2 (b3)] regions. Isosurfaces of $3\,\mathrm{m}e/\text{Å}^3$.

Motivated by the recent advances in the synthesis of 2D heterostructures and the theoretically proposed electronic localization upon the presence of defects in borophene (94), we examined the structural and electronic properties of borophene lateral heterostructures. Borophene heterostructures composed of S1 and S2 phases have been successfully synthesized, where the authors identified S1/S2 periodic assemblies with different relative concentrations (42). In this work, we have considered ordered 2D borophene superlattices (BSLs) combining different structural phases of borophene, with m/n periodicities, separated by zigzag edges. For instance, in $\mathrm{S0_1/S1_7}$ ($m = 1/n = 7$) we have one periodic unit cell of S0 separated by seven periodic unit cells of S1, as represented in Fig. 11(a1). In Ref. (44), electronic properties of some $\mathrm{S0}_m/\mathrm{S1}_n$ BSLs were intensively investigated.

Table 1 – Cohesive energies (E^c) of the BSLs (eV/atom) with different m/n periodicities, namely $\mathrm{S0_m/S1_n}$, $\mathrm{S0_m/S2_n}$, and $\mathrm{S1_m/S2_n}$.

		$\mathrm{S0_m/S1_n}$		
m/n	1/7	2/6	3/5	4/4
E^c	-6.26	-6.25	-6.25	-6.23
		$\mathrm{S0_m/S2_n}$		
m/n	2/4	2/2	4/1	8/1
E^c	-6.27	-6.27	-6.23	-6.23
		$\mathrm{S1_m/S2_m}$		
m/n	4/1	2/1	2/2	1/4
E^c	-6.26	-6.27	-6.27	-6.27
m/n	6/1	1/1	1/2	1/6
E^c	-6.26	-6.27	-6.27	-6.27

The equilibrium configuration of all BSLs was calculated taking into account the fully relaxed atomic positions and lattice vectors[3].

We will start our investigation looking for $S0_m/S1_n$ and $S0_m/S2_n$ BSLs, but taking a closer look at $S0_1/S1_7$ and $S0_2/S2_4$. After the relaxation, the bond lengths change drastically. For such a lower proportion of S0 in these BSL mentioned, the vertical buckling in S0 has been suppressed. In $S0_1/S1_7$ the B–B bond length between the B atoms lying on the same sublayer (taking pristine S0 as reference) increases from 1.61 Å to 1.83 Å at the inner sites of the S0 region, meanwhile for different sublayers, it reduces from 1.87 Å to 1.73 Å. Similarly in $S0_1/S2_4$ (Fig. [11(b1)]), where the vertical buckling at the inner sites of S0 reduces to 0.03 Å, with the bond length between the B atoms lying on the same sublayers reducting of 1.72 Å and 1.70 Å for different sublayers. The energetic stability of those BSLs was inferred by the calculation of the cohesive energies (E^c), where we found E^c of -6.26 eV/atom. Our results of E^c, summarized in Table 1, show that the cohesive energies of the other BSLs are practically the same when compared with the ones of the pristine phases, thus, supporting the energetic stability of those boron superlattices.

Examining the electronic properties of the aforementioned BSLs, we infer that in $S0_1/S1_7$ the electronic states near the Fermi level (in an energy range of $E_F \pm 0.1\,\mathrm{eV}$) are mainly localized on S1, giving rise to "electronic stripes" composed by graphene-like π-hybridizations along the four-fold and five-fold coordinated boron atoms, of the inner sites of $S1_{\mathbf{7}}$, separated by $S0_{\mathbf{1}}$ rows. The [Fig. 11(a1)] helps to clarify this inference - in the S1 region is possible to see the charge density overlap along the four- and five-fold coordinated from the inner sites of S1 fading into outer sites/S0 region. The localization of the electronic states can be also identified through the projection of the energy bands on S0 and S1, Fig. [11(a2) and (a3)], respectively; where it is noticeable that most of the metallic bands lying on S1. Such localization of the electronic states near the Fermi level and the electronic separation of the metallic bands have been also observed in $S0_2/S2_4$, Figs. [11(b)].

---

[3] A detailed description of computational details are presented in section F.1.

Here, the electronic states are predominantly localized along the S2 region. However, as shown in Fig. [11(b3)], in addition to the π-orbitals, we find that the σ-hybridizations also contribute to the formation of the metallic bands. The localization of the electronic states in the other $\mathrm{S0_m/S1_n}$ and $\mathrm{S0_m/S2_n}$ combinations, are presented in Figs. [13 and 14].

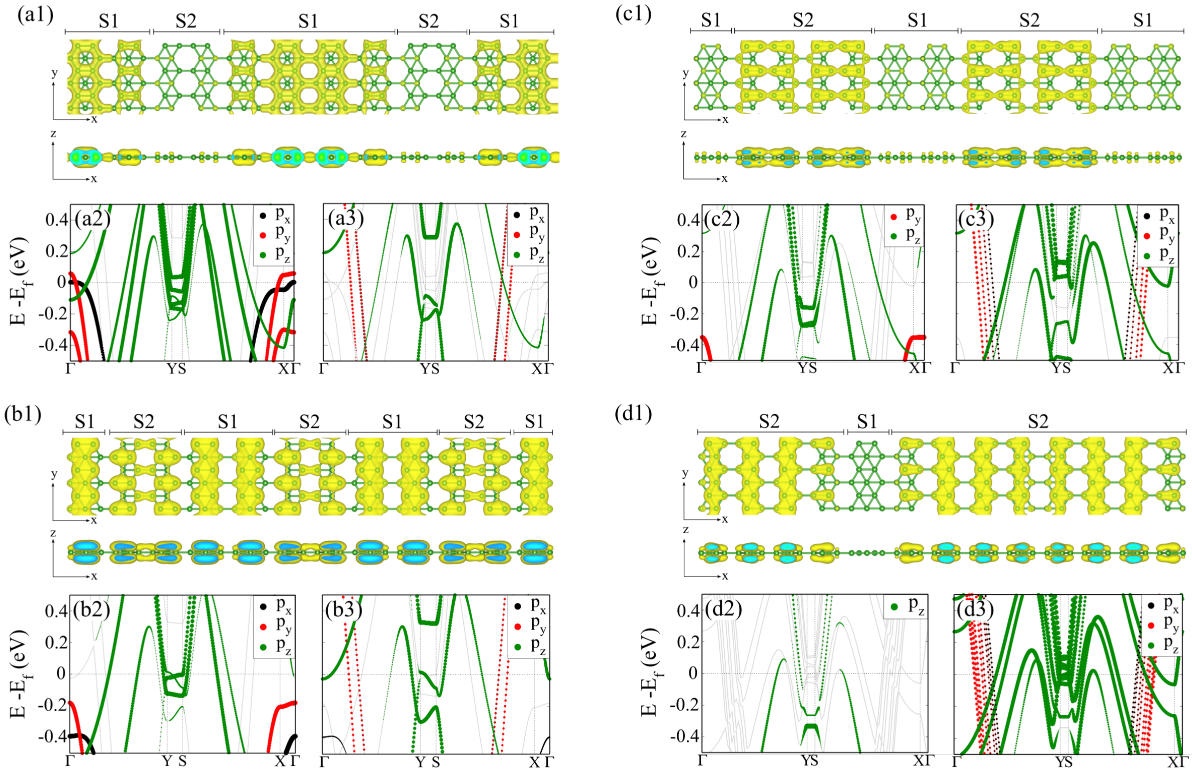

Figure 12 – Structural models (top-view and side-view) and the electronic density of states within $E_F \pm 0.1\,\mathrm{eV}$, of $\mathrm{S1_4/S2_1}$ (a1), $\mathrm{S1_2/S2_1}$ (b1), $\mathrm{S1_2/S2_2}$ (c1), and $\mathrm{S1_1/S2_4}$ (d1) BSLs. Electronic structure and the projection of the energy bands on $\mathrm{S1_4}$ (a2) and $\mathrm{S2_1}$ (a3); $\mathrm{S1_2}$ (b2) and $\mathrm{S2_1}$ (b3); $\mathrm{S1_2}$ (c2) and $\mathrm{S2_2}$ (c3); $\mathrm{S1_1}$ (c2) and $\mathrm{S2_4}$ (c3). Isosurfaces of $3\,\mathrm{m}e/\text{Å}^3$ in (a) and (d); and $1.5\,\mathrm{m}e/\text{Å}^3$ in (b) and (c).

A large number of possible structural combinations to build up heterostructures, based on borophene, is an interesting degree of freedom to control/design the electronic properties in 2D systems. Here we will examine the $\mathrm{S1_m/S2_n}$ BSLs, with m/n of 4/1, 2/1, 2/2, and 1/4, depicted in Fig. 12.

At the equilibrium geometry, (i) the planar structure has been preserved, and (ii) the S1/S2 zigzag interface boron atoms are neatly arranged, where the B–B bond lengths and angles are practically the same compared with the ones the pristine structures. At the equilibrium geometry, the bond lengths and angles at the interface region change by less than 0.8% and 1.5%, respectively, compared with the ones of the pristine S1 and S2 phases. So, this indicates that S1/S2 interfaces present lower strain than S0/S1 and S0/S2.

In $\mathrm{S1_4/S2_1}$, the electronic states within $E_F \pm 0.1\,\mathrm{eV}$ are mostly confined in S1 ruled by S2, Fig. [12(a1)]. There is a charge density overlap along S1, giving rise to metallic bands for wave vectors parallel to the ΓY and SX directions, Fig. 12(a2) and (a3). Those metallic bands are predominantly composed of B-2p_z orbitals lying on the four-fold and five-fold coordinated boron atoms of S1. Meanwhile, the projection of the energy bands on S2 reveals contributions from B-2p_z and -2p_y orbitals to the formation of the metallic bands. On the other hand, the electronic states with wave vector perpendicular to the S1/S2 interface, namely ΓX and YS directions, are characterized by dispersionless energy bands localized mainly on S1. Localization of the electronic states on the other $\mathrm{S1_m/S2_n}$ BSLs, m/n = 6/1, 1/1, 1/2, and 1/6 are presented in Fig 15, where is possible confirm the formation of tuneable electronic stripes in S1/S2 BSLs.

Reducing the width of S1, $\mathrm{S1_4/S2_1 \rightarrow S1_2/S2_1}$, the distribution of the electronic density of states near the Fermi level, on S1 and S2, becomes almost equivalent. However, they present different features (Fig. [12(b1)]). The metallic bands are characterized by π-hybridization through S1, while in S2 we have both, *i.e.* π- and σ-hybridizations (B-2p_y), with a major contribution from the latter along the zigzag B-dimers lines. Keeping the width of S1, and increasing S2, $\mathrm{S1_2/S2_1 \rightarrow S1_2/S2_2}$, we find that the electronic states near the Fermi level become more localized on S2, mostly on the four-fold coordinated boron atoms, as shown in Fig. [12(c1)]. Indeed, the π-and σ-hybridizations along the S2 rows have been strengthened, giving rise to metallic bands along the ΓY and SX directions, concomitantly there is a reduction of the electronic contribution from S1. Finally, upon further reduction of S1 and increase of S2, $\mathrm{S1_2/S2_2 \rightarrow S1_1/S2_4}$ (Fig. [12(d)]), there is a noticeable change on the electronic distribution along S2, where the wave function overlap between the B-2p_y orbitals becomes more intense, strengthening the σ-hybridizations and the orbital localization along S2, characterized by zigzag rows of B-dimers. A notable fact is that the B-dimer bond length in $\mathrm{S2_4}$ (d = 1.67 Å) is the same compared with that of S2 pristine.

In Figs. [13(a1)-(c1)] we present the localization of the electronic states near the Fermi level, $E_\mathrm{F} \pm 0.1\,\mathrm{eV}$, of $\mathrm{S0_m/S1_m}$ for m/n = 2/6, 3/5, and 4/4. There is an increase in the vertical buckling along the BSL proportional to the area of the S0 region. However, the localization of the metallic bands along the S1 region (mostly due to the B-2p_z orbitals) has been kept [Figs. 13(a2)-(b2) and 13(a3)-(b3)], although somewhat dimmed by increasing the proportion of S0. Similarly, features have been found in $\mathrm{S0_2/S2_2}$, where the surface area of $\mathrm{S2_2}$ is larger in comparison with that of $\mathrm{S0_2}$. On the other hand, the localization of the electronic states on S0 increases by increasing its area, (see Fig. 14). In Fig. 15 we present the electronic band structure, and the projection of the electronic states near the Fermi level for the $\mathrm{S1_m/S2_m}$ BSLs, with m/n = 6/1, 1/1, 1/2, and 1/6, where it is noticeable the change on the localization of the electronic states near the Fermi level, namely from S1 in $\mathrm{S1_6/S2_1}$ (Fig. [15(a)]) to S2 in $\mathrm{S1_1/S2_6}$ (Fig. [15(d)]).

3.3 Conclusions

- We confirmed the metallic character of the pristine systems, through simulations of X-ray Absorption Near-Edge Structure (XANES) we unveil the connection between the electronic properties and the atomic arrangement of borophene S0, S1, and S2 phases;
- We report that each structural phase presents a particular K-edge X-ray absorption spectrum, and thus, well-defined XAS fingerprints;
- Electronic structure calculations reveal confinement effects, which lead to metallic electronic stripes embedded in BSLs and a strong directional dependence in transmission probability, giving rise to transport channels tuned by m/n proportion.

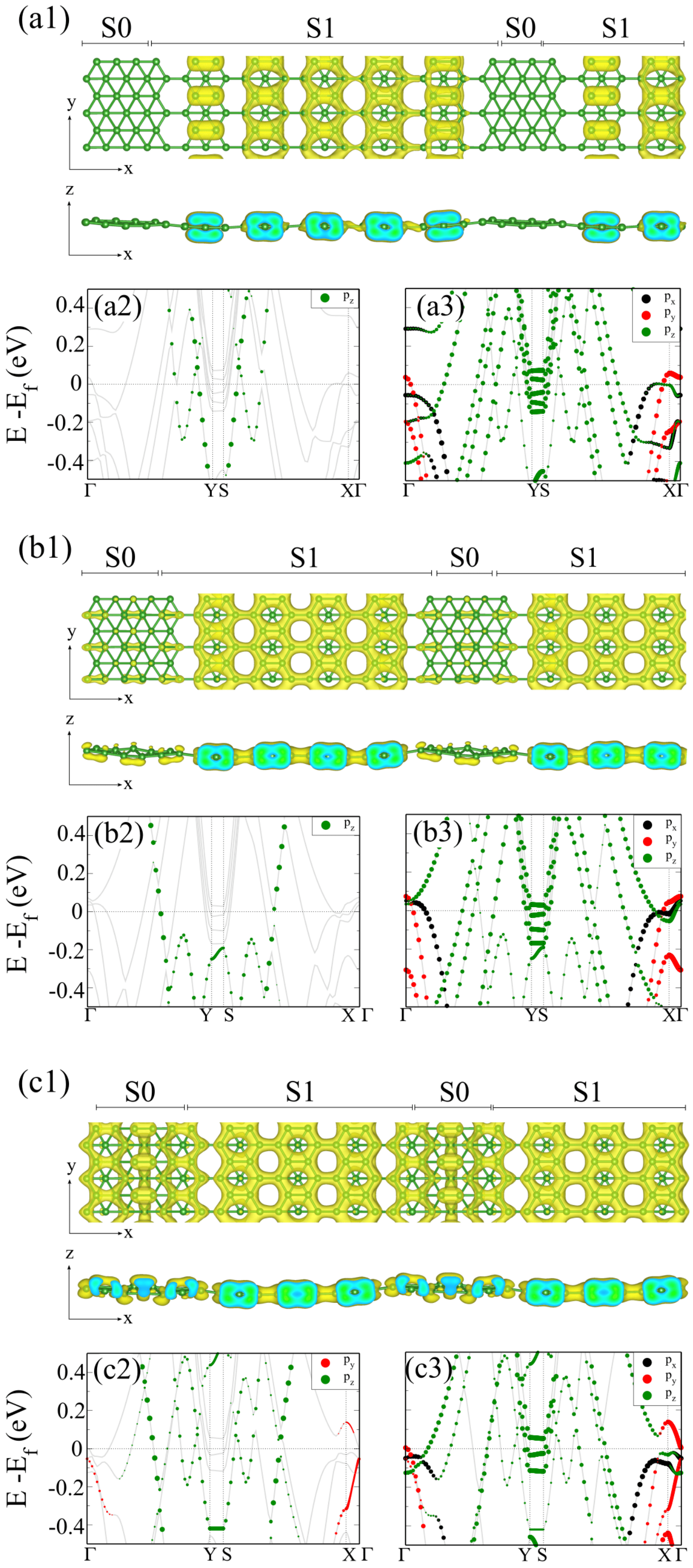

Figure 13 – Structural models (top-view and side-view) and the projected electronic density of states near the Fermi level, $E_F \pm 0.1\,\mathrm{eV}$, of $S0_2/S1_6$ (a1), $S0_3/S1_5$ (b1), and $S0_4/S1_4$ (c1) BSLs. Electronic band structure projected on the S0 [S1] regions (a2), (b2), and (c2) [(a3), (b3), and (c3)]. Isosurfaces of $3\,\mathrm{m}e/\text{Å}^3$ in (a); and $5\,\mathrm{m}e/\text{Å}^3$ in (b) and (c).

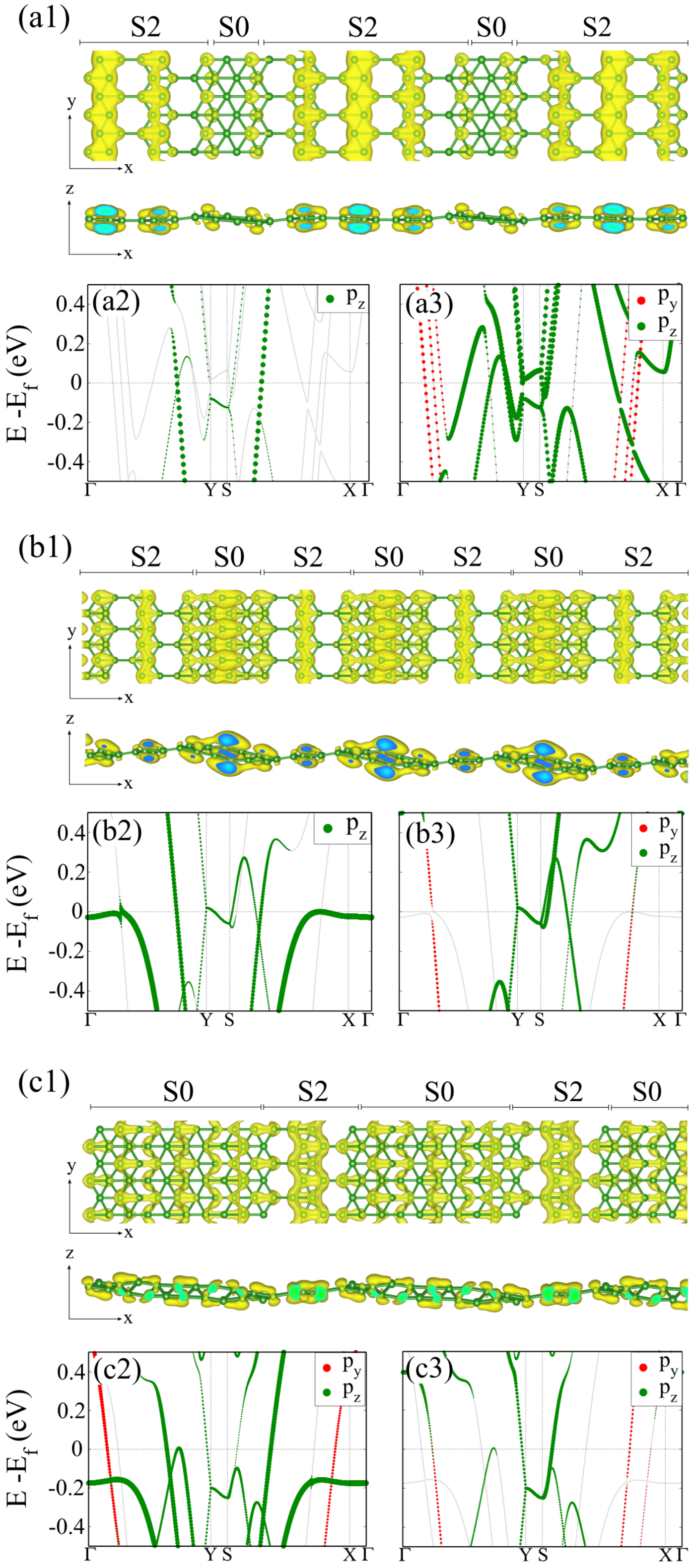

Figure 14 – Structural models (top-view and side-view) and the projected electronic density of states near the Fermi level, $E_F \pm 0.1$ eV, of $\mathrm{S0}_2/\mathrm{S2}_2$ (a1), $\mathrm{S0}_4/\mathrm{S2}_1$ (b1), and $\mathrm{S0}_8/\mathrm{S2}_1$ (c1) BSLs. Electronic band structure projected on the S0 [S2] regions (a2), (b2), and (c2) [(a3), (b3), and (c3)]. Isosurfaces of $3\,\mathrm{m}e/\text{Å}^3$ in (a) and (b); and $0.3\,\mathrm{m}e/\text{Å}^3$ in (c).

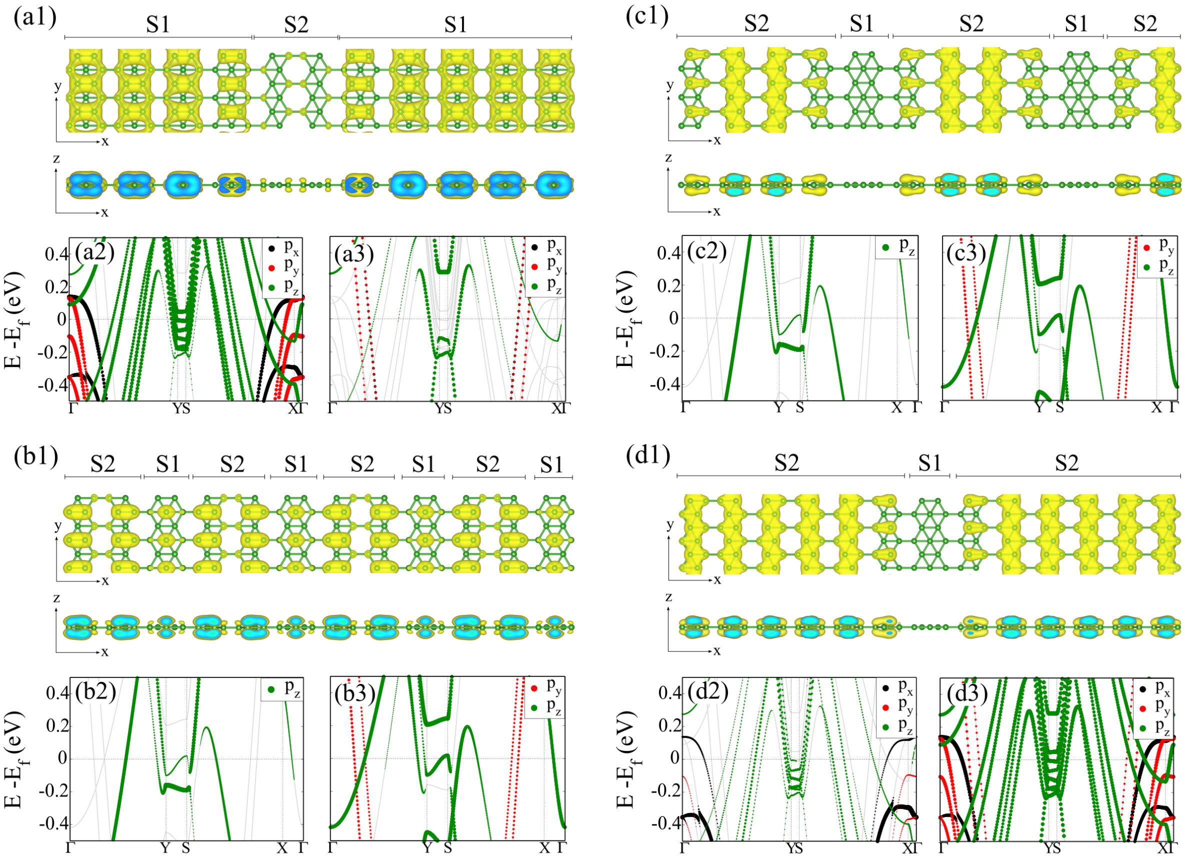

Figure 15 – Structural models (top-view and side-view) and the projected electronic density of states near the Fermi level, $E_F \pm 0.1\,\text{eV}$, of $\text{S1}_m/\text{S2}_n$ for m/n = 6/1 (a1), 1/1 (b1), 1/2 (c1), and 1/6 (d1). Electronic band structure projected on the S1 [S2] regions (a2), (b2), (c2), and (d2) [(a3), (b3), (c3), and (d3)]. Isosurfaces of $1.5\,\text{m}e/\text{Å}^3$ in (a) and (b); and $3\,\text{m}e/\text{Å}^3$ in (c) and (d).

4 Perspectives

4.1 Molecular Self-Assembly and Adsorption of Organic Molecules in Borophene Superlattices

In the last few years, carbon-based nanostructures have been intensively investigated. Following this tendency, boron-based was also included in this class. These materials could be used in nanodevices development and work as a support to investigate new phenomena in low-dimensional systems.

The molecular self-assembly process in solid surfaces is dictated mainly due to molecule-molecule and/or molecule-substrate interaction (95). The organic molecules adsorbed in graphene's surface were largely discussed in literature (96, 97, 98), and organic molecules that change substrate properties as tetracyanoquinodimethane (TCNQ) and tetrafluoro-tetracyanoquinodimethane (F4-TCNQ) are well-known for being a graphene electron-receiver (99). Here, our goal is to study the stability of these two molecules in borophene substrates, and the possibility of molecular self-assembly.

4.1.1 Pristine Borophene and Organic Molecules

To understand the interaction between borophene superlattices and organic molecules, firstly we started our investigation with pristine borophene, *viz.*: S1 and S2, interacting with TCNQ and F4-TCNQ.

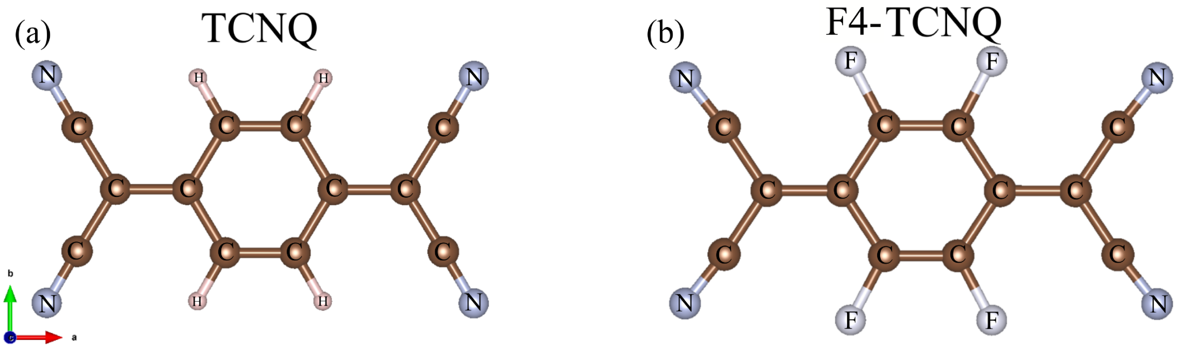

Figure 16 – TCNQ (a) and F4-TCNQ (b) molecules.

The isolated molecules' energetic stability was analysed through adsorption energy (E_{ads}), given by:

$$E_{\text{ads}} = E_{\text{sis}} - E_{\text{subs}} - E_{\text{mol}}, \tag{4.1}$$

where E_{sis} is the total amount of system energy, E_{subs} is the amount of energy of substrate and E_{mol} is the isolated molecule energy. Negative values indicate that the system was formed. Firstly were analysed a few specific sites for S1 as substrate, are detailed in figure [17]. These sites are namely bridge-x (BX), bridge-y (BY), hollow-x (HX), hollow-y (HY), top-x (TX) and top-y (TY). Bridge, hollow and top allude to graphene sites meanwhile the index x and y are about the molecule orientation. Adsorption energies are listed in table 2

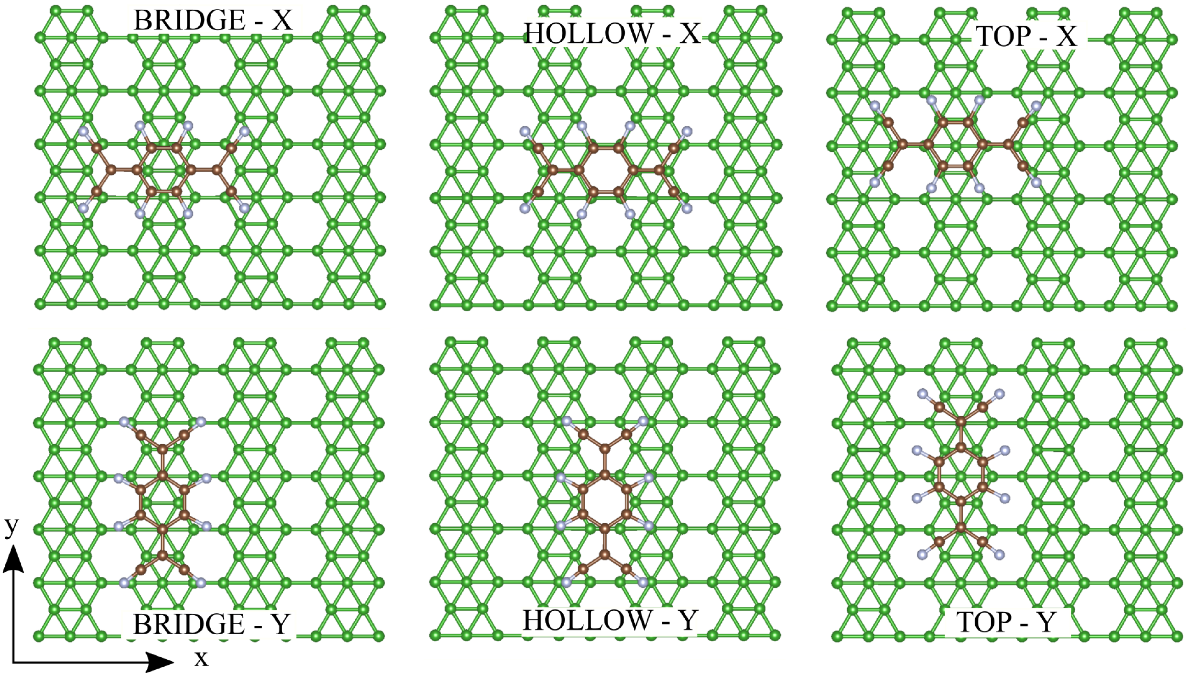

Figure 17 – TCNQ and F4-TCNQ adsorption sites in S1 borophene.

Table 2 – S1-TCNQ and S2-TCNQ adsorption energies (E_{ADS} in eV).

			S1-TCNQ			
site	BX	BY	HX	HY	TX	TY
E_{ads}	-1.37	-1.28	-1.34	-1.31	-1.31	-1.31
			S2-TCNQ			
site	BX	BY	HX	HY	TX	TY
E_{ads}	-1.40	-1.41	-1.41	-1.38	-1.38	-1.39

Calculations indicate that bridge-x is the most stable site for both molecules, with E_{ads} = -1.36 (-1.41) eV for TCNQ-S1 (TCNQ-S2). The next step is to analyse the most stable sites for S2 as substrate and BSLs from chapter 3, due to the electronic confinement effects in the latter, since there is a preference for phases ruled by the m/n proportion. If this fact is confirmed, we will verify (or not) the occurrence of molecular self-assembly and its electronic properties.

Part II

Carbon Based 2D Materials

5 Pristine and Oxidized Cellulose

In this chapter, we investigate cellulose disassembly after the TEMPO-oxidation process and how carboxylate groups influence the intersheet (IS) and interchain (IC) interactions along the inner sites of cellulose nanofibers (CNF). First, we present the total energy of the IS and IC interactions along the (i) pristine, detailed in subsection 5.2 and (ii) oxidized cellulose nanofibers (subsection 5.3). In (i), the main goal is to compare the IS and IC binding energies by using different approaches to describe the long-range van der Waals (vdW) interactions, herein vdW-DF (100, 101, 102, 103), vdW-DF2 (78) and optB86b, and in (ii) we once again investigate IS and IC interactions, but this time, focused on its strength as a function of the degree of oxidation of the carboxylate groups. Through TEMPO-mediated oxidation, was experimentally observed that the formation of nanofibers occurs with widths corresponding to the ones of single and double cellulose polymer chains.

5.1 Experimental Overview of the Cellulose Nanofibers

The reports in this section are here to explain how was obtained the CNFs. Experimental results were obtained and explained in the Brazilian Nanotechnology National Laboratory of the Brazilian Center for Research in Energy and Materials (LNNano/CNPEM) by Dr Juliana S. Bernardes' group.

The oxidized CNFs were isolated from sugarcane bagasse pulp through TEMPO-mediated oxidation using high oxidant content, 25 and 50 mmol/g. This reaction converts C6 primary hydroxyls groups from cellulose to carboxylates (COO^-) Na^+, yielding gravimetrically normalized values of 1.10 and 1.40 mmol of COO^- per gram of cellulose, respectively, which correspond to ca 25% of oxidation. Electrostatic repulsion between highly charged cellulose microfibrils SC-25 and SC-50ζ-potentials ca -65 mV in water) together with osmotic effects promoted the disassembling of completely individualized CNF dispersed in water without the need for high-energy mechanical treatments. On the other hand, cellulose fibres with low carboxylate content (SC-5, 0.4 mmol per gram of cellulose) presented aggregated fibril bundles, as already observed for different types of biomass. The SC-25 and SC-50 nanofibers present average lengths in the range of 243-370 nm and an average width of 4 nm, which may correspond to elementary fibrils diameter, according to Ding and Himmel's model for maize biomass (104). The full details of this experimental section[1] is available in (105).

---

[1] All experimental investigation that support the theoretical results here presented (and vice versa) was performed in Brazilian Nanotechnology National Laboratory of Brazilian Center for Research in Energy and Materials (LNNANO/CNPEM), Campinas, São Paulo, by Dr J. S. Bernardes' group. Once again, we register our thanks.

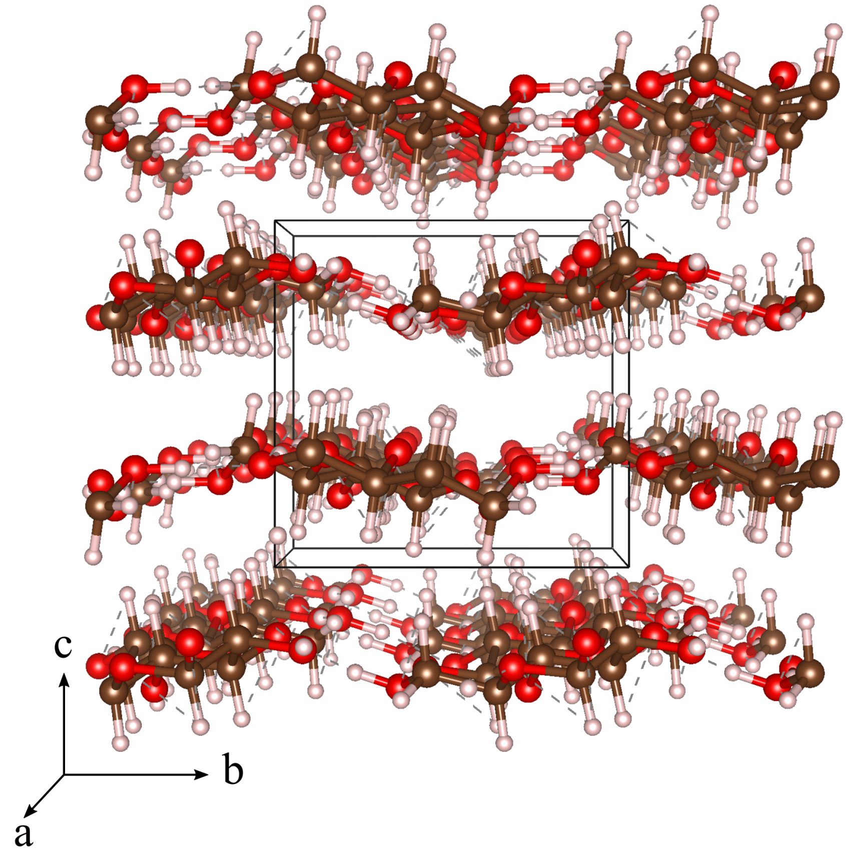

Figure 18 – Structural model of monoclinic cellulose I_β. Solid lines indicate a perspective view of the periodic unit cell.

5.2 Pristine Cellulose Nanofibers

The experimental results in (105) suggest that the formation of cellulose polymer chains is a consequence of the weakening of intersheet and interchain interactions within the elementary oxidized fibrils. To provide support to these results, DFT simulations are capable to unveil the noncovalent IS and IC interactions. The first step is to analyze hydrogen bonds and vdW forces and their behaviour in intersheet and interchain interactions

In Fig. 18 we present the structural model of the monoclinic I_β phase, where the periodic structure can be described by two misaligned molecular chains per unit cell. These sheets are composed of linear chains (**a** direction), where the lateral interchain interaction (**b** direction) is mostly ruled by O–H$\cdots$O hydrogen bonds (HBs), and them stacking (vdW interactions - direction **c**) is the responsible of the structural stability of this crystal. The strength of the intersheet (IS) and interchain (IC) interactions were quantified by the calculation of the IS and IC binding energies (E^b_{IS} and E^b_{IC}, respectively), given by:

$$E^b_{\text{IS}} = E_{\text{bulk}} - E_{\text{sheet}}, \tag{5.1}$$

$$E^b_{\text{IC}} = E_{\text{sheet}} - E_{\text{chain}}. \tag{5.2}$$

E_{bulk}, E_{sheet}, and E_{chain} corresponds to the total energies of crystalline cellulose nanofibers, free-standing cellulosic sheet, and free-standing single molecular chain. The binding energy

Table 3 – Interchain (IC) and Intersheet (IS) binding energies for different vdW.

vdW	E^b_{IS}	E^b_{IC}	E^b_{CNF}	$E^b_{\mathrm{IS}}/E^b_{\mathrm{IC}}$
DF	-1.351	-0.676	-2.027	2.0
D2	-1.080	-0.833	-1.913	1.3
no vdW	-0.127	-0.569	-0.697	0.2

Table 4 – Equilibrium geometry of I_β cellulose.

vdW	DF	D2	Exp. (46)
a (Å)	7.872	7.413	7.784
b (Å)	8.391	8.159	8.201
c (Å)	10.576	10.416	10.380
α (°)	90.0	89.8	–
β (°)	89.8	89.9	–
γ (°)	93.5	95.5	96.5

of the cellulose nanofibers (E^b_{CNF}) can be written as the sum of interchain and intersheet binding energies:

$$E^b_{\mathrm{CNF}} = E^b_{\mathrm{IC}} + E^b_{\mathrm{IS}}. \tag{5.3}$$

By using the vdW-DF approach, we have $E^b_{\mathrm{CNF}} = -2.027\,\mathrm{eV/unit\text{-}chain}$, where a unit-chain corresponds to two glucose rings. In order to investigate the role of energy cutoff, we increased it to 60 Ry, and we obtained $E^b_{\mathrm{IS}} = -1.321\,\mathrm{eV/unit\text{-}chain}$ and $E^b_{\mathrm{IC}} = -0.665\,\mathrm{eV/unit\text{-}chain}$, resulting in binding energy of $-1.986\,\mathrm{eV/unit\text{-}chain}$. As the energy differences are from a small order, our calculations were with 48 Ry. The total energy results are summarized in Table 3, where we have also considered the semi-empirical vdW-D2 approach, to describe the long-range dispersive interactions. In Table 4, we present some important information about the equilibrium geometry of the I_β crystalline cellulose. The results were in good agreement with the experimental measurements (46).

Despite several results in the literature, there is no consensus on which interaction would be more influential, i.e., with greater intensity in binding energy. Comparing our results, we find different results obtained through different calculation approaches. In the literature, Qian *et al.* (106) found IC interaction stronger than the IS interaction; while Parthasarathi *et al.* (107) obtained nearly the same contribution for both interactions. Meanwhile, even upon the inclusion of vdW correction (78), Li *et al.* (108) obtained 0.8 and 1.1 eV/unit-chain, for IS and IC interactions, respectively. In contrast, based on molecular dynamic (MD) simulations, Gross and Chu (109, 110) pointed out that the IS iteration is larger than the IC interaction. In our calculations, the total energy results are in agreement with these latter results. We found that the IS interaction is stronger than the IC one by almost twice, $E^b_{\mathrm{IS}}/E^b_{\mathrm{IC}} \approx 2$, using vdW-DF. By using the vdW-D2 approach, the strength of the IS interaction reduces, meanwhile in IC it increases, keeping E^b_{IS} larger than E^b_{IC} with a rate $E^b_{\mathrm{IS}}/E^b_{\mathrm{IC}}$ in ≈ 1.3. To check the accuracy of our results, we have calculated the binding energies using other nonlocal self-consistent vdW approaches. Technically they are the same approaches, but implemented in a different code - VASP in this case (see App. F). These results are summarized in Table 5.

Table 5 – Intersheet (IS), interchain (IC), and CNF binding energies using the vdW-DF, vdW-DF2, and vdW-optB86b approaches implemented in the VASP code. The binding energies are in eV/unit chain.

vdW	E^b_{IS}	E^b_{IC}	E^b_{CNF}	$E^b_{\text{IS}}/E^b_{\text{IC}}$
DF	-1.288	-0.663	-1.951	1.9
DF2	-1.232	-0.716	-1.948	1.7
optB86b	-1.441	-0.818	-2.259	1.8

In Refs. (109) and (110), the authors pointed out that vdW interaction rules the IS interaction, while it presents a minor contribution to the IC one. To provide a quantitative picture of the role played by the dispersive forces to the structural stability of the I_β CNFs, we calculate E^b_{IS} and E^b_{IC} by turning off the vdW contribution, but "freezing" the equilibrium geometry obtained by the vdW-DF calculation. Here, we found a reduction of the IS from -1.351 to -0.127 eV/unit-chain, while for the IC interactions change by less than 0.1 eV, $E^b_{\text{IC}} = -0.676 \rightarrow -0.569$ eV/unit-chain. The E^b ratio vdW/no-vdW in the first is ≈ 10.6 meanwhile in the latter is ≈ 1.2. **This evidences that vdW forces present (i) a dominant role in the energetic stability between the cellulosic sheets (about 90 % of the IS interactions), and (ii) a minor contribution to the IC interactions (∼16 %).** We will use this information [(i) and (ii)] to guide and provide an energetic picture of the disintegration of oxidized CNFs (section 5.3).

Here in this chapter, we didn't take into account any presence of solvents (explicit or implicit) or reorganization process in the calculations of the binding energies (111, 112, 113, 114). The E^b_{IC} and E^b_{IS} were obtained comparing the total energies, at T=0, of the initial (chain/sheet) and final (sheet/bulk) ground state configurations. We are assuming the approximation that (i) the solvent contribution to the total energies of the initial and final systems are nearly the same, as well as (ii) the temperature dependence carried out by the entropic term in the free energy. Therefore, within such an approximation, these contributions [(i) and (ii) separately] are cancelled out when we compare the initial and final free energies (115, 116).

5.3 Oxidized Cellulose Nanofibers

Now we will examine the changes of these IS and IC interactions upon the presence of charged carboxylate groups due oxidation process embedded within elementary fibrils. Here, we will show an atomistic picture of how these charged carboxylate groups rule the repulsive electrostatic forces within the nanofibrils, which in its turn weakens IS and IC interactions between the polymeric cellulose chains.

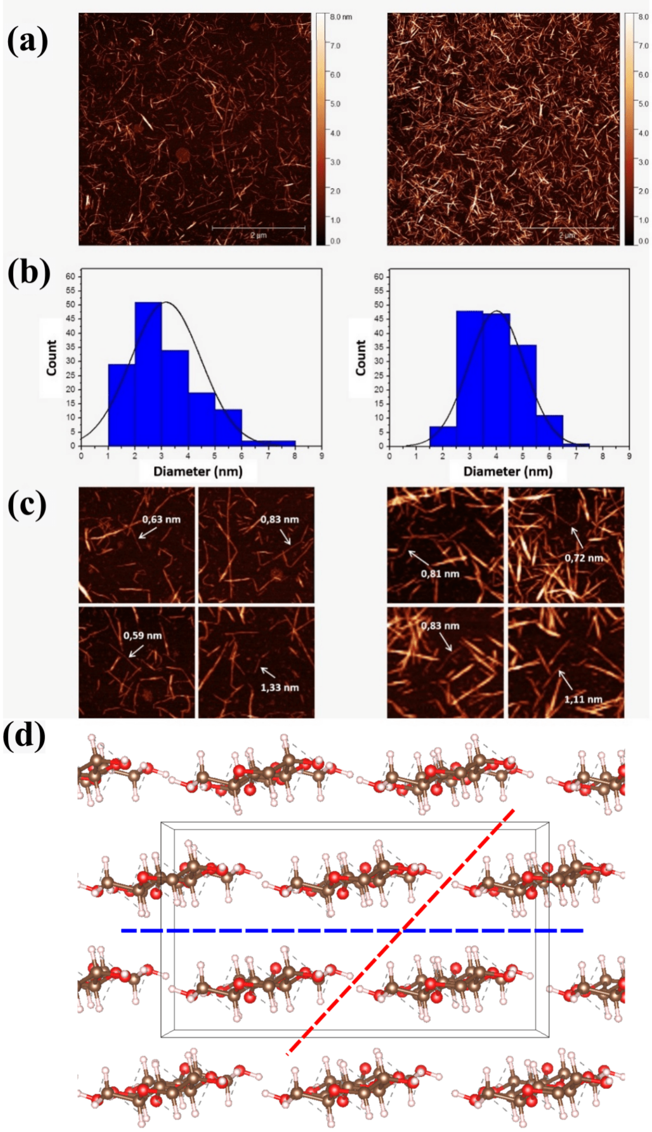

Figure 19 – AFM experimental images (a)/(c). In (b), elementary fibril diameter distribution in the oxidation process. IC and IS disruption, represented by red and blue dashed lines, respectively (d).

The energy cost to disintegrate the cellulose fibers reduces upon the formation of charged carboxylate groups (COO^-) (117). Indeed, previous experimental works have shown the disintegration of cellulose into nanofibers with diameters of 3-5 nm mediated by (TEMPO) oxidation processes (118, 119). Also, MD simulations have been done addressing the effect of the presence of carboxylate groups, bonded to the CNF surfaces, on the inter-fibril interaction (120). An important point here is that Pinto *et al.* (59) have used a recently proposed low-energy cost pathway to produce cellulose nanofibers with widths of single and double cellulose polymer chains (AFM images in Figs. [19(a) and (c)]).

Following this report, we expected that the formation of carboxylate groups should occur not only on the surface of the elementary fibrils but also at the inner sites of the CNFs (Fig. [19(b)] - indicated by the count of elementary fibrils with diameter < 3 nm)

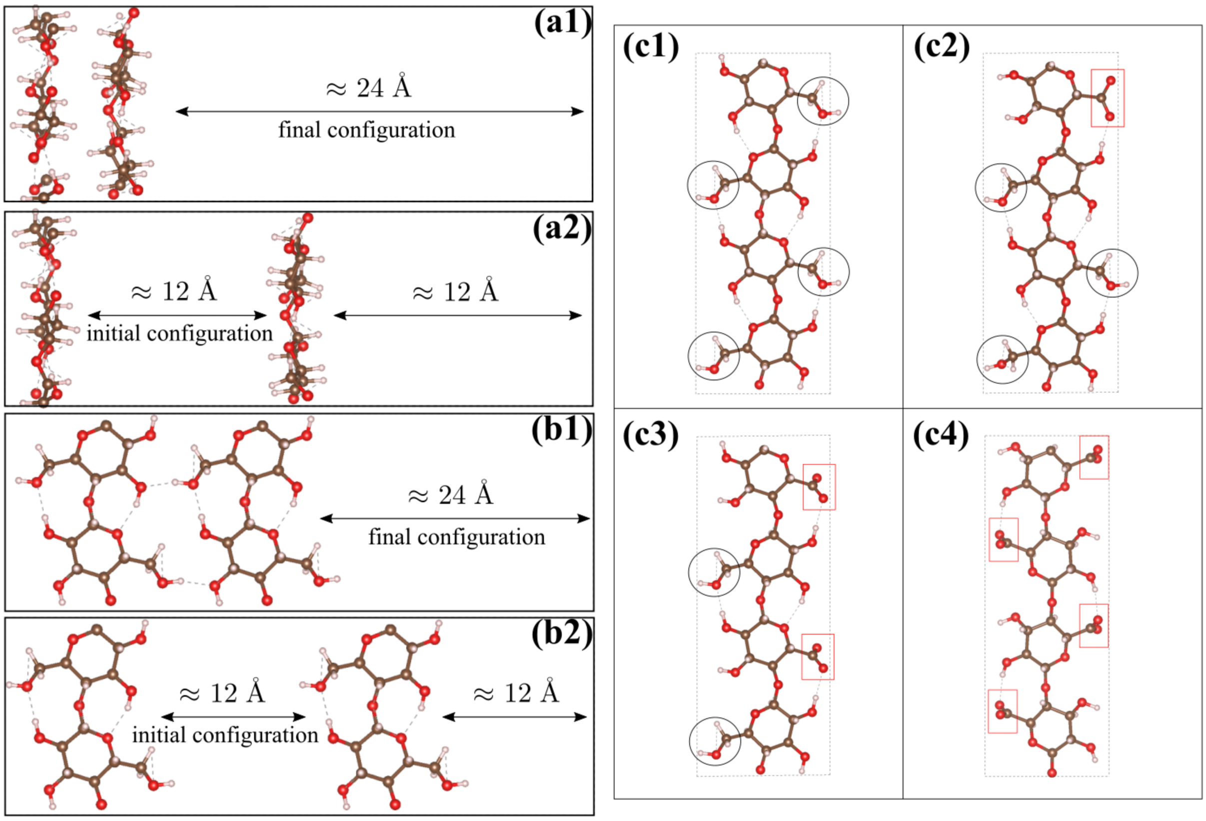

Figure 20 – Schematic representation of the IS (a) and IC (b) binding energy calculations. (a1)-(b1)/(a2)-(b2) Final/Initial configuration of two free standing cellulosic sheets (a) and chains (b). (c) Structural models of pristine (non-oxidized) NC chain (c1), and oxidized chains with linear concentration of carboxylate groups of $[\mathrm{COO}^-] = 25\%$ (c2), 50% (c3), and 100% (c4). The carboxylate groups are within red rectangles.

indicated by dashed lines in Fig. [19(d)], such there is a weakening of IS and IC interactions.

Figs. [20(a) and (b)] indicate how the calculation procedure of IS and IC (respectively) binding energy was conducted, as a function of the charging state of the carboxylate group. Here, the binding energy (E^b) corresponding to the IS [IC] interaction was obtained by comparing the total energies of two free-standing cellulosic sheets [chains] interacting with each other (their final configuration), as shown in figures 20(a1) [20(b1)], and the ones far from each other (their initial configuration), figures 20(a2) [20(b2)], for a given charging state (q),

$$E^b_{\mathrm{IS/IC}}(q) = E_{\mathrm{final}}(q) - E_{\mathrm{initial}}(q). \tag{5.4}$$

For each configuration (initial/final), we obtained fully relaxed atomic positions and the total energies including the vdW interactions within the vdW-DF approach. Within our supercell approach, we have considered the presence of carboxylate groups with different concentrations ($[\mathrm{COO}^-]$), i.e., 0% (pristine case), 25%, 50% and 100%, shown in figures 20(c1)-(c4). The localization of the net charge (q) was determined by using the Löwdin orbital population (121), where we found that most of the charging lies on the carboxylate groups. In Figs. [21(a) and (b)], we present how the net charge density along

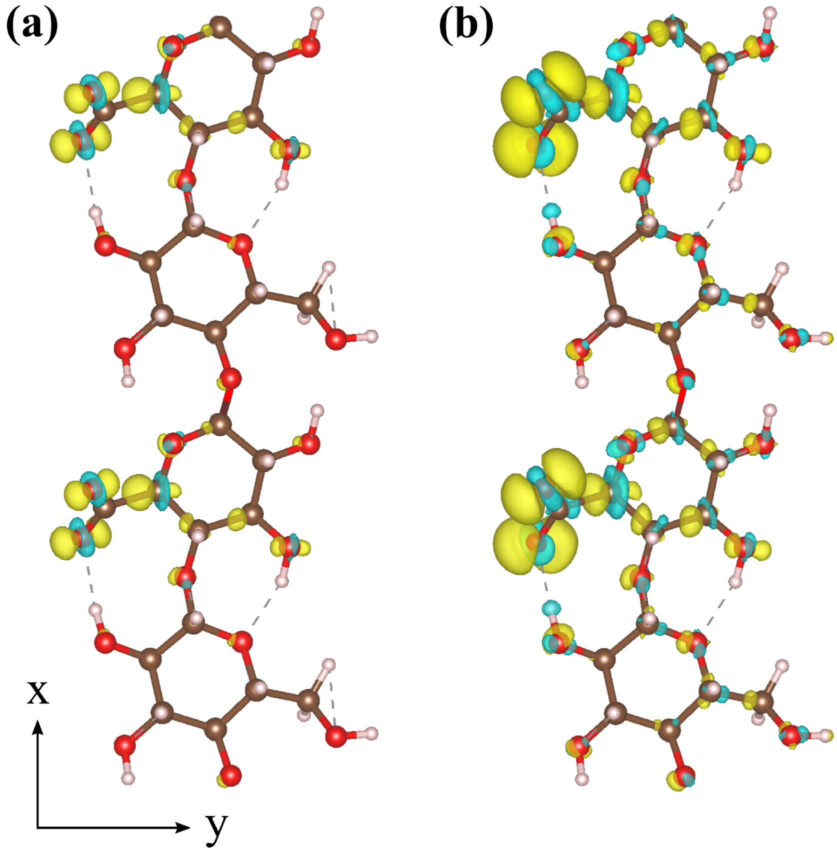

Figure 21 – Charge density distribution along oxidized cellulose chain, with [COO^-] of 50%, upon the net charging increase q=0.25 → 0.50 e (a) and q=0.25 → 1.0 e (b). Isosurfaces of 0.003 $e/\text{Å}^3$ in (a) and 0.002 $e/\text{Å}^3$ in (b).

a cellulose chain with [COO^-] of 50% increases when the charging state increases from q=0.25 → 0.50 e and q=0.50 → 1.00 e. To check the suitability of our calculation approach, instead of charging our supercell, we have considered the presence of sodium ions nearby the carboxylate groups (120). In this case, we found a net charging of about 0.5 e per [COO^-] unit.

Attempting for binding energies results for IS and IC interactions in figures 22(a) and (b), was revealed a weakening of the IS and IC interactions, compared with the ones of pristine systems (dashed lines in Fig. 22), that is proportional to the charging and the concentration of carboxylate groups. Moreover, the net (negative) charge localization in the carboxylate group, as shown in figure 21, actually supports the repulsive electrostatic role on the cellulose disassembling process of CNF by weakening the IS and IC interactions (117).

After binding energy comparison in figure 22(c), the higher E^b of interchain interaction shows that IC interactions are more sensitive to oxidation than the IS interactions. An example is given for [COO^-]=50% and charging of $q = 0.5e$, which IC binding energy reduces by 0.25 eV/unit-chain, $E^b_{IC} = -0.48 \rightarrow -0.23$ eV/unit-chain, whereas for the IS interaction, we found E^b_{IS} reduces only by 0.09 eV/unit-chain, $-0.60 \rightarrow -0.51$ eV/unit-chain. By these results, we suggest that the CNF disassembly should take place (preferentially) through a

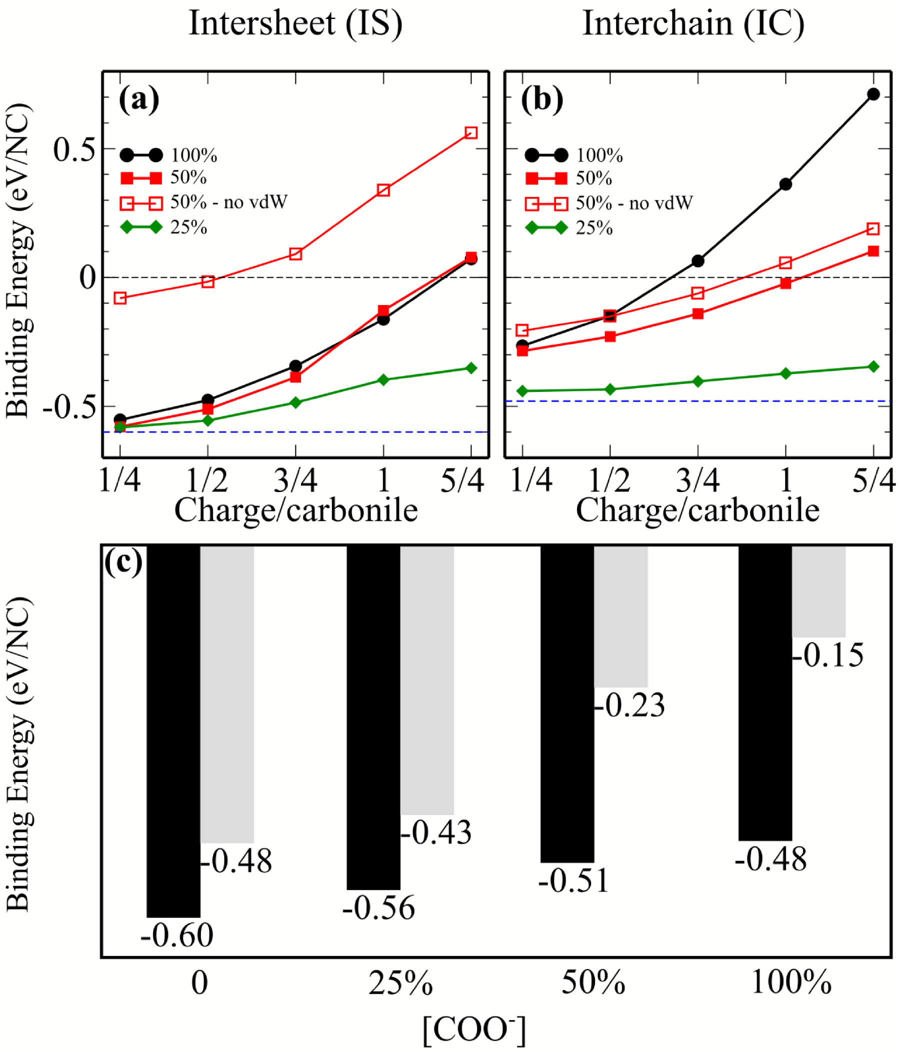

Figure 22 – Intersheet (a) and interchain (b) binding energy as a function of the charging state (q) with [COO$^-$]=100, 50, and 25%. Dashed lines indicate the calculated binding energies of a (non-oxidized) pristine system. (c) IS (black) and IC (shaded) binding energies for $q = 0.5e$. [COO$^-$] = 0 indicates non-oxidized pristine system.

disruption of the interchain interactions (indicated by red dashed lines in figure 19(d)])

In the pristine systems, the IS binding energy is mostly dictated by vdW forces, while the hydrogen-like C–H$\cdots$O bonds bring a minor contribution. Oppositely, IC binding strength is mostly ruled by hydrogen bonds, followed by a minor contribution from vdW forces.

Now, in oxidized systems, E^b_{IC} reveals a greater reduction when compared with E^b_{IS} [figure 22(c)]. To this, we can infer that the weakening of hydrogen bonds and vdW interactions (C–H$\cdots$O) play the main role in the disassembly process of CNFs. To provide qualitative support to such a statement, we calculate $E^b_{\mathrm{IS/IC}}(q)$, for [COO$^-$]=50%, with no vdW contribution to the total energies. The results for the IS and IC binding energies, indicated by empty squares in figures 22(a) and (b), show a significant reduction of IC binding energy. On occasion, for $q = 0.5\,e$, $E^{b}_{\mathrm{IS}}(q)$ reduces from -0.511 to $-0.016\,\mathrm{eV/unit\text{-}chain}$, while the intensity of the IC interaction reduces by about $0.08\,\mathrm{eV/unit\text{-}chain}$, $E^{b}_{\mathrm{IC}}(q) = -0.230 \rightarrow -0.151\,\mathrm{eV/unit\text{-}chain}$, i.e., the higher reduction of $\boldsymbol{E}^{\boldsymbol{b}}_{\mathrm{IS}}$ compared with that of $\boldsymbol{E}^{\boldsymbol{b}}_{\mathrm{IC}}$ is a consequence of the predominance of vdW forces in the IS interactions.

5.4 Conclusions

- A disruption of CNFs was attributed to the formation of carboxylate groups embedded within oxidized fibrils, weakening the noncovalent interchain (IC) and intersheet (IS) interactions;
- The disassembling process depends on the concentration of the carboxylate groups;
- IC and IS binding energies $[E^b_{IC/IS}(q)]$ reduce in the oxidized CNFs;
- A reduction of $E^b_{IC/IS}(q)$ is proportional to the charging state (q), and the concentration of the oxidized carboxylate groups indicating an electrostatic repulsion between the (charged) cellulose fibrils;
- The disassembly processes of the oxidized CNFs should take place primarily through a disruption of the interchain interactions, giving rise to (predominantly) fibers and cellulose chains, instead of sheets, as a final structure, and thus in accordance/supporting with the present experimental AFM observations.

6 Cellulose-Graphene Interaction

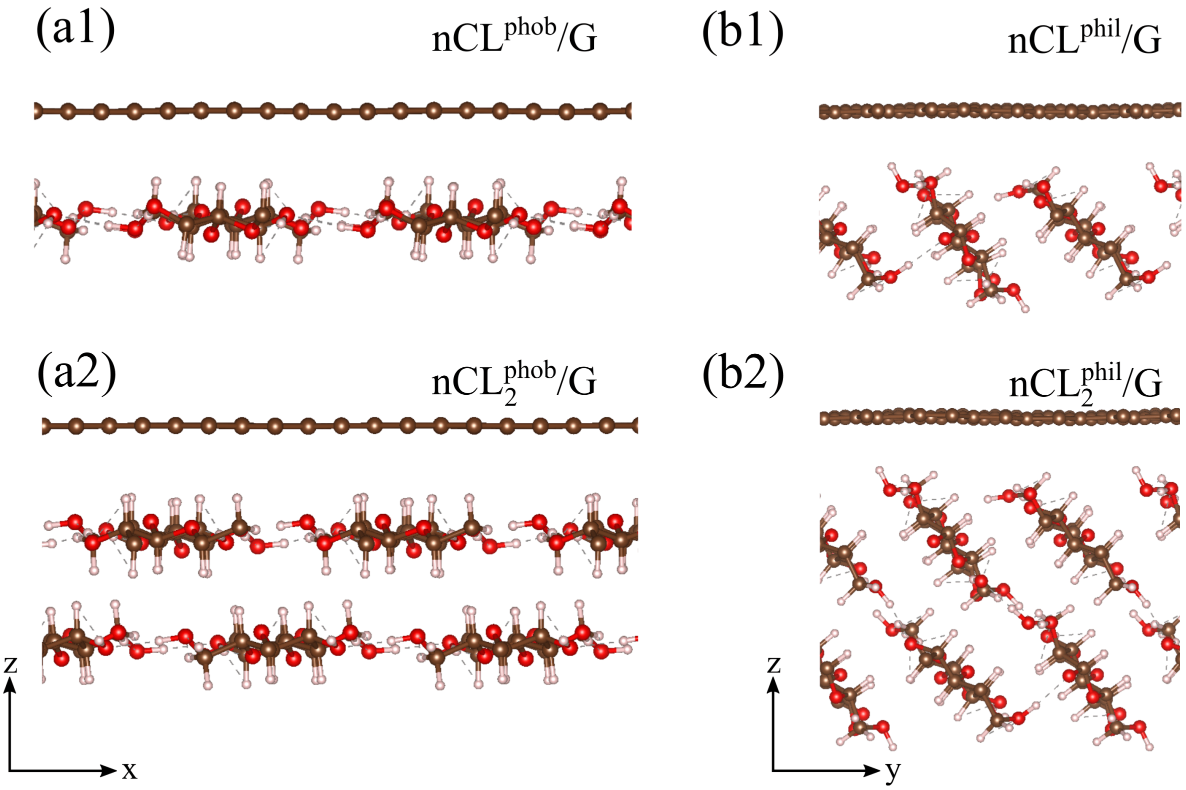

Figure 23 – Structural models of graphene interacting with the hydrophobic (a1)-(a2), and hydrophilic (b1)-(b2) nanocellulose sheet described by a single layer (a1)-(b1), and bilayer (a2)-(b2) of cellulose nanofibrils.

6.1 Nanocellulose - Graphene Binding Energy and Geometry

The first step in this chapter is to examine the energetic stability and equilibrium geometry of the nCL/G interface, and the role played by the long-range vdW forces on the nanocellulose - graphene binding strength. The structural models of nCL/G interface investigated in this work are shown in Fig. 23. The graphene layer interacts with two different cellulose interfaces: (i) hydrophobic (Figs. [23 (a1) and (a2)]) and (ii) hydrophilic (Figs. [23 (b1) and (b2)]) nanocellulose sheets described by a single layer of cellulose fibrils, labelled as nCL^{phob}/G and nCL^{phil}/G in figure 23(a1) and (b1), and bilayer of cellulose fibrils, nCL$_2^{phob}$/G and nCL$_2^{phil}$/G in figure 23(a2) and (b2).

The hydrophobic interface is characterized by the predominance of CH-π bonds[1], while in nCL^{phil}/G the interface interaction is mainly dictated by the OH-π bonds[2]. The nCL/G

---

[1] CH-π bonds are those bonds which a CH- radical (from cellulose) is bonded in a C from graphene

[2] OH-π bonds are those bonds which an OH-radical (from cellulose) is bonded in a C from graphene

Table 6 – Binding energies (E^b in meV/Å^2) and ncl–G interface distance (h in Å) of the nCL$^{\text{phob}}$/G and nCL$^{\text{phil}}$/G interfaces.

	nCL$^{\text{phob}}$/G		nCL$^{\text{phil}}$/G	
vdW	E^b	h	E^b	h
DF	12.92	2.71 ± 0.09	11.63	2.59 ± 0.12
optB86b	15.10	2.53 ± 0.08	13.87	2.13 ± 0.12
no vdW	0.51	3.04 ± 0.08	0.81	2.90 ± 0.23
DF-solvent	11.80	2.71 ± 0.09	9.51	2.70 ± 0.06
	nCL$_2^{\text{phob}}$/G		nCL$_2^{\text{phil}}$/G	
vdW	E^b	h	E^b	h
DF	13.22	2.75 ± 0.07	12.34	2.51 ± 0.13
optB86b	16.07	2.46 ± 0.07	13.91	2.32 ± 0.13
DF-solvent	12.92	2.74 ± 0.07	9.69	2.69 ± 0.10

interface binding energy (E^b) was calculated by:

$$E^b = E[nCL/G] - E[nCL] - E[G], \tag{6.1}$$

i.e., comparing the total energy of the final system (E[nCL/G]) and the sum to the total energies of the isolated components; for example, in Figs. 23 (a1) and (b1) a single sheet of cellulose nanofibrils (E[nCL]) and single layer graphene (E[G]). For each interface, nCL$^{\text{phob}}$/G and nCL$^{\text{phil}}$/G, we have considered three different stacking geometries, varying cellulose sheet position through graphene sites. Then was found that E^b and the average equilibrium vertical distance between the nCL and graphene sheet (h) changes by less than 0.06 meV/Å^2 and 0.01 Å.

The results of E^b and h, in Table 6, reveal an energetic preference for the nCL$^{\text{phob}}$/G interface. By using the vdW-DF approach to describe the long-range vdW interactions we found binding energies of 12.92 and 11.63 meV/Å^2 for nCL$^{\text{phob}}$/G and nCL$^{\text{phil}}$/G, respectively. To compare it with other layered 2D counterpart systems, we find that the nCL$^{\text{phob}}$/G binding energy is comparable with that of boron-nitride/G bilayer [∼12 meV/Å^2(122)], ∼ 40% smaller for that graphene bilayer, about 13% smaller compared with the inter-sheet binding energy of nCL (105), and between 16% and 40% higher when compared to graphene oxide (GO) and nCL$^{\text{phob}}$ interface, depending on the oxygen concentration (123). We have also calculated the binding energies by using the vdW-optB86b functional (the results are summarized in Table 6). Adding a second layer of cellulose nanofibrils, nCL$_2^{\text{phob}}$/G and nCL$_2^{\text{phil}}$/G, as depicted in Figs. 23(a2) and (b2), respectively, confirms the energetic preference for the nCL$^{\text{phob}}$/G interface, which is in good agreement with recent theoretical findings based on molecular dynamic simulations (124, 125). These previous studies indicate that the presence of trapped water molecules at the nCL/G interface reduces the binding energy; further, was verified the exclusion of the water molecules from the nCL$^{\text{phob}}$/G interface (124). To confirm this, we checked through the implicit solvation model[3] (126, 127) a reduction of the interface binding energy, leading to $E^b = 12.92 \rightarrow 11.80\,\mathrm{meV/Å^2}$ in nCL$^{\mathrm{phob}}$/G, and $11.63 \rightarrow 9.51\,\mathrm{meV/Å^2}$ in the nCL$^{\mathrm{phil}}$/G interface. The equilibrium geometries of the nCL/G interfaces showed tiny variation, almost remaining the same as those obtained previously with no solvent effects. These calculations took into account only electronic effects, ignoring any geometry effect (it is a direct consequence of the implicit solvation model). It is worth noting that the larger binding energy reduction in the latter is due to the hydrophilic nature of the interface, which is in agreement with the results of solvation energies E^s (also showed in Table 6), with E^s = 2.87 and $10.77\,\mathrm{meV/Å^2}$ in nCL$^{\mathrm{phob}}$/G and nCL$^{\mathrm{phil}}$/G, respectively, and 4.21 and 11.19 in the nanocellulose bilayer systems, nCL$_2^{\mathrm{phob}}$/G and nCL$_2^{\mathrm{phil}}$/G.

As discussed in the previous chapter, long-range vdW dispersion interaction plays an important role in the interchain and intersheet binding energy between the cellulose fibrils and nCL sheets, respectively. Here, once again, to measure the role played by the vdW interaction on the nCL - G binding energy, we have calculated E^b by turning off the vdW contribution. In this case, the binding energy of the nCL$^{\mathrm{phob}}$/G (nCL$^{\mathrm{phil}}$/G) interface reduces to 0.51 (0.81) $\mathrm{meV/Å^2}$, and the vertical distance $\boldsymbol{h}$ increase to 3.04 (2.90) Å; so, as occurred in intersheet binding energy in pristine nCL (105), we can deduce that the non-covalent (vdW) interactions once again rules the formation of nCL/G interfaces. Comparing the vdW role in the nCL/G interface with the one in graphene bilayer (GBL), where the interlayer interaction is mainly ruled by π–π bondings, within the vdW-DF approach, we found that the binding energy reduces from 21.16 to $0.51\,\mathrm{meV/Å^2}$, and the interlayer distance increases from 3.47 to 3.70 Å.

6.2 Structural Characterization

Core-level spectroscopy is a powerful tool to provide the structural characterization of materials on an atomic scale based on the local electronic properties of the probed element. The combination of experimental XANES data and first-principles simulations has proven to be a highly successful strategy to understand the atomic structure of novel materials (128, 129, 130, 131). In this section, we will show XANES simulation results of the Carbon K-edge absorption spectra of nCL/G interfaces to find spectroscopic fingerprints of the atomic structures of the nCL$^{\mathrm{phob}}$/G and nCL$^{\mathrm{phil}}$/G interfaces.

Our investigation starts with the XANES of the pristine isolated systems, graphene, and single layer nCL. In Fig. 24(a), we have the absorption spectra of graphene as a function of the orientation (θ) of the radiation polarization vector ($\hat{\epsilon}$), where we can identify the C-1$s \rightarrow \pi^*$ [$\rightarrow \sigma^*$] transition for $\hat{\epsilon} = \hat{\epsilon}_\perp$ ($\theta = 90°$) [$\hat{\epsilon} = \hat{\epsilon}_\parallel$ ($\theta = 0°$)]. The energy positions of these absorption peaks, around 285 and 292 eV, respectively, indicated as g_1 and g_2 in figure 24(a), and the dependence of their intensities with the orientation

---

[3] see Appendix E.

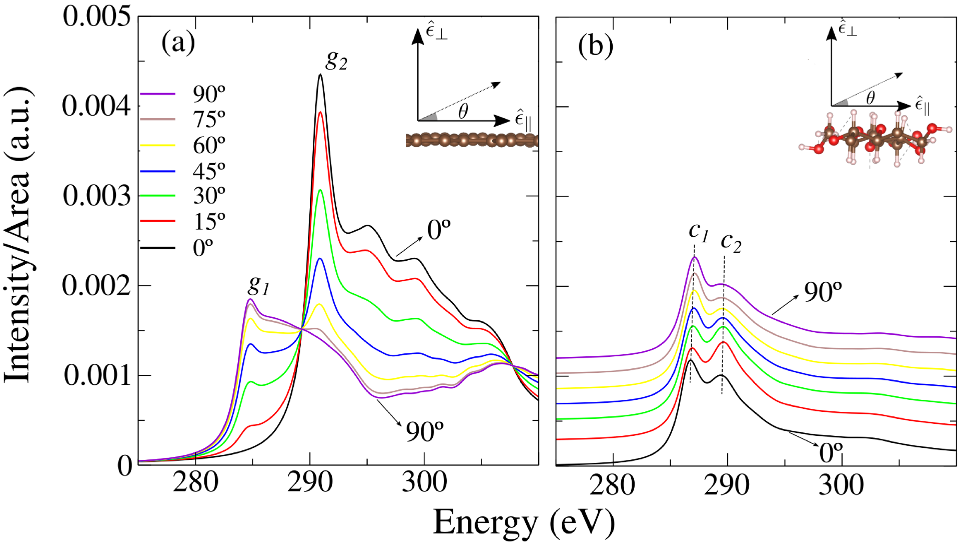

Figure 24 – Carbon K-edge simulated XANES spectra of pristine graphene (a), and single layer cellulose fibrils (b) as a function of the radiation polarization angle (θ).

of the polarization vector is in good agreement with the previous experimental findings (132, 133, 134). Experimental results of XANES spectra of cellulose (135, 136) indicate the presence of two absorption peaks, at 289.3 and 290.7 eV, both attributed to the C-1$s \rightarrow \pi^*$ transition, associated to the C–OH and C–H bonds, respectively. Those bonding structures are present in the single layer nCL, and the respective absorption spectra were identified in our simulations. In Fig. 24(b), we show our results for a single-layer nCL sheet which are characterized by (i) two absorption peaks, denoted c_1 and c_2, lying at about 287 and 290 eV, and (ii) reduced angular dependency with the direction of the polarization vector compared to the one of graphene (Fig. [24(a)]). As shown in Fig. 24(b), the energy positions of c_1 and c_2 changes by 0.36 and 0.21 eV, respectively, for $\theta = 0° \rightarrow 90°$. These simulations of the XANES spectra of nCL were performed by taking into account the polar angle [θ, presented in Figs. 24 and 25], and two azimuthal (ϕ) angles, one for polarization vectors parallel and another perpendicular to the cellulose fibrils.

The XANES spectra of nCL$^{\text{phob}}$/G and nCL$^{\text{phil}}$/G interfaces are shown in Figs. 25(a) and (b). In both spectra we identify the C-1$s \rightarrow \pi^*$ and $\rightarrow \sigma^*$ absorption features from graphene for $\theta = 90°$ and 0°, respectively. Between these two transitions energies, we can identify the following differences in the absorption features in nCL$^{\text{phob}}$/G and nCL$^{\text{phil}}$/G attributed to the nCL absorption spectra, (i) the presence absorption peaks *1a* and *2a* [Fig. 25(a)] for $\boldsymbol{\theta} = \mathbf{0°}$, while in the nCL$^{\text{phil}}$/G we find one absorption feature, *1b* in Fig. 25(b); (ii) the absorption peak *2b* at 287.5 eV is clearly visible in the nCL$^{\text{phil}}$/G interface for $\boldsymbol{\theta} = \mathbf{90°}$, but it is attenuated in nCL$^{\text{phob}}$/G; and (iii) due to the tilted geometry of cellulose fibrils with respect to the graphene layer, the absorption spectra in nCL$^{\text{phil}}$/G are no longer symmetric for positive and negative values of radiation polarization angles. For instance, the absorption features for $\theta = +15°$ and $-15°$ (dot-dashed lines) present different intensities, as seen in Fig. 25(b).

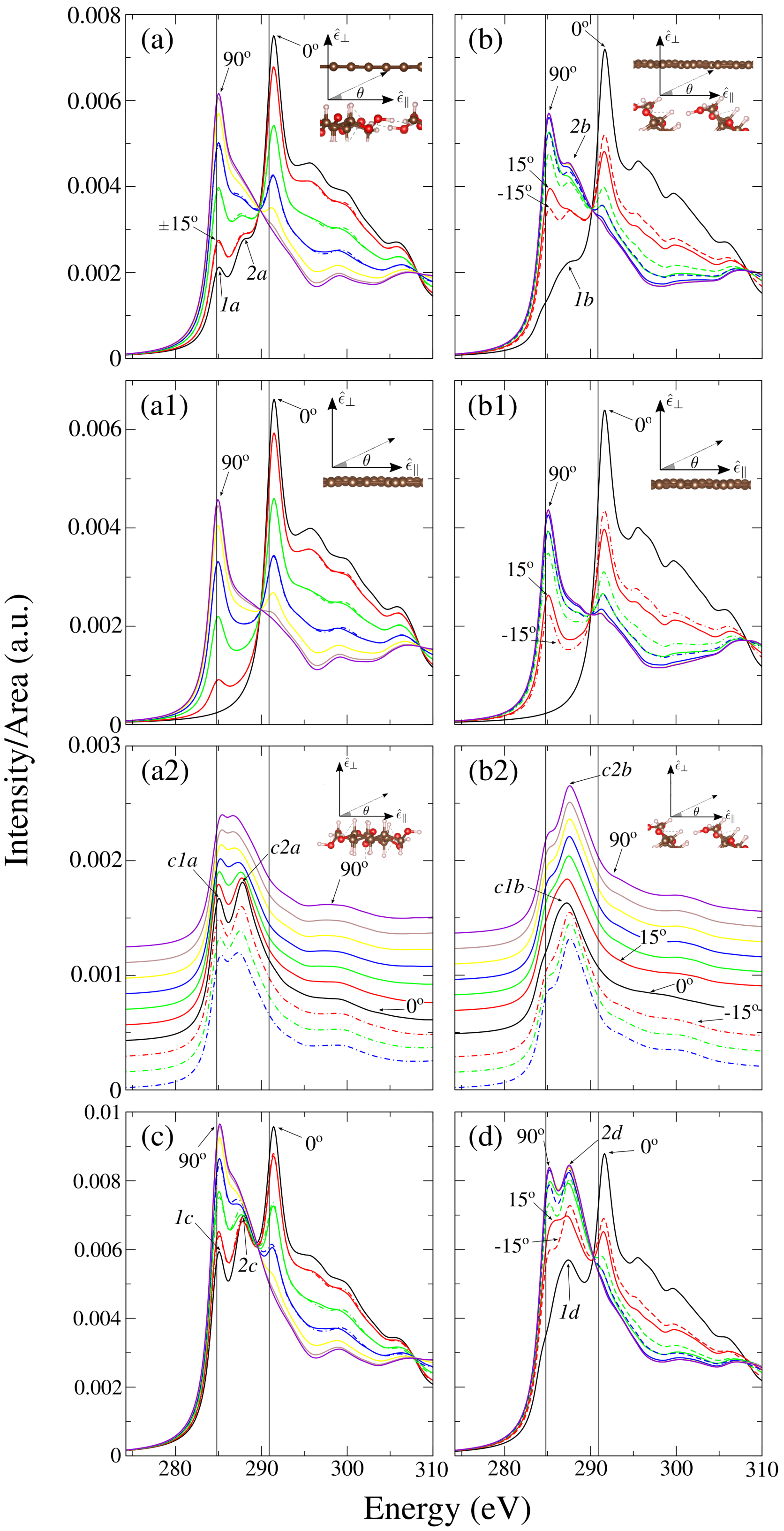

Figure 25 – XANES spectra of nCL$^{\mathrm{phob}}$/G (a) and nCL$^{\mathrm{phil}}$/G (b) interfaces. XANES spectra of hypothetical graphene [(a1)-(b1)] and single layer nCL sheet [(a2)-(b2)] constrained to the equilibrium geometry of the respective final system, nCL$^{\mathrm{phob}}$/G and nCL$^{\mathrm{phil}}$/G, as indicated in the insets. XANES spectra of nCL$_3^{\mathrm{phob}}$/G (c) and nCL$_3^{\mathrm{phil}}$/G (d).

As the formation of the nCL/G heterostructure occurs mainly due vdW interactions, without covalent bonds between the nCL sheet and the graphene layer, the absorption spectra of the nCL/G interfaces are mainly determined by their superposition of isolated components. Indeed, the absorption spectra can be better understood by XANES computations of hypothetical structures, namely, isolated single-layer graphene, and nCL sheet (both) constrained to the respective nCL/G interface equilibrium geometry. The XANES simulations of these constrained structures reveal that the features *1a* and *2a* in nCL$^{\text{phob}}$/G emerge from the superposition of the edge transitions in graphene with the absorption peaks *c1a* and *c2a* of the nCL, Figs. [25(a1) and (a2)]. Similarly, the absorption peak *1b* in nCL$^{\text{phil}}$/G results from the superposition of graphene edge absorption structure with the *c1b* peak of the tilted layer of cellulose fibrils, Figs. [25(b1) and (b2)], and (ii) for $\boldsymbol{\theta = 90^\circ}$ the absorption feature *2b* is composed by the superposition of graphene near-edge structure with the absorption peak *c2b* of the tilted nCL.

The absorption spectra of the nCL/G systems, Figs. 25(a) and (b), were calculated by considering graphene on a single layer of cellulose sheet. However, when the number of nCL sheets increases, it is worthwhile to examine the changes on the XANES spectra. Our results reveal that as the number of nCL layers increases, the absorption characteristics from the C - H and C - OH bonds present a sharpest increase between 285 and 292 eV. In Fig. [25(c) and (d)], we have the absorption spectra for three layers of cellulose fibrils, namely nCL$_3^{\text{phob}}$/G and nCL$_3^{\text{phil}}$/G. In the former interface the absorption peaks *1a* and *2a* become more apparent [labelled as *1c* and *2c* in Fig. 25(c)], similarly the features *1b* and *2b* of nCL$^{\text{phil}}$/G become more intense in nCL$_3^{\text{phil}}$/G, indicated as *1d* and *2d* in Fig. 25(d), reinforcing the differences in the XANES signatures of the hydrophobic and hydrophilic nCL/G interfaces.

6.3 Electronic Properties

The electronic properties of nCL/G present an insulator/semi-metal interface with the linear energy bands of graphene lying within the bandgap of nCL. In Figs. [26(a) and (b)], we present the orbital projected electronic band structures of nCL$^{\text{phob}}$/G and nCL$^{\text{phil}}$/G. Here, we can infer two points: we find (i) the graphene's Dirac-point (DP) at about 2 eV above the valence band maximum (VBM) of the nCL layer; and (ii) the emergence of an energy gap of ∼0.04 eV at the DP. Based on the Bader analysis (137), we found $\boldsymbol{\Delta\rho}$ of $\mathbf{0.23\,(0.28)\times 10^{13}}\ \boldsymbol{e}/\text{cm}^{\mathbf{2}}$ from graphene to the nCL$^{\text{phob}}$/G, (nCL$^{\text{phil}}$/G) interface. This charge keeps accumulated at the nCL/G interface; followed by a reduction of the a graphene work-function (Φ), given by:

$$\Phi = E_{vac} - E_F, \tag{6.2}$$

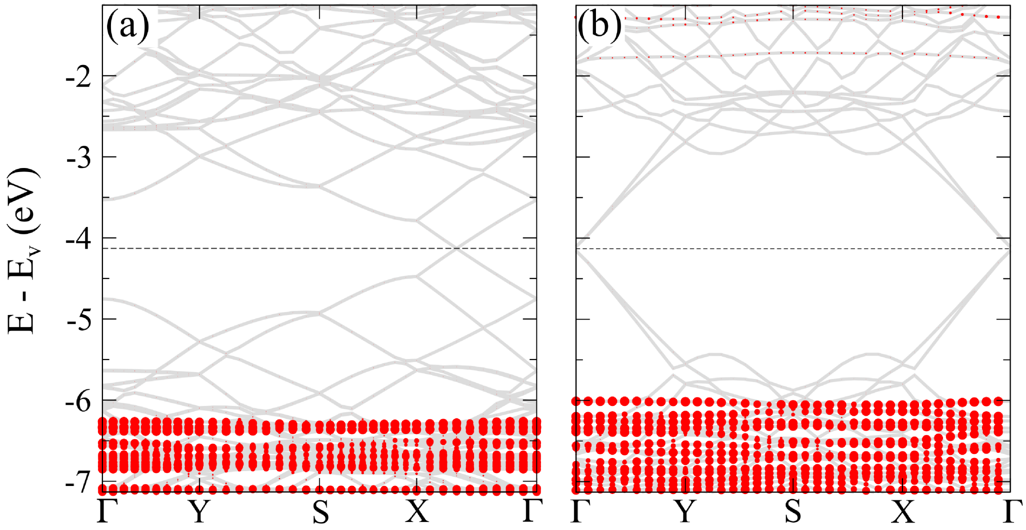

Figure 26 – Electronic band structure of nCL$^{\text{phob}}$/G (a) and nCL$^{\text{phil}}$/G (b). The zero energy was set at the vacuum level, the Fermi level is indicated by the dashed black lines, and red circles indicate cellulose contribution in the band.

where E_{vac} is obtained from the electrostatic potential calculation in a vacuum region far away from the system. This work-function reduction is about 0.2 eV compared with that of the free-standing graphene sheet, 4.33 → 4.13 eV. Similar results were obtained in the nCL$_2^{\text{phob}}$/G and nCL$_2^{\text{phil}}$/G interfaces.

In Figs. [27(a) and (b)] we present a map of these charge accumulations in the nCL$^{\text{phob}}$/G and nCL$^{\text{phil}}$/G interfaces mentioned before. Here is possible to observe some characteristics like (i) the inhomogeneous net charge distribution on the graphene sheets [Figs. 27(a1) and (b1)], which can be attributed to the differences in the orbital hopping between the nCL surface and the graphene's π orbitals[4]; and (ii), as depicted in Figs. [27(a2) and (b2)], those charge transfers occur primarily at the nCL/G interface, since $\Delta\rho \approx 0$ in the subsurface nCL layers, Figs. [27(a3) and (b3)].

The understanding of the electronic properties of the nCL/G interface in the presence of external agents is an important issue for the development of electronic devices based on a combination of cellulosic materials and graphene. Next, we will focus on the effects of external electric field (EEF) and mechanical compressive strain in the nCL/G interface.

Let us start with the effect of EEF, where for each value of the electric field, the atomic positions of the nCL$^{\text{phob}}$/G system were fully relaxed. As shown in Fig. 28, the energy position of the Dirac point with the VBM of the nCL $\boldsymbol{\Delta E_{DP}}$ changes from 1.6 to 2.3 eV in nCL$^{\text{phob}}$/G, and in nCL$^{\text{phil}}$/G, $\boldsymbol{\Delta E_{DP}}$ changes from 1.1 to 2.6 eV for EEF of $\boldsymbol{-0.25}$ and $\boldsymbol{+0.25}$ V/Å, respectively. At same time, the G → nCL net charge transfer, $\boldsymbol{\Delta\rho}$, increases from 0.08 to 0.36 $\times\boldsymbol{10^{13}}\,\boldsymbol{e}/\text{cm}^{\boldsymbol{2}}$ for nCL$^{\text{phob}}$/G meanwhile for nCL$^{\text{phil}}$/G it increases from 0.14 to 0.47 $\times\boldsymbol{10^{13}}\,\boldsymbol{e}/\text{cm}^{\boldsymbol{2}}$. Such tuning of ΔE_{DP} and $\Delta\rho$ is nearly linear to the EEF, with the following rates -1.43 eV/(V/Å) [-3.14 eV/(V/Å)] for ΔE_{DP}, and

---

[4] This might harm graphene's electrical transport.

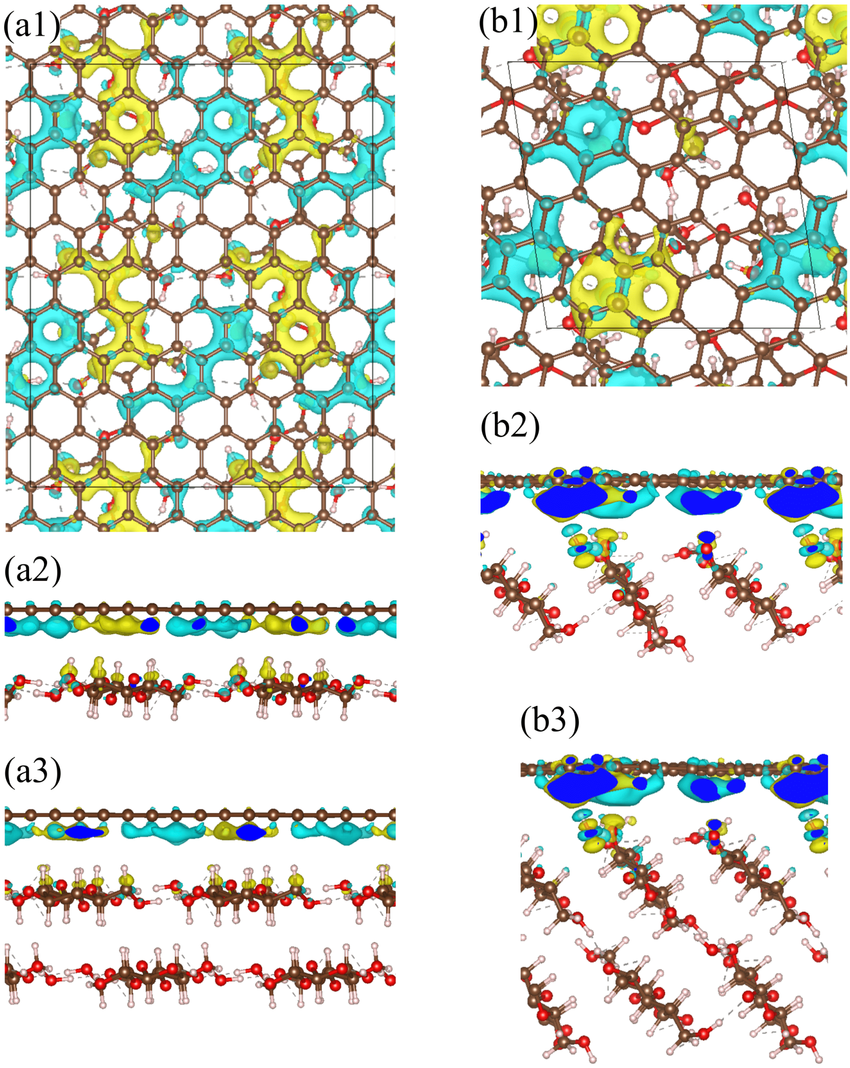

Figure 27 – Net charge transfers ($\Delta\rho$) in nCL$^{\mathrm{phob}}$/G (a1), nCL$^{\mathrm{phil}}$/G (b1), nCL$_2^{\mathrm{phob}}$/G (a2), and nCL$_2^{\mathrm{phil}}$/G (b2). Isosurfaces of 0.4 me/Å^3.

$0.55\,e/\mathrm{cm}^2$ [$0.62\,e/\mathrm{cm}^2$] for $\Delta\rho$ in nCL$^{\mathrm{phob}}$/G [nCL$^{\mathrm{phil}}$/G]. Assuming that such a linear relationship is preserved for larger values of EEF, we can infer that in nCL$^{\mathrm{phil}}$/G the DP becomes resonant with the nCL valence band for EEF > 0.6 V/Å, and thus suppressing the G $\rightarrow$ nCL charge transfer.

Further control of the electronic properties of 2D systems can be achieved through mechanical strain (138, 139). Indeed, such an approach has been used to control the electronic doping level in bilayer graphene and boron-nitride/graphene vdW heterostructures (140, 141). Here, we investigate the net charge transfer, $\Delta\rho$, and the work function (Φ) in nCL/G, as a function of compressive strain. The strain in the nCL$^{\mathrm{phob}}$/G and nCL$^{\mathrm{phil}}$/G interfaces was applied by considering bilayers of nCL and graphene, namely nCL$_2^{\mathrm{phob}}$/GBL [Fig. 29(a)] and nCL$_2^{\mathrm{phil}}$/GBL [Fig. 29(b)]. In Figs. 29(a1) and (a2) we present the spatial distribution of $\Delta\rho$ of pristine nCL$_2^{\mathrm{phob}}$/GBL and compressed by 9 %, respectively; likewise in Figs. 29(b1) and (b2), we show $\Delta\rho$ for the hydrophilic interface, nCL$_2^{\mathrm{phil}}$/GBL. These maps of $\Delta\rho$ reveal that the charge transfers are localized at the nCL$_2$/GBL interface

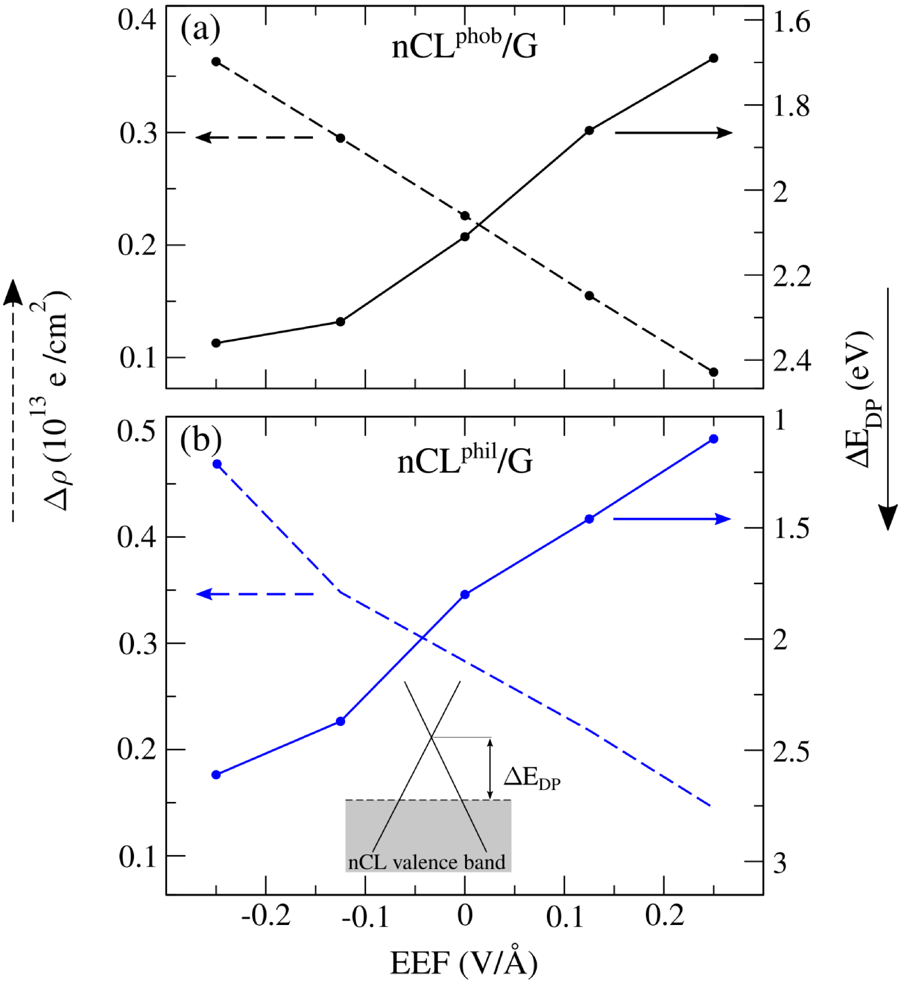

Figure 28 – Energy position of the DP with respect to the VBM (ΔE_{DP} - filled lines), and the net charge transfer ($\Delta\rho$ in $10^{13}\, e/\mathrm{cm}^2$ - dashed lines) as a function of the external electric field (EEF) for the nCL^{phob}/G (a) and nCL^{phil}/B (b) interfaces. Negative values of $\Delta\rho$ indicate a net charge transfer from graphene to the nCL.

region, and as shown in Figs. 30, the net charge transfer from G to the nCL increases up to $\sim 1.0 \times \mathbf{10^{13}}\, \boldsymbol{e}/\mathrm{cm}^{\mathbf{2}}$ in nCL$_2^{phob}$/GBL and 0.8 $\times \mathbf{10^{13}}\, \boldsymbol{e}/\mathrm{cm}^{\mathbf{2}}$ in nCL$_2^{phil}$/GBL for a compressive strain of about 9 %, which corresponds to an external pressure of 3.73 GPa for nCL$_2^{phob}$/GBL and 3.15 GPa for nCL$_2^{phil}$/GBL. At the same time, with the G → nCL charge transfer, we find that the work function increases from 4.64 to 4.73 eV in nCL$_2^{phil}$/GBL and nCL$_2^{phob}$/GBL it increases from 4.68 from 4.88 (Fig. 30).

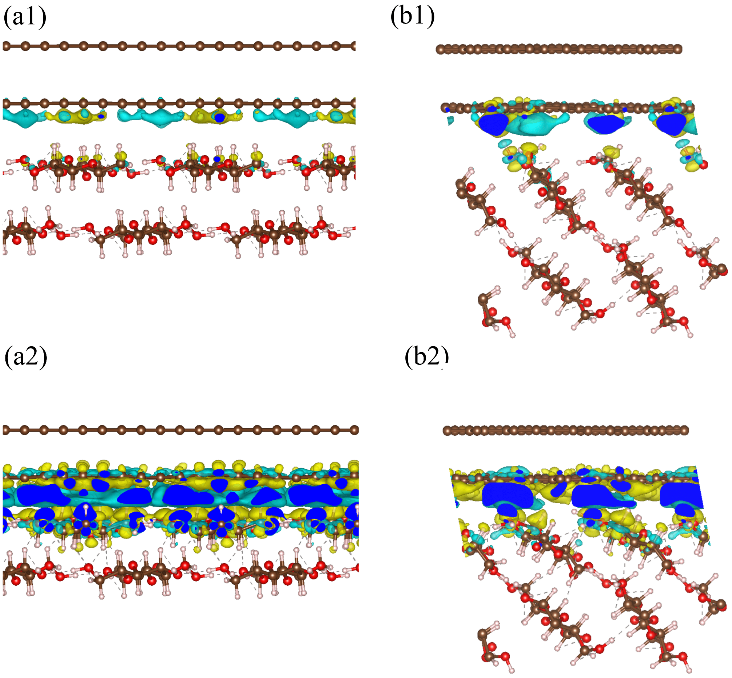

Figure 29 – Side view of differential charge densities of nCL$_2^{\text{phob}}$/GBL (a) to 9% z-compressed nCL$_2^{\text{phob}}$/GBL (b), and nCL$_2^{\text{phil}}$/GBL (c) to 9% z-compressed nCL$_2^{\text{phil}}$/GBL (d). Isosurfaces of 0.4 me/Å^3

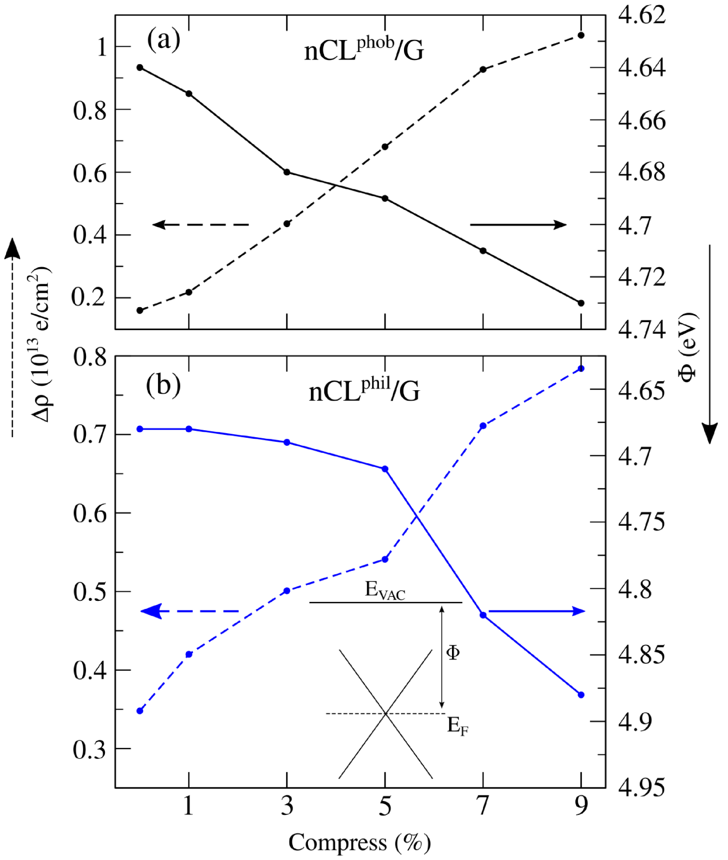

Figure 30 – Net charge tranfer, $\Delta\rho$, and the work function Φ upon compression of nCL$_2^{\text{phob}}$/GBL (a) and nCL$_2^{\text{phil}}$/GBL (b). E$_{\text{vac}}$ represents the vacuum level.

6.4 Conclusions

- The binding energy of nCL/G is primarily ruled by the vdW interactions, being comparable with that of boron-nitride/graphene;
- Through XANES simulations, fingerprints of nCL/G interfaces were identified, being tuned according to the amount of nCL/G sheets in the system;
- The electronic structure of nCL/G is characterized by linear energy bands of graphene lying within the bandgap of nCL, with the Dirac point at about 2 eV above the valence band maximum of the nCL sheet, $\Delta E_{\rm DP} \approx 0.2$eV, and a net charge accumulation, $\Delta\rho$ of $\sim 0.2 \times 10^{13} e/{\rm cm}^2$, localized at the nCL/G interface;
- $\Delta E_{\rm DP}$ varies from 1.6 (1.1) to 2.3 (2.6) eV in nCL$^{\rm phob}$/G (nCL$^{\rm phil}$/G), for EEF of -0.25 and $+0.25\,{\rm V/Å}$, respectively; whereas there is an increase of $\Delta\rho$ up to $1 \times 10^{13} e/{\rm cm}^2$ upon an external pressure of 3.73 GPa.

A The Born-Oppenheimer Approximation

The main idea behind the Born-Oppenheimer approximation (142, 143, 144) is to consider the ratio between the electron and nucleus masses to be sufficiently small, such that the nuclei cannot keep up with the fast change of electrons, and thus are considered fixed. Within the approximation, the nuclear kinetic energy term,

$$\hat{T}_n = \sum_{A=1}^{m} - \left(\frac{1}{2} \frac{1}{m_A} \nabla_A^2 \right) \tag{A.1}$$

is much smaller than the other terms. So for $m_A \to \infty$ we have:

$$\hat{H} = \hat{T}_n + \hat{T} + \hat{V}_{ne} + \hat{V}_{ee} + \hat{V}_n \Longrightarrow \hat{T} + \hat{V}_{ne} + \hat{V}_{ee} + \hat{V}_n = \hat{H}_T \tag{A.2}$$

where $\hat{H}_T$ is the total Hamiltonian of the system. The Hamiltonian $\hat{H}_T$ will then be given by:

$$\hat{H}_T = \hat{H}_e + \hat{V}_n, \tag{A.3}$$

where the electronic hamiltonian is given by:

$$\hat{H}_e = \hat{H} = \hat{T} + \hat{V}_{ne} + \hat{V}_{ee}, \tag{A.4}$$

which is the same Hamiltonian as the equation (2.3).

There are some cases where the approximation is not valid, as in crossing potential curves, as it leads to strong coupling. However, the vast majority of theoretical studies use the approximation of Born-Oppenheimer.

B Funcionals Derivative

A functional can be defined as an application that assigns to $f(x)$ the number F, and $f(x)$ is said to be the function argument of the functional (145). For any $f(x)$ function that leads to some dx variation in its domain, we have:

$$f(x+dx) = f(x) + \frac{df}{dx}dx + \frac{d^2 f}{dx^2}dx^2 + \dots . \tag{B.1}$$

For a functional, we proceed in the same way, such that:

$$F[f(x) + \delta f(x)] = F[f(x)] + \int s(x)\delta f(x) dx + \dots , \tag{B.2}$$

where $s(x) \equiv \frac{\delta F[f(x)]}{\delta f(x)}$ is the derivative of the functional $F[f]$. The derivative of a functional is essential in the study of functional analysis and methods/theories involving functional in calculations, such as the DFT.

We can indicate a general expression for obtaining the derivative of a functional $F[n] = \int f(n, n', n'', \dots ; x)dx$, where $n = n(x)$ and n^i the i-th derivative with respect to x, which will be given by:

$$\frac{\delta F[n]}{\delta n(x)} = \frac{\partial f}{\partial n} - \frac{d}{dx}\frac{\partial f}{\partial dn'} - \frac{d^2}{dx^2}\frac{\partial f}{\partial dn''} + \dots . \tag{B.3}$$

An example of a classical functional in physics is an action functional analyzed in classical mechanics:

$$S = \int L(q, q', q'', \dots, t)dt, \tag{B.4}$$

where the Lagrangian of a dynamical system is represented by $L(q, q', q'', \dots, t)$. The Lagrangian of this system is a function of the generalized coordinates, velocities, and time, while s is an integer, which makes the Lagrangian functional.

Using the equation (B.3) for the Lagrangian, the equation that describes the evolution of the dynamical system will be given when maximizing the action, so:

$$\frac{\delta S[q]}{\delta q(t)} = \frac{\partial L}{\partial q} - \frac{d}{dt}\frac{\partial L}{\partial q'} = 0. \tag{B.5}$$

Therefore, the equation (B.5) is the Lagrange equation which will be the equation of motion when the Lagrangian of the system is determined.

C The Variational Principle

Through the variational principle, we can obtain an upper boundary very close to the exact value of the ground state energy E_0 (146). By choosing a trial wave function Ψ_t such that

$$\langle \Psi_t | \Psi_t \rangle = 1, \tag{C.1}$$

The variational principle assures us that we will always have to:

$$E_0 \; \leq \; \langle \Psi_t | \hat{H} | \Psi_t \rangle \; \equiv \; \langle \hat{H} \rangle. \tag{C.2}$$

In the equation (C.2), $\langle \hat{H} \rangle$ represents the expected value of the Hamiltonian in some excited state. If Ψ_t is a solution of some state excited n, we will have to

$$E_n \; = \; \langle \Psi_t | \hat{H} | \Psi_t \rangle \; \geq \; E_0. \tag{C.3}$$

Since we know that the eigenfunctions Ψ_n that are the solutions of the Hamiltonian $\hat{H}$ form a complete set of solutions, we can write any function Ψ_t as a linear combination of the eigenfunctions, that is,

$$\Psi_t = \sum_n C_n \Psi_n, \tag{C.4}$$

where $\hat{H}\Psi_n = E_n \Psi_n$. If the trial wavefunction Ψ_t is normalized, we can rewrite the equation (C.1) as follows:

$$\begin{aligned} \langle \Psi_t | \Psi_t \rangle &= 1 \\ \langle \sum_m C_m \Psi_m | \sum_n C_n \Psi_n \rangle \; &= \; 1 \\ \sum_m \sum_n C_m^* C_n \langle \Psi_m | \Psi_n \rangle \; &= \; 1 \\ \sum_m \sum_n C_m^* C_n \delta_{mn} \; &= \; 1 \\ \sum_n |C_n|^2 \; &= \; 1. \end{aligned} \tag{C.5}$$

The expected value for the Hamiltonian in another excited state is given by

$$\begin{aligned} \langle \hat{H} \rangle \; &= \; \langle \Psi_t | \hat{H} | \Psi_t \rangle \\ = \; \langle \sum_m C_m \Psi_m | \hat{H} | \sum_n C_n \Psi_n \rangle \; &= \; \sum_m \sum_n C_m^* C_n \langle \Psi_m | \hat{H} \Psi_n \rangle \\ = \; \sum_m \sum_n C_m^* C_n \langle \Psi_m | E_n \Psi_n \rangle \; &= \; \sum_m \sum_n C_m^* C_n E_n \langle \Psi_m | \Psi_n \rangle \\ &= \; \sum_m \sum_n C_m^* C_n E_n \delta_{mn} \\ \langle H \rangle \; &= \; \sum_n |C_n|^2 E_n. \end{aligned} \tag{C.6}$$

We know that the energy of any excited state will always be greater than the energy of the ground-state. Mathematically speaking, we know that $E_n \geq E_0$. This allows us to write the equation (C.5) as follows:

$$\langle \hat{H} \rangle \; = \; \sum_n |C_n|^2 E_n \; \geq \; \sum_n |C_n|^2 E_0. \tag{C.7}$$

As we saw from the equation (C.5), the equation (C.7) can be rewritten as

$$\langle \hat{H} \rangle = E_n \geq E_0. \tag{C.8}$$

Therefore, we were able to demonstrate that the expected value of the Hamiltonian in any state is always greater than or equal to the energy of the ground state, that is:

$$\langle \hat{H} \rangle \geq E_0. \tag{C.9}$$

D X-Ray Absorption Near-Edge Structure

X-rays are electromagnetic waves with energy between 100 eV and 100 keV, which is equivalent to wavelengths between 12 and 0.01 nm and frequencies between 2×10^{16} and 2×10^{19} Hz. When interacting with matter, the X-ray photon can be absorbed: its energy is used to excite an atom, causing an electron to be promoted to an energy level higher than the level it was at. When the energy of the photon is greater than the binding energy of the electron, the electron is ejected from the atom with kinetic energy equal to the difference between the energy of the absorbed photon ($\hbar\omega$) and the binding energy of the electron (E_i), such that $T = \hbar\omega - E_i$. When an X-ray beam strikes a material, its intensity decreases because of the absorption of photons. This decrease is described by the Lambert-Beer law:

$$I = I_0 e^{-\mu t} \tag{D.1}$$

where I is the intensity of the beam passing through the sample, I_0 is the intensity of the incident beam, t is the thickness of the sample and μ is the absorption coefficient that depends on the material and the energy of the X-rays.

From an X-ray absorption spectrum, we can obtain information about the electronic levels of an atom, and the basic process involves the excitation of electrons from occupied levels to unoccupied levels. Figure 31, adapted from (147) shows a graph of the absorption

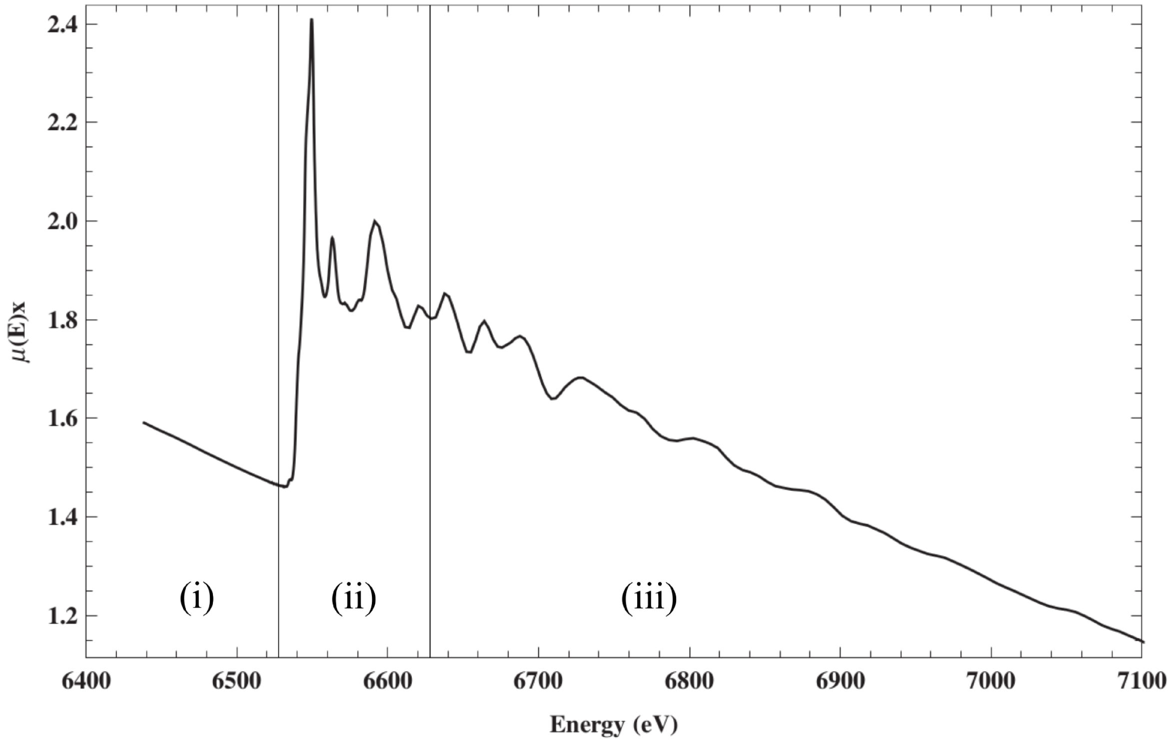

Figure 31 – Absorption coefficient x Energy - adapted from (147)

coefficient (μ) as a function of energy. We can observe three characteristics:

(i) a general decrease in X-ray absorption with increasing energy,

(ii) the presence of an abrupt increase in absorption at a given energy, called absorption edge,

(iii) above the edge, an oscillatory structure that modulates absorption.

The second feature illustrates the phenomenon of X-ray absorption, described by Fermi's golden rule (148).

The edge energy position is unique for a given absorbing atom and reflects the excitation energy of the electrons in the innermost layers, making the technique sensitive to the element studied. The third feature is precisely what is of interest to the EXAFS technique. When interpreted correctly, it is possible to obtain detailed information on the crystal structure of the material studied.

The absorption spectrum (Figure 31) is divided into three regions:

- Pre-edge region: refers to electronic transitions with absorption energy lower than the binding energy, occurs when the absorbing atom has unoccupied or partially unoccupied states below the Fermi energy. Such transitions are unlikely to occur and therefore produce only small oscillations in the absorption spectrum (Region (i) in figure 31);
- Absorption edge: is the region characterized by the discontinuity of the absorption spectrum. It happens when the energy absorbed is enough to knock electrons from the absorbing atom. The exact position of the peak depends on the details of the oxidation state, symmetry of the site of the absorbing atom (octahedral, tetrahedral, etc.) and the nature of the chemical bonds;
- Transitions to the continuum states: corresponds to the absorption of photons with energies greater than the binding energy of the electron, so that transitions to continuous states, not located in the absorbing atom, occur, and the excess energy is carried by the photoelectron (the electron that was ripped from the atom after absorbing the X-ray photon) in the form of kinetic energy. This part of the spectrum is divided into:
    - ⋆ XANES (X-ray Absorption Near Edge Structure) region: range of the absorption spectrum that goes up to 50 eV above the absorption edge, where intense variations in absorption occur. In this interval, the photoelectron's wavelength is of the order of atomic distances and, therefore, its mean free path is small; multiple scatterings occur before returning to the absorbing atom (Region (ii) in figure 31);

- ⋆ EXAFS (Extended X-ray Absorption Fine Structure) region: range that goes from 50 to 1000 eV above the absorption edge and presents smoother oscillations (fine structure). These oscillations have information about the atomic structure around the absorbing atom. In this region, the mean free path of the photoelectron is large and simple scatterings (where the photoelectron encounters only one scatterer and returns to the absorbing atom) are more likely (Region (iii) in figure 31).

Here, we will be focused only on XANES. XANES can provide physical and chemical information about the surroundings of a given element through direct comparison with the spectra of standard samples. In this sense, the XANES spectrum is considered a fingerprint of the local three-dimensional electronic structure. In the region of the spectrum close to the absorption edge, the photoelectron has a shorter mean free path, which provides a stronger interaction between the photoelectron and the potential of the scattering atoms. Thus, it is possible to obtain information about the geometric distribution of atoms (such as bond angles and atomic positions) through a complete analysis of the multiple scatterings that contribute to the absorption signal in the XANES region. To try to explain and predict the phenomena present in the XANES region, it is necessary to use, and sometimes implement, particular ad-hoc methodologies appropriate for each situation. In the analysis of the spectroscopic results of bound electronic states, it is necessary to describe the initial state, the final state and the absorption cross-section as a function of the interaction Hamiltonian. This involves proposing models that consider different effects of the processes involved to investigate the atomic structure (149).

In every ionization process, holes are produced in the electronic layer, and this has at least three relevant effects that must be considered in the proposed models:

- the atom has one less electron in its innermost levels, which can be considered as an increase in its atomic number (Z + 1);
- innermost bound states with non-zero angular momentum result in spin-orbit coupling splits;
- unfolding of the coupling between internal states and valence states with non-zero angular momentum

The simulation of absorption spectra and electronic structure using basic principles has been shown to be a very efficient tool in understanding structures in the XANES region. In general, the objective of these simulations is to obtain the absorption spectra using calculations based on information about the structure (atomic, electronic and magnetic) of the material.

E Implicit Solvent Model

When *ab initio* of the solute/solvent system treatment becomes necessary, there are two ways to proceed with the treatment. The first consists of all solvent molecules that must be considered explicitly. The equilibrium final state is reached after the full relaxation of the system, which is quite expensive as the number of solvent molecules in the system required to capture the essential equilibrium properties is huge and because of the statistical averaging required for the solvent molecules. The second one is to treat the solute quantum-mechanically and to treat the solvent as a continuum, which means that the solute is immersed in a bath of solvent and the average over the solvent degrees of freedom becomes implicit in the properties of the solvent bath. The implicit solvent model offers a much more computationally tractable way to change the solute's electronic and geometric degrees of freedom so that its ground state complies with the solvent bath's equilibrium properties. This method provided all interactions between the solute and the solvent are properly taken into account and can be quite accurate because the solute electron structure is still being treated in a quantum-mechanical way (126, 127).

The free energy A of the combined solute/solvent system can be written as a sum of two terms: (i) a universal functional F of the total electron density, and (ii) the thermodynamically averaged atomic densities of the solvent species, and a term describing the electrostatic energy contribution, given by:

$$A = F[\rho_{\text{tot}}, \{N_i(\boldsymbol{r})\}] + \int d^3r \; V_{\text{ee}}(\boldsymbol{r}) \left(\sum_i Z_i N_i(\boldsymbol{r}) - N_{\text{tot}}(\boldsymbol{r}) \right), \tag{E.1}$$

where $\rho_{\text{tot}}(\boldsymbol{r}) = \rho_{\text{sol}}(\boldsymbol{r}) + \rho_{\text{solv}}(\boldsymbol{r})$ is the total electron density (the sum of the electron density of the solute and the solvent), $N_i(\boldsymbol{r})$ are the thermodynamically averaged atomic densities associated with the chemical species i in the solvent, $V_{\text{ee}}(\boldsymbol{r})$ s the external potential due to the solute nuclei, and F is a universal functional. Minimizing Eq. (E.1) with respect to the solvent electron density ρ_{solv}, we obtain:

$$\tilde{A} = G[\rho_{\text{sol}}(\boldsymbol{r}), \{N_i(\boldsymbol{r})\}, V_{\text{ee}}(\boldsymbol{r})] - \int d^3r \; V_{\text{ee}}(\boldsymbol{r}) \rho_{\text{sol}}(\boldsymbol{r}), \tag{E.2}$$

where

$$G[\rho_{\text{sol}}(\boldsymbol{r}), \{N_i(\boldsymbol{r})\}, V_{\text{ee}}(\boldsymbol{r})] = \min_{\rho_{\text{solv}}} \left\{ F[\rho_{\text{tot}}, \{N_i(\boldsymbol{r})\}] - \int d^3r \; V_{\text{ee}}(\boldsymbol{r}) \left(\sum_i Z_i N_i(\boldsymbol{r}) - N_{\text{tot}}(\boldsymbol{r}) \right) \right\} \tag{E.3}$$

The term G is a universal functional of the electron density of the solute ρ_{sol}, the average atomic densities of the various species in the solvent $\{N_i(\boldsymbol{r})\}$, and the external potential of the solute nuclei $V_{\text{ee}}(\boldsymbol{r})$. The functional G can also be separated as:

$$G[\rho_{\text{sol}}(\boldsymbol{r}), \{N_i(\boldsymbol{r})\}, V_{\text{ee}}(\boldsymbol{r})] = A_{KS}[\rho_{\text{sol}}(\boldsymbol{r}), V_{\text{ee}}(\boldsymbol{r})] + A_{\text{diel}}[\rho_{\text{sol}}(\boldsymbol{r}), \{N_i(\boldsymbol{r})\}, V_{\text{ee}}(\boldsymbol{r})], \tag{E.4}$$

where A_{KS} is the usual Kohn-Sham density functional for the solute and $\mathrm{A}_{\mathrm{diel}}$ is the term that encapsulates all the interactions of the solute with the solvent and the internal energy of the solvent. To further simplify the expression, the functional $\mathrm{A}_{\mathrm{diel}}$ is minimized with respect to the average atomic densities of the solvent $\{N_i(\boldsymbol{r})\}$, given by:

$$\tilde{A}_{\mathrm{diel}}[\rho_{\mathrm{sol}}(\boldsymbol{r}), V_{\mathrm{ee}}(\boldsymbol{r})] = \min_{\{N_i(\boldsymbol{r})\}} A_{\mathrm{diel}}[\rho_{\mathrm{sol}}(\boldsymbol{r}), \{N_i(\boldsymbol{r})\}, V_{\mathrm{ee}}(\boldsymbol{r})]. \tag{E.5}$$

An electrostatic-only approach is insufficient to describe the solvation of molecules and nanoparticles, where cavitation and dispersion may play a significant role. Including in $\tilde{A}_{\mathrm{diel}}$ an additional term to describe the free energy contributions of cavitation and dispersion, we have so:

$$A_{\mathrm{cav}} = \tau \int d^3r |\nabla S|, \tag{E.6}$$

where τ is the effective surface tension parameter, which describes the cavitation, dispersion, and repulsion interaction between the solute and the solvent that are not captured by the electrostatic terms alone and $S(\boldsymbol{r})$ is the cavity shape function described by:

$$S(\rho_{\mathrm{sol}}(\boldsymbol{r})) = \frac{1}{2}\mathrm{erfc}\left\{\frac{\log(\rho_{sol} - \rho_c)}{\sigma\sqrt{2}}\right\}, \tag{E.7}$$

with the parameters ρ_c and σ, that determine respectively at what value of the electron density the dielectric cavity forms, and the width of the diffuse cavity. Decoupling the electrostatic term from the Kohn-Sham functional A_{KS} and combining it with the interaction term and the cavitation term, we obtain:

$$A[\rho_{\mathrm{sol}}(\boldsymbol{r}), \phi(\boldsymbol{r})] = A_{\mathrm{TXC}}[\rho_{\mathrm{sol}}(\boldsymbol{r})] + \int d^3r\phi(\boldsymbol{r})(N_{\mathrm{sol}}(\boldsymbol{r}) - n_{\mathrm{sol}}(\boldsymbol{r})) - \int d^3r\epsilon(\boldsymbol{r})\frac{|\nabla\phi|^2}{8\pi} + A_{\mathrm{cav}}, \tag{E.8}$$

where A_{TXC} is the free energy density functional describing the kinetic and exchange-correlation energy of the solute and $N_{\mathrm{sol}}(\boldsymbol{r}$ is the solute nuclear charge density. The term $\phi(\boldsymbol{r})$ is the combined electrostatic potential due to the electronic $n_{\mathrm{sol}}(\boldsymbol{r})$ and nuclear $(N_{\mathrm{sol}}(\boldsymbol{r}))$ charges of the solute system in a polarizable medium, which is different from V_{ee}, this being the potential due to the nuclei in the solute. Outside a specified cutoff radius, it has the form $\frac{Z_{\mathrm{eff}}}{r}$, where Z_{eff} is the effective charge of the respective atom. Since the solvent described by $\epsilon(\boldsymbol{r})$ does not penetrate the core region of the pseudopotentials, we can approximate the contribution of the nuclear charges to the combined electrostatic potential $\phi(\boldsymbol{r})$ of the solute by a sum over terms of the form $\frac{Z_{\mathrm{eff}}}{r}$. Minimization of Eq. E.8 with respect to electronic charge density $n_{\mathrm{sol}}(\boldsymbol{r})$, leads to a typical Kohn-Sham Hamiltonian with the following additional terms in the local part of the potential:

$$V_{\mathrm{solv}} = \frac{d\epsilon(\rho_{\mathrm{sol}}(\boldsymbol{r}))}{d\rho_{\mathrm{sol}}(\boldsymbol{r})}\frac{|\nabla\phi|^2}{8\pi} + \tau\frac{d|\nabla S|}{d\rho_{\mathrm{sol}}(\boldsymbol{r})}. \tag{E.9}$$

F Computational Details

F.1 Chapters 3 and 4

All calculations were performed within the density functional theory (DFT), where the exchange-correlation term was described by the generalized gradient approximation (GGA-PBE) (76) proposed by Perdew, Burke and Ernzerhof. The periodic image interaction was avoided by using at least 15 Å vacuum. The Kohn-Sham orbitals were expanded in a plane wave basis set with an energy cutoff of 400 eV and the electron-ion interaction have been evaluated using the PAW (projected augmented wave) method (150). The Brillouin Zone (BZ) sampling was performed according to the Monkhorst-Pack scheme (151), using a 12×12×1 mesh. Binding energies, equilibrium geometry and electronic properties were performed using Vienna Ab-initio Simulation Package (VASP) (152). The equilibrium configuration was calculated taking into account fully relaxed atomic positions, considering convergence criteria of 25 meV/Å for the atomic forces.

The boron K-edge X-ray absorption near-edge structure (XANES) spectra were simulated using the theoretical approach implemented in the XSpectra code,(153, 129, 154) supplied with QUANTUM ESPRESSO(155). We have used ultrasoft pseudopotentials, where in order to describe the K-edge spectra, we built a pseudopotential with a core hole in the 1*s* orbital, and the all-electron wave function was recovered by using the GIPAW(156) approach. We have considered a set of 12×12×1 k-points to the BZ sampling (relax) and 200 k-points along Γ-X-S-Y-Γ direction (band), energy cutoffs of 40 Ry for the plane wave basis set (to expand the KS orbitals) and 400 Ry for the self-consistent total charge density.

F.2 Chapter 5

All calculations were performed within the density functional theory (DFT), where the exchange-correlation term was described by the generalized gradient approximation (GGA-PBE) (76) proposed by Perdew, Burke and Ernzerhof. The periodic image interaction was avoided by using at least 12 Å vacuum perpendicular to the graphene sheet. The Kohn-Sham orbitals were expanded in a plane wave basis set with an energy cutoff of 48 Ry (we have verified the convergence by increasing the cutoff energy up to 60 Ry), and the electron-ion interaction has been evaluated using the PAW (projected augmented wave) method (150). The Brillouin Zone (BZ) sampling was performed according to the Monkhorst-Pack scheme (151), using a 3×3×1 mesh for cellulosic chains and 3×3×3 for cellulose crystal phase. The equilibrium configuration was calculated taking into account fully relaxed atomic positions and the lattice vectors, considering convergence criteria of 25 meV/Å for the atomic forces on each atom.

In order to perform a thorough study of the role played by the van der Waals (vdW) forces in the structural stability of the cellulose nanofibers, we have taken into account different approaches for the vdW interactions, *viz.*: (i) vdW density functional (vdW-DF) (101, 100, 102, 103) implemented in the QE and VASP codes, (ii) parameterized vdW-D2 (78) implemented in the QE code, (iii) vdW-DF2 (157), and (iv) vdW-optB86b (158, 82) both implemented in the VASP code(152).

F.3 Chapter 6

All calculations were performed within the density functional theory (DFT), where the exchange-correlation term was described by the generalized gradient approximation (GGA-PBE) (76) proposed by Perdew, Burke and Ernzerhof. The periodic image interaction was avoided by using at least 25 Å vacuum perpendicular to the graphene sheet. The Kohn-Sham orbitals were expanded in a plane wave basis set with an energy cutoff of 400 eV and the electron-ion interaction has been evaluated using the PAW (projected augmented wave) method (150). The Brillouin Zone (BZ) sampling was performed according to the Monkhorst-Pack scheme (151), using a 6×6×1 mesh(relax) and 20 k-points along Γ-X-S-Y-Γ direction (band). The search for binding energies, equilibrium geometry and electronic properties was performed using Vienna Ab-initio Simulation Package (VASP) (152), and the influence of an aqueous environment was simulated based on the implicit solvation model implemented in DFT code VASP (VASPsol (126, 127)). The equilibrium configuration was calculated taking into account fully relaxed atomic positions, considering convergence criteria of 25 meV/Å for the atomic forces. To provide a more complete picture of the energetic features of the nCL/G interfaces, we have examined the role played by the vdW dispersion interaction on the nCL/G binding energies. We have considered two different non-local vdW approaches, viz.: vdW-DF (101, 100, 103), and vdW-optB86b (158, 82).

The Carbon K-edge X-ray absorption near edge structure (XANES) spectra were simulated using XSpectra package (153, 129, 154), implemented in Quantum ESPRESSO (155, 102). To describe the K-edge spectra, we used a reconstructed ultrasoft pseudopotential with a core-hole in C-1s orbital and the electron wave functions were recovered using GIPAW (156) reconstruction. Here, the BZ sampling was the same as previously described and the energy cutoffs for the plane wave basis set and self-consistent total charge density were respectively 48 and 192 Ry.

G Published Articles

Here we will list the published articles which are related to this work:

Chapter 3

- ⋆ SILVESTRE, G.; SCOPEL, W. L.; MIWA, R. Electronic stripes and transport properties in borophene heterostructures. Nanoscale, Royal Society of Chemistry, v. 11, n. 38, p. 17894–17903, 2019 (45).

Chapter 5

- ⋆ SILVESTRE, G. H. et al. Disassembly of tempo-oxidized cellulose fibers: Intersheet and interchain interactions in the isolation of nanofibers and unitary chains. The Journal of Physical Chemistry B, ACS Publications, v. 125, n. 14, p. 3717–3724, 2021 (105).
- ⋆ PETRY, R. et al. Machine learning of microscopic ingredients for graphene oxide/cellulose interaction. Langmuir, ACS Publications, v. 38, n. 3, p. 1124–1130, 2022 (123).

Chapter 6

- ⋆ SILVESTRE, G. H. et al. Nanoscale structural and electronic properties of cellulose/graphene interfaces. arXiv preprint arXiv:2208.11742, 2022, (up-to-dated in reference (159)).

Bibliography

1 NOVOSELOV, K. S. et al. Electric field effect in atomically thin carbon films. *Science*, American Association for the Advancement of Science, v. 306, n. 5696, p. 666–669, 2004. DOI: <https://doi.org/10.1126/science.1102896>.

2 GEIM, A. K.; NOVOSELOV, K. S. The rise of graphene. *Nature materials*, Nature Publishing Group, v. 6, n. 3, p. 183, 2007. DOI: <https://doi.org/10.1038/nmat1849>.

3 NOBELPRIZE.ORG. *The Nobel Prize in Physics* 2010. 2010.

4 PENEV, E. S. et al. Polymorphism of two-dimensional boron. *Nano letters*, ACS Publications, v. 12, n. 5, p. 2441–2445, 2012. DOI: <https://doi.org/10.1021/nl3004754>.

5 WU, X. et al. Two-dimensional boron monolayer sheets. *ACS nano*, ACS Publications, v. 6, n. 8, p. 7443–7453, 2012. DOI: <https://doi.org/10.1021/nn302696v>.

6 MANNIX, A. J. et al. Synthesis of borophenes: Anisotropic, two-dimensional boron polymorphs. *Science*, American Association for the Advancement of Science, v. 350, n. 6267, p. 1513–1516, 2015. DOI: <https://doi.org/10.1126/science.aad1080>.

7 FENG, B. et al. Experimental realization of two-dimensional boron sheets. *Nature chemistry*, Nature Publishing Group, v. 8, n. 6, p. 563, 2016. DOI: <https://doi.org/10.1038/nchem.2491>.

8 BERGERON, H.; LEBEDEV, D.; HERSAM, M. C. Polymorphism in post-dichalcogenide two-dimensional materials. *Chemical Reviews*, ACS Publications, v. 121, n. 4, p. 2713–2775, 2021. DOI: <10.1021/acs.chemrev.0c00933>.

9 TAO, M.-L. et al. Gallenene epitaxially grown on Si (111). *2D Materials*, IOP Publishing, v. 5, n. 3, p. 035009, 2018. DOI: <https://doi.org/10.1088/2053-1583/aaba3a>.

10 TAO, L. et al. Silicene field-effect transistors operating at room temperature. *Nature nanotechnology*, Nature Publishing Group, v. 10, n. 3, p. 227, 2015. DOI: <https://doi.org/10.1038/nnano.2014.325>.

11 VOON, L. L. Y.; ZHU, J.; SCHWINGENSCHLöGL, U. Silicene: Recent theoretical advances. *Applied Physics Reviews*, AIP Publishing LLC, v. 3, n. 4, p. 040802, 2016. DOI: <https://doi.org/10.1063/1.4944631>.

12 DERIVAZ, M. et al. Continuous germanene layer on Al (111). *Nano letters*, ACS Publications, v. 15, n. 4, p. 2510–2516, 2015. DOI: <https://doi.org/10.1021/acs.nanolett.5b00085>.

13 LI, L. et al. Black phosphorus field-effect transistors. *Nature nanotechnology*, Nature Publishing Group, v. 9, n. 5, p. 372, 2014. DOI: <https://doi.org/10.1038/nnano.2014.35>.

14 ZHANG, R.; LI, Z.; YANG, J. Two-Dimensional Stoichiometric Boron Oxides as a Versatile Platform for Electronic Structure Engineering. *The Journal of Physical Chemistry Letters*, ACS Publications, v. 8, n. 18, p. 4347–4353, 2017. DOI: <https://doi.org/10.1021/acs.jpclett.7b01721>.

15 HUANG, C. et al. Lateral heterojunctions within monolayer $MoSe_2$–WSe_2 semiconductors. *Nature materials*, Nature Publishing Group, v. 13, n. 12, p. 1096, 2014. DOI: <https://doi.org/10.1038/nmat4064>.

16 LING, X. et al. Parallel stitching of 2D materials. *Advanced Materials*, Wiley Online Library, v. 28, n. 12, p. 2322–2329, 2016. DOI: <https://doi.org/10.1038/nmat4064>.

17 LEDUR, C. M. et al. Ab initio simulation of functionalized β_{12} borophene. *Disciplinarum Scientia | Naturais e Tecnológicas*, v. 21, n. 3, p. 89–98, 2020. DOI: <https://doi.org/10.37779/nt.v21i3.3570>.

18 GONG, Y. et al. Vertical and in-plane heterostructures from WS_2/MoS_2 monolayers. *Nature materials*, Nature Publishing Group, v. 13, n. 12, p. 1135, 2014. DOI: <https://doi.org/10.1038/nmat4091>.

19 SOUZA, P. H. et al. Magnetic anisotropy energies and metal-insulator transitions in monolayers of α-$RuCl_3$ and $OsCl_3$ on graphene. *Phys. Rev. B*, American Physical Society, v. 106, p. 155118, Oct 2022. DOI: <https://doi.org/10.1103/PhysRevB.106.155118>.

20 GLAVIN, N. R. et al. Emerging applications of elemental 2D materials. *Advanced Materials*, Wiley Online Library, v. 32, n. 7, p. 1904302, 2020. DOI: <https://doi.org/10.1002/adma.201904302>.

21 LIU, X.; HERSAM, M. C. 2D materials for quantum information science. *Nature Reviews Materials*, Nature Publishing Group, v. 4, n. 10, p. 669–684, 2019. DOI: <https://doi.org/10.1038/s41578-019-0136-x>.

22 AHN, E. C. 2D materials for spintronic devices. *NPJ 2D Materials and Applications*, Nature Publishing Group, v. 4, n. 1, p. 1–14, 2020. DOI: <https://doi.org/10.1038/s41699-020-0152-0>.

23 LIMA, F. Crasto de; FERREIRA, G.; MIWA, R. Layertronic control of topological states in multilayer metal-organic frameworks. *The Journal of Chemical Physics*, AIP Publishing LLC, v. 150, n. 23, p. 234701, 2019. DOI: <https://doi.org/10.1063/1.5100679>.

24 NOVOSELOV, K. et al. 2D materials and van der Waals heterostructures. *Science*, American Association for the Advancement of Science, v. 353, n. 6298, p. aac9439, 2016. DOI: <https://doi.org/10.1126/science.aac9439>.

25 SCHULMAN, D. S.; ARNOLD, A. J.; DAS, S. Contact engineering for 2D materials and devices. *Chemical Society Reviews*, Royal Society of Chemistry, v. 47, n. 9, p. 3037–3058, 2018. DOI: <https://doi.org/10.1039/C7CS00828G>.

26 RANJAN, P. et al. Borophene: New sensation in flatland. *Advanced Materials*, Wiley Online Library, v. 32, n. 34, p. 2000531, 2020. DOI: <https://doi.org/10.1002/adma.202000531>.

27 WU, X. et al. Two-dimensional boron monolayer sheets. *ACS Nano*, ACS Publications, v. 6, n. 8, p. 7443–7453, 2012. DOI: <https://doi.org/10.1021/nn302696v>.

28 WANG, V.; GENG, W.-T. Lattice defects and the mechanical anisotropy of borophene. *The Journal of Physical Chemistry C*, ACS Publications, v. 121, n. 18, p. 10224–10232, 2017. DOI: <https://doi.org/10.1021/acs.jpcc.7b02582>.

29 PENG, B. et al. The electronic, optical, and thermodynamic properties of borophene from first-principles calculations. *Journal of Materials Chemistry C*, Royal Society of Chemistry, v. 4, n. 16, p. 3592–3598, 2016. DOI: <https://doi.org/10.1039/C6TC00115G>.

30 JIANG, H. et al. Borophene: a promising anode material offering high specific capacity and high rate capability for lithium-ion batteries. *Nano Energy*, Elsevier, v. 23, p. 97–104, 2016. DOI: <https://doi.org/10.1016/j.nanoen.2016.03.013>.

31 ARABHA, S.; AKBARZADEH, A.; RAJABPOUR, A. Engineered porous borophene with tunable anisotropic properties. *Composites Part B: Engineering*, Elsevier, v. 200, p. 108260, 2020. DOI: <https://doi.org/10.1016/j.compositesb.2020.108260>.

32 ZHOU, X. et al. Two-Dimensional Boron-Rich Monolayer B x N as High Capacity for Lithium-Ion Batteries: A First-Principles Study. *ACS Applied Materials & Interfaces*, ACS Publications, v. 13, n. 34, p. 41169–41181, 2021. DOI: <https://doi.org/10.1021/acsami.1c08331>.

33 TANG, H.; ISMAIL-BEIGI, S. Novel precursors for boron nanotubes: the competition of two-center and three-center bonding in boron sheets. *Physical Review Letters*, APS, v. 99, n. 11, p. 115501, 2007. DOI: <https://doi.org/10.1103/PhysRevLett.99.115501>.

34 LIU, Y.; PENEV, E. S.; YAKOBSON, B. I. Probing the Synthesis of Two-Dimensional Boron by First-Principles Computations. *Angewandte Chemie International Edition*, Wiley Online Library, v. 52, n. 11, p. 3156–3159, 2013. DOI: <https://doi.org/10.1002/ange.201207972>.

35 ZHANG, Z. et al. Two-Dimensional Boron Monolayers Mediated by Metal Substrates. *Angewandte Chemie International Edition*, Wiley Online Library, v. 54, n. 44, p. 13022–13026, 2015. DOI: <https://doi.org/10.1002/ange.201505425>.

36 LIU, X. et al. Intermixing and periodic self-assembly of borophene line defects. *Nature Materials*, v. 17, p. 783–8, 2018. DOI: <https://doi.org/10.1038/s41563-018-0134-1>.

37 WU, R. et al. Large-area single-crystal sheets of borophene on Cu (111) surfaces. *Nature Nanotechnology*, Nature Publishing Group, v. 14, n. 1, p. 44–49, 2019. DOI: <https://doi.org/10.1038/s41565-018-0317-6>.

38 KIRALY, B. et al. Borophene synthesis on Au (111). *ACS Nano*, ACS Publications, v. 13, n. 4, p. 3816–3822, 2019. DOI: <https://doi.org/10.1021/acsnano.8b09339>.

39 VINOGRADOV, N. A. et al. Single-phase borophene on Ir (111): formation, structure, and decoupling from the support. *ACS Nano*, ACS Publications, v. 13, n. 12, p. 14511–14518, 2019. DOI: <https://doi.org/10.1021/acsnano.9b08296>.

40 PREOBRAJENSKI, A. B. et al. Honeycomb Boron on Al (111): From the Concept of Borophene to the Two-Dimensional Boride. *ACS Nano*, ACS Publications, v. 15, n. 9, p. 15153–15165, 2021. DOI: <https://doi.org/10.1021/acsnano.1c05603>.

41 CABRAL, T. L. G. et al. C-doping anisotropy effects on borophene electronic transport. *Journal of Physics: Condensed Matter*, IOP Publishing, v. 34, n. 9, p. 095502, 2021. DOI: <https://doi.org/10.1088/1361-648X/ac3d54>.

42 LIU, X. et al. Intermixing and periodic self-assembly of borophene line defects. *Nature Materials*, Nature Publishing Group, v. 17, n. 9, p. 783–788, 2018. DOI: <https://doi.org/10.1038/s41563-018-0134-1>.

43 OGANOV, A. R.; GLASS, C. W. Crystal structure prediction using ab initio evolutionary techniques: Principles and applications. *The Journal of Chemical Physics*, American Institute of Physics, v. 124, n. 24, p. 244704, 2006. DOI: <https://doi.org/10.1063/1.2210932>.

44 SILVESTRE, G. H. Simulação computacional de materiais bidimensionais baseado no elemento boro. Universidade Federal de Uberlândia, 2018. DOI: <http://dx.doi.org/10.14393/ufu.di.2018.1238>.

45 SILVESTRE, G.; SCOPEL, W. L.; MIWA, R. Electronic stripes and transport properties in borophene heterostructures. *Nanoscale*, Royal Society of Chemistry, v. 11, n. 38, p. 17894–17903, 2019. DOI: <https://doi.org/10.1039/c9nr05279h>.

46 NISHIYAMA, Y.; LANGAN, P.; CHANZY, H. Crystal structure and hydrogen-bonding system in cellulose Iβ from synchrotron X-ray and neutron fiber diffraction. *Journal of the American Chemical Society*, ACS Publications, v. 124, n. 31, p. 9074–9082, 2002. DOI: <https://doi.org/10.1021/ja0257319>.

47 CALAHORRA, Y. et al. Nanoscale electromechanical properties of template-assisted hierarchical self-assembled cellulose nanofibers. *Nanoscale*, Royal Society of Chemistry, v. 10, n. 35, p. 16812–16821, 2018. DOI: <https://doi.org/10.1039/C8NR04967J>.

48 DRI, F. L. et al. Anisotropy and temperature dependence of structural, thermodynamic, and elastic properties of crystalline cellulose Iβ: a first-principles investigation. *Modelling and Simulation in Materials Science and Engineering*, IOP Publishing, v. 22, n. 8, p. 085012, 2014. DOI: <https://doi.org/10.1088/0965-0393/22/8/085012>.

49 ZHENG, Q. et al. High-performance flexible piezoelectric nanogenerators consisting of porous cellulose nanofibril (CNF)/poly (dimethylsiloxane)(PDMS) aerogel films. *Nano Energy*, Elsevier, v. 26, p. 504–512, 2016. DOI: <https://doi.org/10.1016/j.nanoen.2016.06.009>.

50 RAJALA, S. et al. Cellulose nanofibril film as a piezoelectric sensor material. *ACS applied materials & interfaces*, v. 8, n. 24, p. 15607–15614, 2016. DOI: <https://doi.org/10.1021/acsami.6b03597>.

51 LI, T. et al. Cellulose ionic conductors with high differential thermal voltage for low-grade heat harvesting. *Nature Materials*, Nature Publishing Group, v. 18, n. 6, p. 608–613, 2019. DOI: <https://doi.org/10.1038/s41563-019-0315-6>.

52 KIM, H.-J. et al. Bacterial nano-cellulose triboelectric nanogenerator. *Nano Energy*, Elsevier, v. 33, p. 130–137, 2017. DOI: <https://doi.org/10.1016/j.nanoen.2017.01.035>.

53 MOLNÁR, G. et al. Cellulose crystals plastify by localized shear. *Proceedings of the National Academy of Sciences*, v. 115, n. 28, p. 7260–7265, 2018. DOI: <https://doi.org/10.1073/pnas.1800098115>.

54 KHALIL, H. A.; BHAT, A.; YUSRA, A. I. Green composites from sustainable cellulose nanofibrils: A review. *Carbohydrate Polymers*, Elsevier, v. 87, n. 2, p. 963–979, 2012. DOI: <https://doi.org/10.1016/j.carbpol.2011.08.078>.

55 ISOGAI, A.; SAITO, T.; FUKUZUMI, H. TEMPO-oxidized cellulose nanofibers. *Nanoscale*, Royal Society of Chemistry, v. 3, n. 1, p. 71–85, 2011. DOI: <https://doi.org/10.1039/C0NR00583E>.

56 TAYLOR, N. G. Cellulose biosynthesis and deposition in higher plants. *New Phytologist*, Wiley Online Library, v. 178, n. 2, p. 239–252, 2008. DOI: <https://doi.org/10.1111/j.1469-8137.2008.02385.x>.

57 MELLEROWICZ, E. J.; GORSHKOVA, T. A. Tensional stress generation in gelatinous fibres: a review and possible mechanism based on cell-wall structure and composition. *Journal of Experimental Botany*, Oxford University Press, v. 63, n. 2, p. 551–565, 2012. DOI: <https://doi.org/10.1093/jxb/err339>.

58 NECHYPORCHUK, O.; BELGACEM, M. N.; BRAS, J. Production of cellulose nanofibrils: A review of recent advances. *Industrial Crops and Products*, Elsevier, v. 93, p. 2–25, 2016. DOI: <https://doi.org/10.1016/j.indcrop.2016.02.016>.

59 PINTO, L. O.; BERNARDES, J. S.; REZENDE, C. A. Low-energy preparation of cellulose nanofibers from sugarcane bagasse by modulating the surface charge density. *Carbohydrate Polymers*, Elsevier, v. 218, p. 145–153, 2019. DOI: <https://doi.org/10.1016/j.carbpol.2019.04.070>.

60 AJALA, E. et al. Sugarcane bagasse: a biomass sufficiently applied for improving global energy, environment and economic sustainability. *Bioresources and Bioprocessing*, SpringerOpen, v. 8, n. 1, p. 1–25, 2021. DOI: <https://doi.org/10.1186/s40643-021-00440-z>.

61 KHOO, R.; CHOW, W.; ISMAIL, H. Sugarcane bagasse fiber and its cellulose nanocrystals for polymer reinforcement and heavy metal adsorbent: a review. *Cellulose*, Springer, v. 25, n. 8, p. 4303–4330, 2018. DOI: <https://doi.org/10.1007/s10570-018-1879-z>.

62 INUI, T. et al. A miniaturized flexible antenna printed on a high dielectric constant nanopaper composite. *Advanced Materials*, Wiley Online Library, v. 27, n. 6, p. 1112–1116, 2015. DOI: <https://doi.org/10.1002/adma.201404555>.

63 YANG, X. et al. Cellulose nanocrystal aerogels as universal 3D lightweight substrates for supercapacitor materials. *Advanced Materials*, Wiley Online Library, v. 27, n. 40, p. 6104–6109, 2015. DOI: <https://doi.org/10.1002/adma.201502284>.

64 FINGOLO, A. C. et al. Enhanced Hydrophobicity in Nanocellulose-Based Materials: Toward Green Wearable Devices. *ACS Applied Bio Materials*, ACS Publications, v. 4, n. 9, p. 6682–6689, 2021. DOI: <https://doi.org/10.1021/acsabm.1c00317>.

65 CAO, S. et al. Solution-processed flexible paper-electrode for lithium-ion batteries based on MoS2 nanosheets exfoliated with cellulose nanofibrils. *Electrochimica Acta*, Elsevier, v. 298, p. 22–30, 2019. DOI: <https://doi.org/10.1016/j.electacta.2018.12.067>.

66 THOMAS, L. H. The calculation of atomic fields. In: CAMBRIDGE UNIVERSITY PRESS. *Mathematical Proceedings of the Cambridge Philosophical Society.* [S.l.], 1927. v. 23, p. 542–548.

67 FERMI, E. A statistical method for determining some properties of the atoms and its application to the theory of the periodic table of elements. *Z. Phys*, v. 48, p. 73–79, 1928.

68 DIRAC, P. A. M. Note on exchange phenomena in the Thomas-Fermi atom. In: *Proc. Cambridge Philos. Soc.* [S.l.: s.n.], 1931. v. 26, p. 376–385.

69 MARTIN, R. M. *Electronic Structure: Basic Theory and Practical Methods.* [S.l.]: Cambridge University Press, 2004. DOI: <https://doi.org/10.1017/CBO9780511805769>.

70 DENTENEER, P. J. H. *The pseudopotential-density-functional method applied to semiconducting crystals.* Tese (Doutorado) — Eindhoven University of Technology, 1987. DOI: <https://doi.org/10.6100/IR263952>.

71 HOHENBERG, P.; KOHN, W. Inhomogeneous electron gas. *Physical review*, APS, v. 136, n. 3B, p. B864, 1964. DOI: <https://doi.org/10.1103/PhysRev.136.B864>.

72 SHOLL, D. S.; STECKEL, J. A. *Density functional theory: a practical introduction.* [S.l.]: John Wiley & Sons, 2011. DOI: <https://doi.org/10.1002/9780470447710>.

73 KOHN, W.; SHAM, L. J. Self-consistent equations including exchange and correlation effects. *Physical review*, APS, v. 140, n. 4A, p. A1133, 1965. DOI: <https://d.orgoi/10.1103/PhysRev.140.A1133>.

74 CAPELLE, K. A bird's-eye view of density-functional theory. *Brazilian Journal of Physics*, SciELO Brasil, v. 36, n. 4A, p. 1318–1343, 2006. DOI: <https://doi.org/10.1590/S0103-97332006000700035>.

75 PARR, R. G.; YANG, W. *Density-Functional Theory of Atoms and Molecules.* [S.l.]: Oxford University Press, 1989. DOI: <https://doi.org/10.1093/oso/9780195092769.001.0001>.

76 PERDEW, J. P.; BURKE, K.; ERNZERHOF, M. Generalized gradient approximation made simple. *Physical review letters*, APS, v. 77, n. 18, p. 3865, 1996. DOI: <https://doi.org/10.1103/PhysRevLett.77.3865>.

77 PERDEW, J. P.; BURKE, K. Comparison shopping for a gradient-corrected density functional. *International journal of quantum chemistry*, v. 57, n. 3, p. 309–319, 1996. DOI: <https://doi.org/10.1002/(SICI)1097-461X(1996)57:3%3C309::AID-QUA4%3E3.0.CO;2-1>.

78 GRIMME, S. Semiempirical GGA-type density functional constructed with a long-range dispersion correction. *Journal of Computational Chemistry*, Wiley Online Library, v. 27, n. 15, p. 1787–1799, 2006. DOI: <https://doi.org/10.1002/jcc.20495>.

79 RYDBERG, H. et al. Van der Waals density functional for layered structures. *Physical Review Letters*, APS, v. 91, n. 12, p. 126402, 2003. DOI: <https://doi.org/10.1103/PhysRevLett.91.126402>.

80 DION, M. et al. Van der Waals density functional for general geometries. *Physical Review Letters*, APS, v. 92, n. 24, p. 246401, 2004. DOI: <https://doi.org/10.1103/PhysRevLett.92.246401>.

81 LEE, K. et al. Higher-accuracy van der Waals density functional. *Physical Review B*, APS, v. 82, n. 8, p. 081101, 2010. DOI: <https://doi.org/10.1103/PhysRevB.82.081101>.

82 KLIMEŠ, J.; BOWLER, D. R.; MICHAELIDES, A. Van der Waals density functionals applied to solids. *Physical Review B*, APS, v. 83, n. 19, p. 195131, 2011. DOI: <https://doi.org/10.1103/PhysRevB.83.195131>.

83 HAMANN, D.; SCHLÜTER, M.; CHIANG, C. Norm-conserving pseudopotentials. *Physical Review Letters*, APS, v. 43, n. 20, p. 1494, 1979. DOI: <https://doi.org/10.1103/PhysRevLett.43.1494>.

84 TROULLIER, N.; MARTINS, J. L. Efficient pseudopotentials for plane-wave calculations. *Physical review B*, APS, v. 43, n. 3, p. 1993, 1991. DOI: <https://doi.org/10.1103/PhysRevB.43.1993>.

85 VANDERBILT, D. Soft self-consistent pseudopotentials in a generalized eigenvalue formalism. *Physical Review B*, APS, v. 41, n. 11, p. 7892, 1990. DOI: <https://doi.org/10.1103/PhysRevB.41.7892>.

86 KRESSE, G.; HAFNER, J. Norm-conserving and ultrasoft pseudopotentials for first-row and transition elements. *Journal of Physics: Condensed Matter*, IOP Publishing, v. 6, n. 40, p. 8245, 1994. DOI: <https://doi.org/10.1088/0953-8984/6/40/015>.

87 KRESSE, G.; JOUBERT, D. From ultrasoft pseudopotentials to the projector augmented-wave method. *Physical Review B*, APS, v. 59, n. 3, p. 1758, 1999. DOI: <https://doi.org/10.1103/PhysRevB.59.1758>.

88 SLATER, J. C. Wave functions in a periodic potential. *Physical Review*, APS, v. 51, n. 10, p. 846, 1937. DOI: <https://doi.org/10.1103/PhysRev.51.846>.

89 OLIVEIRA, I. S.; De Jesus, V. L. *Introdução à física do estado sólido.* [S.l.]: Editora Livraria da Fisica, 2005.

90 KITTEL, C.; MCEUEN, P.; MCEUEN, P. *Introduction to solid state physics*. [S.l.]: Wiley New York, 1996. v. 8.

91 CHADI, D. J.; COHEN, M. L. Special points in the Brillouin zone. *Physical Review B*, APS, v. 8, n. 12, p. 5747, 1973. DOI: <https://doi.org/10.1103/PhysRevB.8.5747>.

92 PAYNE, M. C. et al. Iterative minimization techniques for ab initio total-energy calculations: molecular dynamics and conjugate gradients. *Reviews of modern physics*, APS, v. 64, n. 4, p. 1045, 1992. DOI: <https://doi.org/10.1103/RevModPhys.64.1045>.

93 PADILHA, J. E.; MIWA, R. H.; FAZZIO, A. Directional dependence of the electronic and transport properties of 2D borophene and borophane. *Physical Chemistry Chemical Physics*, Royal Society of Chemistry, v. 18, n. 36, p. 25491–25496, 2016. DOI: <https://doi.org/10.1039/C6CP05092A>.

94 KISTANOV, A. A. et al. Exploring the charge localization and band gap opening of borophene: a first-principles study. *Nanoscale*, Royal Society of Chemistry, v. 10, n. 3, p. 1403–1410, 2018. DOI: <https://doi.org/10.1039/C7NR06537J>.

95 ROOS, M. et al. Intermolecular vs molecule–substrate interactions: A combined STM and theoretical study of supramolecular phases on graphene/Ru (0001). *Beilstein Journal of Nanotechnology*, Beilstein-Institut, v. 2, n. 1, p. 365–373, 2011. DOI: <https://doi.org/10.3762/bjnano.2.42>.

96 WANG, Q. H.; HERSAM, M. C. Room-temperature molecular-resolution characterization of self-assembled organic monolayers on epitaxial graphene. *Nature Chemistry*, Nature Publishing Group, v. 1, n. 3, p. 206, 2009. DOI: <https://doi.org/10.1038/nchem.212>.

97 ALZAHRANI, A. First-principles study on the structural and electronic properties of graphene upon benzene and naphthalene adsorption. *Applied Surface Science*, Elsevier, v. 257, n. 3, p. 807–810, 2010. DOI: <https://doi.org/10.1016/j.apsusc.2010.07.069>.

98 OLIVEIRA, I. de; MIWA, R. Organic molecules deposited on graphene: A computational investigation of self-assembly and electronic structure. *The Journal of chemical physics*, AIP Publishing LLC, v. 142, n. 4, p. 044301, 2015. DOI: <https://doi.org/10.1063/1.4906435>.

99 CHEN, W. et al. Surface transfer p-type doping of epitaxial graphene. *Journal of the American Chemical Society*, ACS Publications, v. 129, n. 34, p. 10418–10422, 2007. DOI: <https://doi.org/10.1021/ja071658g>.

100 THONHAUSER, T. et al. Van der Waals density functional: Self-consistent potential and the nature of the van der Waals bond. *Physical Review B*, APS, v. 76, n. 12, p. 125112, 2007. DOI: <https://doi.org/10.1103/PhysRevB.76.125112>.

101 THONHAUSER, T. et al. Spin signature of nonlocal correlation binding in metal-organic frameworks. *Physical Review Letters*, APS, v. 115, n. 13, p. 136402, 2015. DOI: <https://doi.org/10.1103/PhysRevLett.115.136402>.

102 BERLAND, K. et al. van der Waals forces in density functional theory: a review of the vdW-DF method. *Reports on Progress in Physics*, IOP Publishing, v. 78, n. 6, p. 066501, 2015. DOI: <https://doi.org/10.1088/0034-4885/78/6/066501>.

103 LANGRETH, D. et al. A density functional for sparse matter. *Journal of Physics: Condensed Matter*, IOP Publishing, v. 21, n. 8, p. 084203, 2009. DOI: <https://doi.org/10.1088/0953-8984/21/8/084203>.

104 DING, S.-Y.; HIMMEL, M. E. The maize primary cell wall microfibril: a new model derived from direct visualization. *Journal of Agricultural and food Chemistry*, ACS Publications, v. 54, n. 3, p. 597–606, 2006. DOI: <https://doi.org/10.1021/jf051851z>.

105 SILVESTRE, G. H. et al. Disassembly of TEMPO-Oxidized Cellulose Fibers: Intersheet and Interchain Interactions in the Isolation of Nanofibers and Unitary Chains. *The Journal of Physical Chemistry B*, ACS Publications, v. 125, n. 14, p. 3717–3724, 2021. DOI: <https://doi.org/10.1021/acs.jpcb.1c01928>.

106 QIAN, X. et al. Atomic and electronic structures of molecular crystalline cellulose Iβ: A first-principles investigation. *Macromolecules*, ACS Publications, v. 38, n. 25, p. 10580–10589, 2005. DOI: <https://doi.org/10.1021/ma051683b>.

107 PARTHASARATHI, R. et al. Insights into hydrogen bonding and stacking interactions in cellulose. *The Journal of Physical Chemistry A*, ACS Publications, v. 115, n. 49, p. 14191–14202, 2011. DOI: <https://doi.org/10.1021/jp203620x>.

108 LI, Y.; LIN, M.; DAVENPORT, J. W. Ab initio studies of cellulose I: crystal structure, intermolecular forces, and interactions with water. *The Journal of Physical Chemistry C*, ACS Publications, v. 115, n. 23, p. 11533–11539, 2011. DOI: <https://doi.org/10.1021/jp2006759>.

109 GROSS, A. S.; CHU, J.-W. On the molecular origins of biomass recalcitrance: the interaction network and solvation structures of cellulose microfibrils. *The Journal of Physical Chemistry B*, ACS Publications, v. 114, n. 42, p. 13333–13341, 2010. DOI: <https://doi.org/10.1021/jp106452m>.

110 GROSS, A. S.; BELL, A. T.; CHU, J.-W. Thermodynamics of cellulose solvation in water and the ionic liquid 1-butyl-3-methylimidazolim chloride. *The Journal of Physical Chemistry B*, ACS Publications, v. 115, n. 46, p. 13433–13440, 2011. DOI: <https://doi.org/10.1021/jp202415v>.

111 GURTOVENKO, A. A. et al. Phospholipid–Cellulose Interactions: Insight from Atomistic Computer Simulations for Understanding the Impact of Cellulose-Based Materials on Plasma Membranes. *The Journal of Physical Chemistry B*, ACS Publications, v. 122, n. 43, p. 9973–9981, 2018. DOI: <https://doi.org/10.1021/acs.jpcb.8b07765>.

112 GURTOVENKO, A. A.; KARTTUNEN, M. Controlled On–Off Switching of Tight-Binding Hydrogen Bonds between Model Cell Membranes and Acetylated Cellulose Surfaces. *Langmuir*, ACS Publications, v. 35, n. 42, p. 13753–13760, 2019. DOI: <https://doi.org/10.1021/acs.langmuir.9b02453>.

113 MIYAMOTO, H. et al. Structural reorganization of molecular sheets derived from cellulose II by molecular dynamics simulations. *Carbohydrate Research*, Elsevier, v. 344, n. 9, p. 1085–1094, 2009. DOI: <https://doi.org/10.1016/j.carres.2009.03.014>.

114 MIYAMOTO, H.; YAMANE, C.; UEDA, K. Structural changes in the molecular sheets along (hk0) planes derived from cellulose Iβ by molecular dynamics simulations. *Cellulose*, Springer, v. 20, n. 3, p. 1089–1098, 2013. DOI: <https://doi.org/10.1007/s10570-013-9915-5>.

115 QIAN, G.-X.; MARTIN, R. M.; CHADI, D. First-principles study of the atomic reconstructions and energies of Ga-and As-stabilized GaAs (100) surfaces. *Physical Review B*, APS, v. 38, n. 11, p. 7649, 1988. DOI: <https://doi.org/10.1103/PhysRevB.38.7649>.

116 DESHPANDE, M. et al. Binding strength of sodium ions in cellulose for different water contents. *The Journal of Physical Chemistry B*, ACS Publications, v. 112, n. 30, p. 8985–8989, 2008. DOI: <https://doi.org/10.1021/jp8020547>.

117 TEJADO, A. et al. Energy requirements for the disintegration of cellulose fibers into cellulose nanofibers. *Cellulose*, Springer, v. 19, n. 3, p. 831–842, 2012. DOI: <https://doi.org/10.1007/s10570-012-9694-4>.

118 SAITO, T.; ISOGAI, A. TEMPO-mediated oxidation of native cellulose. The effect of oxidation conditions on chemical and crystal structures of the water-insoluble fractions. *Biomacromolecules*, ACS Publications, v. 5, n. 5, p. 1983–1989, 2004. DOI: <https://doi.org/10.1021/bm0497769>.

119 SAITO, T. et al. Homogeneous suspensions of individualized microfibrils from TEMPO-catalyzed oxidation of native cellulose. *Biomacromolecules*, ACS Publications, v. 7, n. 6, p. 1687–1691, 2006. DOI: <https://doi.org/10.1021/bm060154s>.

120 PAAJANEN, A. et al. Atomistic molecular dynamics simulations on the interaction of TEMPO-oxidized cellulose nanofibrils in water. *Cellulose*, Springer, v. 23, n. 6, p. 3449–3462, 2016. DOI: <https://doi.org/10.1007/s10570-016-1076-x>.

121 LOWDIN, P.-O. Quantum theory of many-particle systems. II. Study of the ordinary Hartree-Fock approximation. *Physical Review*, APS, v. 97, n. 6, p. 1490, 1955. DOI: <https://doi.org/10.1103/PhysRev.97.1490>.

122 FAN, Y. et al. Tunable electronic structures of graphene/boron nitride heterobilayers. *Applied Physics Letters*, American Institute of Physics, v. 98, n. 8, p. 083103, 2011. DOI: <https://doi.org/10.1063/1.3556640>.

123 PETRY, R. et al. Machine learning of microscopic ingredients for graphene oxide/cellulose interaction. *Langmuir*, ACS Publications, v. 38, n. 3, p. 1124–1130, 2022. DOI: <https://doi.org/10.1021/acs.langmuir.1c02780>.

124 ALQUS, R.; EICHHORN, S. J.; BRYCE, R. A. Molecular dynamics of cellulose amphiphilicity at the graphene–water interface. *Biomacromolecules*, ACS Publications, v. 16, n. 6, p. 1771–1783, 2015. DOI: <https://doi.org/10.1021/acs.biomac.5b00307>.

125 MIANEHROW, H.; BERGLUND, L. A.; WOHLERT, J. Interface effects from moisture in nanocomposites of 2D graphene oxide in cellulose nanofiber (CNF) matrix–A molecular dynamics study. *Journal of Materials Chemistry A*, Royal Society of Chemistry, v. 10, n. 4, p. 2122–2132, 2022. DOI: <https://doi.org/10.1039/D1TA09286C>.

126 MATHEW, K. et al. Implicit solvation model for density-functional study of nanocrystal surfaces and reaction pathways. *The Journal of Chemical Physics*, American Institute of Physics, v. 140, n. 8, p. 084106, 2014. DOI: <https://doi.org/10.1063/1.4865107>.

127 MATHEW, K. et al. Implicit self-consistent electrolyte model in plane-wave density-functional theory. *The Journal of Chemical Physics*, AIP Publishing LLC, v. 151, n. 23, p. 234101, 2019. DOI: <https://doi.org/10.1063/1.5132354>.

128 PRENDERGAST, D.; GALLI, G. X-ray absorption spectra of water from first principles calculations. *Physical Review Letters*, APS, v. 96, n. 21, p. 215502, 2006. DOI: <https://doi.org/10.1103/PhysRevLett.96.215502>.

129 GOUGOUSSIS, C. et al. First-principles calculations of x-ray absorption in a scheme based on ultrasoft pseudopotentials: From α-quartz to high-T_c compounds. *Phys. Rev. B*, v. 80, p. 075102, 2009. DOI: <https://doi.org/10.1103/PhysRevB.80.075102>.

130 LIMA, F. C. de et al. Simulations of X-ray absorption spectroscopy and energetic conformation of N-heterocyclic carbenes on Au (111). *Physical Chemistry Chemical Physics*, Royal Society of Chemistry, v. 22, n. 37, p. 21504–21511, 2020. DOI: <https://doi.org/10.1039/D0CP04240D>.

131 INAYEH, A. et al. Self-assembly of N-heterocyclic carbenes on Au (111). *Nature Communications*, Nature Publishing Group, v. 12, n. 1, p. 1–9, 2021. DOI: <https://doi.org/10.1038/s41467-021-23940-0>.

132 SCHIROS, T. et al. Connecting dopant bond type with electronic structure in N-doped graphene. *Nano Letters*, ACS Publications, v. 12, n. 8, p. 4025–4031, 2012. DOI: <https://doi.org/10.1021/nl301409h>.

133 LIPPITZ, A.; FRIEDRICH, J. F.; UNGER, W. E. Plasma bromination of HOPG surfaces: A NEXAFS and synchrotron XPS study. *Surface Science*, Elsevier, v. 611, p. L1–L7, 2013. DOI: <https://doi.org/10.1016/j.susc.2013.01.020>.

134 XU, J. et al. X-ray absorption spectra of graphene and graphene oxide by full-potential multiple scattering calculations with self-consistent charge density. *Physical Review B*, APS, v. 92, n. 12, p. 125408, 2015. DOI: <https://doi.org/10.1103/PhysRevB.92.125408>.

135 CODY, G. D. Probing chemistry within the membrane structure of wood with soft X-ray spectral microscopy. In: AMERICAN INSTITUTE OF PHYSICS. *AIP Conference Proceedings*. [S.l.], 2000. v. 507, n. 1, p. 307–312. DOI: <https://doi.org/10.1063/1.1291162>.

136 KARUNAKARAN, C. et al. Introduction of soft X-ray spectromicroscopy as an advanced technique for plant biopolymers research. *PloS One*, Public Library of Science San Francisco, CA USA, v. 10, n. 3, p. e0122959, 2015. DOI: <https://doi.org/10.1371/journal.pone.0122959>.

137 BADER, R. *Atoms in Molecules: A Quantum Theory*. New York: Oxford University Press, 1990.

138 SI, C.; SUN, Z.; LIU, F. Strain engineering of graphene: a review. *Nanoscale*, Royal Society of Chemistry, v. 8, n. 6, p. 3207–3217, 2016. DOI: <DOIhttps://doi.org/10.1039/C5NR07755A>.

139 MIAO, F.; LIANG, S.-J.; CHENG, B. Straintronics with van der Waals materials. *NPJ Quantum Materials*, Nature Publishing Group, v. 6, n. 1, p. 1–4, 2021. DOI: <https://doi.org/10.1038/s41535-021-00360-3>.

140 VINCENT, T. et al. Probing the nanoscale origin of strain and doping in graphene-hBN heterostructures. *2D Materials*, IOP Publishing, v. 6, n. 1, p. 015022, 2018. DOI: <https://doi.org/10.1088/2053-1583/aaf1dc>.

141 FORESTIER, A. et al. Strain and piezo-doping mismatch between graphene layers. *The Journal of Physical Chemistry C*, ACS Publications, v. 124, n. 20, p. 11193–11199, 2020. DOI: <https://doi.org/10.1021/acs.jpcc.0c01898>.

142 BORN, M.; OPPENHEIMER, R. Zur quantentheorie der molekeln. *Annalen der Physik*, Wiley Online Library, v. 389, n. 20, p. 457–484, 1924. DOI: <https://doi.org/10.1007/978-3-642-61659-4_16>.

143 HERZBERG, G. Molecular spectra and molecular structure. Vol. 3: Electronic spectra and electronic structure of polyatomic molecules. *New York: Van Nostrand, Reinhold, 1966*, 1966.

144 BALLHAUSEN, C.; HANSEN, A. E. Electronic spectra. *Annual Review of Physical Chemistry*, Annual Reviews 4139 El Camino Way, PO Box 10139, Palo Alto, CA 94303-0139, USA, v. 23, n. 1, p. 15–38, 1972.

145 VIANNA, J. D. M.; FAZZIO, A.; CANUTO, S. *Teoria Quântica de Moléculas e Sólidos*. [S.l.]: Editora Livraria da Física, 2004.

146 SAKURAI, J. J.; NAPOLITANO, J. *Modern quantum mechanics*. [S.l.]: Cambridge University Press, 2017.

147 BUNKER, G. *Introduction to XAFS: a practical guide to X-ray absorption fine structure spectroscopy*. [S.l.]: Cambridge University Press, 2010.

148 PARRATT, L. Electronic band structure of solids by x-ray spectroscopy. *Reviews of Modern Physics*, APS, v. 31, n. 3, p. 616, 1959. DOI: <https://doi.org/10.1103/RevModPhys.31.616>.

149 GROOT, F. D. X-ray absorption and dichroism of transition metals and their compounds. *Journal of Electron Spectroscopy and Related Phenomena*, Elsevier, v. 67, n. 4, p. 529–622, 1994. DOI: <https://doi.org/10.1016/0368-2048(93)02041-J>.

150 BLÖCHL, P. E. Projector augmented-wave method. *Physical Review B*, APS, v. 50, n. 24, p. 17953, 1994. DOI: <https://doi.org/10.1103/PhysRevB.50.17953>.

151 MONKHORST, H. J.; PACK, J. D. Special points for Brillouin-zone integrations. *Physical Review B*, APS, v. 13, n. 12, p. 5188, 1976. DOI: <https://doi.org/10.1103/PhysRevB.13.5188>.

152 KRESSE, G.; FURTHMULLER, J. Efficient iterative schemes for ab initio total-energy calculations using a plane-wave basis set. *Physical Review B*, APS, v. 54, n. 16, p. 11169, 1996. DOI: <https://doi.org/10.1103/PhysRevB.54.11169>.

153 BUNĂU, O.; CALANDRA, M. Projector augmented wave calculation of x-ray absorption spectra at the $L_{2,3}$ edges. *Physical Review B*, APS, v. 87, n. 20, p. 205105, 2013. DOI: <https://doi.org/10.1103/PhysRevB.87.205105>.

154 TAILLEFUMIER, M. et al. X-ray absorption near-edge structure calculations with the pseudopotentials: Application to the K edge in diamond and α-quartz. *Phys. Rev. B*, v. 66, p. 195107, 2002. DOI: <https://doi.org/10.1103/PhysRevB.66.195107>.

155 GIANNOZZI, P. et al. QUANTUM ESPRESSO: a modular and open-source software project for quantum simulations of materials. *Journal of Physics: Condensed Matter*, IOP Publishing, v. 21, n. 39, p. 395502, 2009. DOI: <https://doi.org/10.1088/0953-8984/21/39/395502>.

156 PICKARD, C. J.; MAURI, F. All-electron magnetic response with pseudopotentials: NMR chemical shifts. *Physical Review B*, APS, v. 63, n. 24, p. 245101, 2001. DOI: <https://doi.org/10.1103/PhysRevB.63.245101>.

157 HAMADA, I. van der Waals density functional made accurate. *Physical Review B*, APS, v. 89, n. 12, p. 121103, 2014. DOI: <https://doi.org/10.1103/PhysRevB.89.121103>.

158 KLIMEŠ, J.; BOWLER, D. R.; MICHAELIDES, A. Chemical accuracy for the van der Waals density functional. *Journal of Physics: Condensed Matter*, IOP Publishing, v. 22, n. 2, p. 022201, 2009. DOI: <https://doi.org/10.1103/10.1088/0953-8984/22/2/022201>.

159 SILVESTRE, G. H. et al. Nanoscale structural and electronic properties of cellulose/graphene interfaces. *Physical Chemistry Chemical Physics*, Royal Society of Chemistry, v. 25, n. 2, p. 1161–1168, 2023. DOI: <https://doi.org/10.1039/D2CP04146D>.